VISCOELASTIC PROPERTIES OF HYDROGEL-BASED MATERIALS FOR TISSUE ENGINEERING SCAFFOLDS

Rok Kocen

Doctoral Dissertation
Jožef Stefan International Postgraduate School
Ljubljana, Slovenia

Supervisor: Prof. Dr. Saša Novak Krmpotič, Jožef Stefan Institute, Ljubljana, Slovenia

Evaluation Board:
Asst. Prof. Dr. Andraž Kocjan, Chair, Jožef Stefan Institute, Ljubljana, Slovenia
Prof. Dr. Michael Gasik, Member, Aalto University, Helsinki, Finland
Prof. Dr. Karin Stana Kleinschek, Member, Faculty of Mechanical Engineering,
University of Maribor, Maribor, Slovenia

MEDNARODNA PODIPLOMSKA ŠOLA JOŽEFA STEFANA
JOŽEF STEFAN INTERNATIONAL POSTGRADUATE SCHOOL



Rok Kocen

VISCOELASTIC PROPERTIES OF HYDROGEL-BASED MATERIALS FOR TISSUE ENGINEERING SCAFFOLDS

Doctoral Dissertation

VISKOELASTIČNE LASTNOSTI KOMPOZITOV NA OSNOVI HIDROGELOV ZA NOSILCE V TKIVNEM INŽENIRSTVU

Doktorska disertacija

Supervisor: Prof. Dr. Saša Novak Krmpotič

Ljubljana, Slovenia, November 2017

To my cousin Gašper. You will always be in our hearts.

Acknowledgments

First, I would like to thank my supervisor, Prof. Dr. Saša Novak Krmpotič, for giving me the opportunity to work on this topic in the first place, all the support and guidance. I am also thankful for all the discussions we had and when the topic went away from her expertise, her willingness to connect with people who could provide me with the information and the help I needed.

I would like to thank the Slovenian Research Agency for funding my Doctoral studies. I would also like to thank COST Action MP1005 'From nano to macro biomaterials (design, processing, characterisation, modelling) and applications to stem cell regenerative orthopaedic and dental medicine-NAMABIO', for funding two of my Short-Term Scientific Missions to Finland and Austria.

I would like to thank Prof. Dr. Michael Gasik for hosting me at the Aalto University Foundation. I am thankful for all the discussions we had during and after my visit, giving me the opportunity to work in his laboratory and for further collaboration.

I would like to thank Prof. Dr. Christian Hellmich for a kind welcome and all the fruitful discussions we had during my visit to the Vienna University of Technology, Austria. And I would especially like to thank Dr. Maria-Ioana Pastrama and Dr. Romane Blanchard for all the help in the laboratories and the great time we had in Vienna.

I would like to thank Prof. Bojana Obradović for hosting me at Faculty of Technology and Metallurgy, University of Belgrade, Serbia. Special thanks goes also to Jovana Zvicer and Danijela Kostić for all the help in the lab and great time in Belgrade.

I would like to thank Darko Eterovič for keeping up with me, during all the compression tests I performed on the machine in his office.

I would like to thank Prof. Dr. Maja Remškar for letting me use the DMA device for the measurements of my samples and Maja Koblar for showing me how to work with the machine.

I am most grateful to my colleagues in the office: Ana Gantar, Nataša Drnovšek and Martina Lorenzetti. For all that you have taught me, for your help and for all the everyday chitchats. I also have to thank Kaja Križman for all the help in the laboratory. Could not have asked for a better bio-group!

I would also like to thank the whole K7 department, for the great working environment and giving me the opportunity to grow not only in my field, but broaden my knowledge in other areas of material science. Most importantly, I am grateful for all the great times with all the colleagues, whether it was during sport activities, new year's bowling or at the 12 o'clock coffee time.

Last but not least, I would like to thank my family: my parents for all the support, my grandma for all the encouragement and nice words, my brother for the work and non-work related chatting and Polona for being by my side and providing me with unfailing support. This accomplishment would not have been possible without them. Thank you!

Abstract

Tissue engineering is an interdisciplinary field that combines medicine, biology, material science, engineering and others. The goal is to help a patient that suffered from loss or damaged tissue, by providing treatments that help and/or improve regeneration of tissue. Such treatments include stem cells, cell scaffolds and/or growth factors.

Scaffolds provide a suitable environment for the stem cells to grow in as well as for the newly grown tissue, they also provide stimuli for the growth of new tissue and degrade. More specifically, the scaffold needs to be porous to provide space for stem cells to grow in as well as for the bodily fluids to flow inside of the scaffold and provide nutrition for the cells to live, differentiate and proliferate. As the cells multiply and the new tissue grows, the scaffolds needs to provide more space, thus it should degrade. On top of all this, scaffolds need to have certain mechanical properties to sustain mechanical loads.

Mechanical properties of the prepared scaffolds and during their use need to provide support to stem cells. Most tissues and organs have complex viscoelastic properties due to a high amount of water and protein matrix, therefore it makes sense that the scaffolds should have a similar mechanical response. Most common materials for scaffolds currently are hydrogels that appear similar to most tissues, since they contain more than 90 % of water held in a polymer network.

In this work, we performed a study of viscoelastic properties of potential scaffold materials. The material we used is gellan gum (GG) in a combination with bioactive glass (BAG) particles that promote bioactivity. Five techniques were tested with composite samples of GG and BAG. We have determined that dynamical mechanical analysis (DMA) and rheometry are the most suitable techniques that can fully characterize such viscoelastic hydrogel composites, at frequencies that are physiologically relevant. Uniaxial compression also gave comparable results, but with less information in terms of frequency dependence and damping properties. Indentation and ultrasonic wave propagation technique were not suitable for hydrogel composites.

Samples' mechanical properties were measured during submersion in simulated bodily fluid (SBF). We expected degradation of the samples after a month of submersion, however the samples were too stable and did not degrade. However, there was noticeable formation of hydroxyapatite, which is the main mineral phase found in bones. The samples' viscoelastic properties increased during the submersion in SBF after a month.

Gellan gum was also used for 3D printing, which is prerequisite for practical application in the direction of personalized scaffolds. After studying rheological properties of GG, we realized that there is a potential of this hydrogel to be 3D printed. We have modified a commercial 3D printer to be able to use it with thermoactive hydrogels. We were able to print simple geometries with the GG hydrogel.

Povzetek

Tkivni inženiring je interdisciplinarna veda, ki združuje medicino, biologijo, uporabo različnih materialov, inženiring in druga področja. Cilj je spodbuditi regeneracijo tkiv pacientom, ki jim manjka ali pa imajo poškodovano tkivo. Tkivni iženiring vključuje zdravljenje s pomočjo matičnih celic, celičnih ogrodij in rastnih faktorjev.

Celična ogrodja morajo zagotavljati ustrezno okolje za rast matičnih celic in novega tkiva, stimulirati njegovo rast ter se čez določeno obdobje razgraditi. Celično ogrodje mora imeti porozno strukturo, v kateri lahko matične celice rastejo in kjer se lahko pretaka telesna tekočina, ki je potrebna, da se matične celice množijo in diferencirajo. S časom, ko novo tkivo preraste celično ogrodje, se mora le-to razgraditi, da omogoči popolno regeneracijo tkiva. Poleg naštetih, mora celično ogrodje imeti tudi ustrezne mehanske lastnosti.

Po pripravi in med regeneracijo tkiva morajo biti mehanske lastnosti celičnih ogrodij podobne tkivu, ki ga nadomeščajo. Človeška tkiva in organi imajo kompleksne viskoelastične lastnosti zaradi visoke vsebnosti vode in beljakovin, zato so hidrogeli najbolj obetavna skupina materialov, saj vsebujejo več kot 90 % vode in polimerno mrežo.

V tem doktorskem delu smo preučili viskoelastične lastnosti izbranih potencialnih materialov za celična ogrodja. Uporabili smo kompozitne vzorce gelanskega gumija (GG) z delci bioaktivnega stekla (BAG), ki stimulirajo bioaktivnost. Viskoelastične lastnosti vzorcev smo izmerili s petimi različnimi tehnikami. Reometrija in dinamična mehanska analiza (DMA) sta se izkazali za najbolj ustrezni metodi, saj izmerita viskoelastični odziv vzorcev pri različnih frekvencah, ki so fiziološko relevantne. Enoosni tlačni preizkus se je izkazal za ustrezno metodo določevanja elastičnega modula, vendar ne določi frekvenčnega odziva in disipativnih lastnosti. Indentacija in akustična metoda sta se izkazali kot neprimerni za meritve hidrogelnih kompozitov.

Mehanske lastnosti vzorcev smo merili tudi med inkubacijo v simulirani telesni tekočini (SBF). Pričakovali smo, da se bodo vzorci razgradili v enem mesecu, vendar so se v testnem okolju izkazali za prestabilne in se niso razgradili. Opazili pa smo tvorbo hidroksiapatita, ki predstavlja glavni del mineralne faze v kostnem tkivu. Viskoelastične lastnosti vzorcev so se zvišale v času inkubacije v SBF.

Preverili smo, ali je mogoče porozne celične nosilce iz GG oblikovati s 3D tiskanjem. To bi omogočilo hitro personalizacijo celičnih nosilcev oz. implantantov, k čemur stremi tkivni inženiring. Potencial gelanskega gumija za 3D tisk smo opazili pri meritvah z reometrom, kjer smo lahko določili območje geliranja pri ohlajevanju materiala. Konvencionalni 3D tiskalnik smo prilagodili printanju temperaturno aktivnih hidrogelov in natisnili nekaj enostavnejših modelov.

Contents

List of Figures xv

List of Tables xix

Abbreviations xxi

Symbols xxiii

1 Introduction 1
- 1.1 Tissue Engineering . . . 1
- 1.2 Materials for Tissue Engineering Scaffolds . . . 2
  - 1.2.1 Gellan gum . . . 3
  - 1.2.2 Bioactive glass (BAG) . . . 4
  - 1.2.3 Mechanical properties of materials . . . 5
  - 1.2.4 Characterization of mechanical properties . . . 8
- 1.3 Shaping Techniques for Producing Porous 3D Scaffolds . . . 13
  - 1.3.1 Freeze-drying . . . 14
  - 1.3.2 Additive manufacturing . . . 14

2 Aim and Hypothesis 17

3 Materials and Methods 19
- 3.1 Materials . . . 19
  - 3.1.1 Gellan gum and BAG composites . . . 19
  - 3.1.2 Gellan gum with $CaCl_2$ . . . 20
  - 3.1.3 Simulated bodily fluid . . . 21
- 3.2 Characterization of Viscoelastic Properties of Hydrogel Composites . . . 21
  - 3.2.1 Uniaxial compression . . . 21
  - 3.2.2 Rheometry . . . 21
  - 3.2.3 Dynamical mechanical analysis . . . 22
  - 3.2.4 Indentation . . . 23
  - 3.2.5 Ultrasonic wave propagation . . . 24
  - 3.2.6 Density . . . 24
- 3.3 Degradation . . . 25
  - 3.3.1 FT-IR . . . 25
  - 3.3.2 SEM . . . 25
- 3.4 Additive Manufacturing . . . 25
  - 3.4.1 Hardware modification . . . 26

4 Results 29
- 4.1 Characterization of Viscoelastic Properties of Gellan Gum BAG Composite 29
  - 4.1.1 Uniaxial compression . . . 30

4.1.2 Shear rheology . . . 31
4.1.3 Dynamic Mechanical Analysis . . . 34
4.1.4 Indentation . . . 37
4.1.5 Ultrasonic wave propagation . . . 39
4.2 Viscoelastic Properties During Degradation . . . 40
4.2.1 Fourier Transform Infrared Spectroscopy (FT-IR) . . . 41
4.2.2 SEM . . . 41
4.3 Additive Manufacturing . . . 43
4.3.1 Design of a syringe extruder . . . 43
4.3.2 Software for controlling the 3D printer . . . 45
4.3.3 Printing hydrogels . . . 47

5 Discussion **51**
5.1 Choosing the Technique for Characterization of VE Properties of Hydrogel Composites . . . 51
5.1.1 Uniaxial compression . . . 51
5.1.2 Rheometry . . . 52
5.1.3 Dynamic mechanical analysis . . . 54
5.1.4 Indentation . . . 56
5.1.5 Ultrasonic Wave Propagation . . . 57
5.1.6 Comparison of all techniques . . . 62
5.2 Viscoelastic Properties During Degradation . . . 64
5.3 Additive Manufacturing . . . 65
5.3.1 Printing hydrogels . . . 69

6 Conclusions **73**

References **75**

Bibliography **81**

Biography **85**

List of Figures

Figure 1.1: The loading-frequency content (timescale) within knee tissues resulting from common physical activities . . . 2
Figure 1.2: Chemical structure of gellan gum . . . 3
Figure 1.3: Schematic representation of GG structure during cooling and formation of double helices . . . 4
Figure 1.4: Crosslinking of GG double helices with additional Ca^{2+} . . . 4
Figure 1.5: Small volume element . . . 5
Figure 1.6: Sinusoidal wave forms of excitation and response during rheological measurement . . . 6
Figure 1.7: Master curve of highly and lightly crosslinked polymer . . . 7
Figure 1.8: Typical behavior of the dynamic moduli for rubber, concentrated polymeric liquids and dilute solution of random coils and rod-like particles . 8
Figure 1.9: Sketch of a deformed sample's surface during and after indentation and the load-displacement curve of the experiment . . . 10
Figure 1.10: Example of longitudinal and transversal wave propagation . . . 11
Figure 1.11: Phase diagram of water . . . 13
Figure 1.12: SEM picture of a porous sample of GG hydrogel after freeze-drying . . 14
Figure 1.13: Patented design idea of a 3D printed from Prof. Grabec . . . 15
Figure 1.14: 3D bioprinter EnvisionTEC . . . 16

Figure 3.1: SEM micrograph of BAG particles and agglomerates of BAG on hydrogel scaffold . . . 19
Figure 3.2: Benchtop testing machine Galdabini Quasar 50 . . . 22
Figure 3.3: Rheometer Anton Paar MCR 301 . . . 22
Figure 3.4: DMA machine Netzsch Gerätebau DMA242C and a sample in the fixture 23
Figure 3.5: Indentor CSM Nano Hardness Tester® (Switzerland) . . . 23
Figure 3.6: Setup for ultrasonic wave propagation measurements . . . 24
Figure 3.7: Default 3D printer MakerBot Replicator 2X . . . 26
Figure 3.8: Default extruder head for printing thermoplastic polymers on a black plastic x-carriage . . . 27
Figure 3.9: 20 ml glass syringe and costume foil heater . . . 27

Figure 4.1: Prepared samples H0 and H2 . . . 29
Figure 4.2: Stress-strain diagram of GG (H0) and GG-BAG composite (H1) . . . 30
Figure 4.3: Stress-strain diagram at small deformations and elastic moduli of the pure GG and composite samples . . . 30
Figure 4.4: Viscoelastic moduli and temperature of gelation of solid i.e. gelled hydrogel samples with different amounts of BAG . . . 31
Figure 4.5: Viscoelastic moduli and temperature of gelation of solid i.e. gelled hydrogel samples with different amounts of $CaCl_2$ . . . 32

Figure 4.6: Viscoelastic measurements of hydrogels with a varying amount of BAG during the temperature sweep . . . 32
Figure 4.7: Frequency sweeps of GG samples (rheometry) with different amounts of BAG . . . 33
Figure 4.8: Shear moduli (G′ and G″) of GG samples (rheometry) with different amounts of BAG at 1 Hz . . . 34
Figure 4.9: Strain sweep of GG samples (rheometry) with different amounts of BAG 34
Figure 4.10: Strain sweep measurements of GG and BAG composite samples in DMA at 1 Hz . . . 35
Figure 4.11: Frequency sweeps of hydrogels (DMA) with a varying amount of BAG and moduli (E' and E'') at $1Hz$ . . . 35
Figure 4.12: Creep experiments at different creeping forces of the H2 sample . . . 36
Figure 4.13: Force at the sample during creep measurement for H2 samples . . . 37
Figure 4.14: Creep experiments of GG and BAG composite samples at 0.2 and 0.4 N creep force . . . 38
Figure 4.15: Load controlled indentation of sintered BAG sample with respect to time and load-displacement diagram of the same indentation . . . 38
Figure 4.16: Indentation measurements plotted in the order they were measured . . 39
Figure 4.17: Density measurements of hydrogel samples with different amounts of BAG . . . 39
Figure 4.18: Speed of longitudinal and transversal ultrasonic waves in hydrogels and corresponding elements of the stiffness matrix . . . 40
Figure 4.19: Viscoelastic moduli of hydrogel samples during the degradation experiment . . . 40
Figure 4.20: FTIR spectrum of hydrogel samples for degradation before the experiment and after 28 days of incubation . . . 41
Figure 4.21: Porosity of H0Ca1 and H1 samples after freeze-drying . . . 42
Figure 4.22: Figures at the top show micrographs of the samples at day 0 (submerged in SBF for 3 hours) and the bottom figures show micrographs of the samples after 28 days in SBF . . . 42
Figure 4.23: Figures at the top show micrographs of the samples at day 0 (submerged in SBF for 3 hours) and the bottom figures show micrographs of the samples after 28 days in SBF . . . 43
Figure 4.24: Schematic design of the new modified extruder head and the temperature of the material during extrusion . . . 44
Figure 4.25: Drawing of the new extruder head with a syringe without the nozzle in side view, cross-section and isometric view . . . 44
Figure 4.26: 3D rendering of the modified extruder head . . . 45
Figure 4.27: New extruder on the original x-carriage of the 3D printer . . . 46
Figure 4.28: Example of a post-processed CT scan file in Meshmixer of a vertebra and a model of a stepper motor holder of the new extruder in SolidWorks 46
Figure 4.29: Example of a cross-section of a model of a vertebra in Simplify3D with supports and the same model sliced, with different parts in different colors (shells in light and dark blue, infill in orange, supports in grey, raft in purple, etc.) . . . 47
Figure 4.30: Square-shaped wall printed with H0Ca1 hydrogel solution with the side edge of 10 mm . . . 48
Figure 4.31: Zig-zag pattern printed with H0Ca1 hydrogel solution . . . 48
Figure 4.32: Cylindrically shaped wall printed with H0Ca1 hydrogel solution with a diameter of 10 mm. . . . 49

Figure 5.1: Models for predicting mechanical properties of composites with unidirectional fibres (Voigt and Reuss) and spherical particles (Mori-Tanaka) depending on the amount of reinforcing phase 53
Figure 5.2: Storage modulus and temperature of gelation of composite samples of GG and BAG, and GG with added $CaCl_2$ 54
Figure 5.3: Frequency sweep of H0 sample from rheometry and DMA vertically shifted to match the storage moduli 55
Figure 5.4: Creep experiments of H2 sample at 0.4 N and 1.2 N, with fitted Maxwell and Burger's model 55
Figure 5.5: Flowability of H2 samples ($1/\eta_2$) 56
Figure 5.6: Indentation measurements fitted to PDF 57
Figure 5.7: Results of indentation measurements and probability of measured elastic modulus at $\sigma = 2.0\ GPa$ 58
Figure 5.8: Indentation in bulk or porous material 58
Figure 5.9: Comparison of elastic modulus measured with mechanical test and predicted with acoustic measurements for different materials 59
Figure 5.10: Rheometry and ultrasonic wave propagation measurements linked using generalized Maxwell model 60
Figure 5.11: Schematic of Generalized Maxwell model 61
Figure 5.12: Correlation of results of mechanical and acoustic tests on agarose hydrogels with a concentration ranging from 1 to 10 % 62
Figure 5.13: Correlation of shear modulus from DMA measurements and longitudinal moduli from ultrasonic wave propagation 62
Figure 5.14: Coorelation of DMA and ultrasonic wave propagation measurements of epoxy 63
Figure 5.15: A well prepared and partially gelled GG solution with added $CaCl_2$ . . 66
Figure 5.16: Syringe with a properly prepared hydrogel solution and with unwanted air bubble 67
Figure 5.17: Temperature sweep of GG hydrogels with different amounts of BAG measured on a rheometer 67
Figure 5.18: Sketch of hydrogel solution cooling down upon exiting the nozzle . . . 68

List of Tables

Table 1.1: Additive manufacturing techniques [43]. 15

Table 3.1: Composite samples of GG hydrogel and BAG particles. 20
Table 3.2: Samples of GG hydrogel and $CaCl_2$. 20
Table 3.3: Nominal ion concentrations (mM) blood plasma, Original SBF, HBSS and modified HBSS 21

Table 4.1: List of samples measured in creep where some failed and some withstood the creep forces 36

Table 5.1: Constants of Generalized Maxwell model (Figure 5.11) that were used in Figure 5.10. 61

Abbreviations

GG ... Gellan gum
BAG ... Bioactive glass
PDF ... Probability density function
SBF ... Simulated bodily fluid
SAOS ... Small amplitude oscillatory shear
DMA ... Dynamic mechanical analysis
VE ... Viscoelastic
ABS ... Acrylonitrile butadiene styrene
FFF ... Fused filament fabrication
FDM ... Fused deposition modelling

Symbols

G^*	...	Shear complex modulus
G'	...	Shear storage or elastic modulus
G''	...	Shear loss or dissipative modulus
E	...	Uniaxial compression modulus
E^*	...	Uniaxial complex modulus
E'	...	Uniaxial storage or elastic modulus
E''	...	Uniaxial loss or dissipative modulus
δ	...	Damping factor ($\tan(\delta) = G''/G''$)
ω	...	Angular frequency $[rad/s]$
σ	...	Stress
ϵ	...	Strain
S	...	Entropy
E_r	...	Reduced elastic modulus
C_{ijkl}	...	Stiffness tensor
ρ	...	Density
λ	...	Retardation time in creep test ($\lambda = \eta/G$)

Chapter 1

Introduction

1.1 Tissue Engineering

Every day thousands of surgical procedures are performed to replace or repair tissue that has been damaged through disease or trauma. When tissue is damaged beyond repair or when some tissue is missing, surgeons can insert an artificial permanent implant, transplant tissue from one place to another on the patient itself (an autograft) or transplant tissue from another person to the patient (a transplant or allograft). Although these techniques are lifesaving, there are still downsides. The most prominent ones are damage done to the area where the tissue was taken, cost, infections and also rejections in the case of allografts. In order to get around these problems, regenerative medicine aims to help the body to regenerate itself. Regenerative medicine is a broad field that includes tissue engineering, but also covers a research field on self-healing.

Basic idea of tissue engineering is to combine scaffolds, cells and biologically active molecules to regenerate damaged or missing tissue. The field is highly interdisciplinary. It spans from field of medicine, biochemistry, materials science to chemical and mechanical engineering. This approach highly relies on the use of a scaffold that initially provides the support and space for cells and later, after playing its role, it degrades without harmful remains.

Scaffolds have many properties which prominently affect regeneration of the tissue. The ideal scaffold should have the following properties:

- acts as a three-dimensional porous template (support for the cells to adhere, differentiate and proliferate)
- creates stable interface with host tissue and not form scar tissue
- degrades with non-toxic side products
- has similar mechanical properties than the tissue replaced
- is able to withstand the necessary stresses through its lifetime.

Scaffolds for regeneration of cartilage and other connective tissue experience loading forces across a wide spectrum of frequencies i.e. timescales [1]. Slow activities like walking induce loading frequencies below 10 Hz, whereas faster activities like running and jumping can span from 10 to 100 Hz and even more (Figure 1.1).

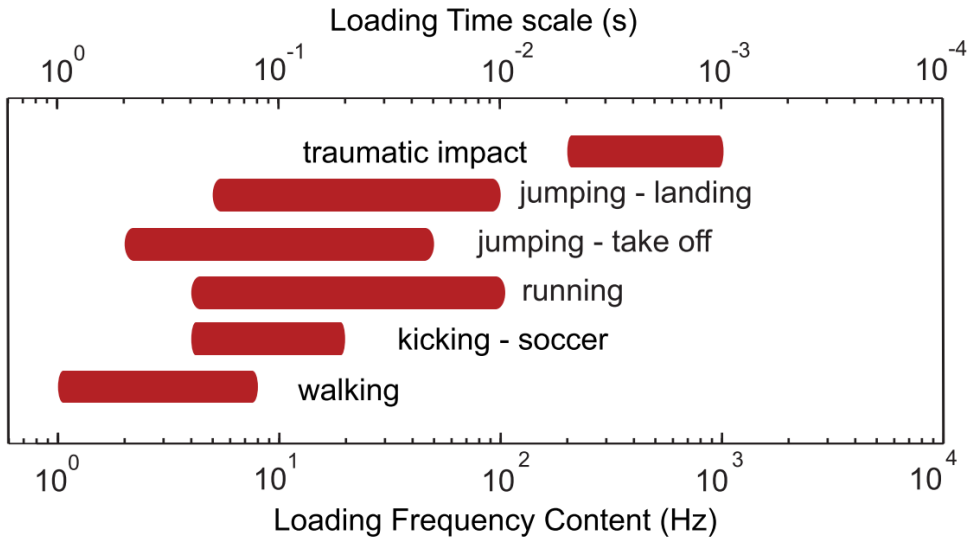


Figure 1.1: The loading-frequency content (timescale) within knee tissues resulting from common physical activities [1].

1.2 Materials for Tissue Engineering Scaffolds

Material used for the scaffold must have specific characteristics. The most important ones are biodegradability, high porosity, specific architecture and high structural strength. All these properties are also connected and need to be balanced. For example, the highest stiffness of a scaffold would be achieved by having a non-porous part. On the other hand, there should be sufficient porosity to provide flow of fluids and space for cells making the scaffold less stiff [2]. Another highly desired property is bioactivity, which increases osteoinductive properties. This can be achieved with the addition of growth stimulating proteins, peptides, growth factors or bioactive glasses. Therefore a balance of all these characteristics needs to be found.

Biodegradable scaffold materials are mainly divided into the following groups: inorganic materials (metals, ceramics, bioactive glasses), polymers (natural or synthetic) and composites. Magnesium and its alloys [3] are a rare example of biodegradable metals, which could potentially be used for tissue engineering scaffolds. But these metallic scaffolds do not show any bioactivity, during degradation hydrogen is released and they prove to be too stiff (E $\approx$ 45 GPa), making them less desirable. Other inorganic materials such as calcium phosphates, bioactive glasses (BAG) [4] and hydroxyapatite [5] (referred to also as "ceramic" materials), are also very stiff and brittle on their own, but preferred for their bioactivity.

Many polymers are biocompatible, degradable and have good processability. Most common natural polymers are silk [6], [7], collagen [8], gelatin [9], gellan gum [10], [11], and others [12], [13]. Although all these natural polymers are biocompatible and biodegradable, they usually exhibit low elastic modulus (typically $<$1 MPa) and low strength. On the other hand synthetic polymers like polyamide66 [14], polyacrylamide [15] and polyurethanes (PURs) [12], have higher mechanical properties, but are not biodegradable.

Due to inadequate behaviour of both above-mentioned groups of materials, recent research is more oriented in development of polymer-'ceramic' composites. This makes sense assuming elasticity of polymers and bioactivity of 'ceramics' can be merged [8], [11], [14].

As it turns out, addition of ceramics or bioactive glass to a polymer matrix does improve mechanical properties. Focus of this work is on a composite material composed of a natural polymer gellan gum (GG) and bioactive glass (BAG) particles.

1.2.1 Gellan gum

Gellan gum (GG) is a microbial water-soluble anionic polysaccharide derived from Sphingomonas paucimobilis. It was identified in 1978 by CP Kelco (San Diego, USA) during a large scale screening operation to identify polysaccharides from the soil and water bacteria useful rheological properties [16]. Since then it has been used as a texture modifier to tailor viscoelasticity in the food industry and as a culture medium in biotechnology because it forms a transparent gel that is resistant to heat and acid in the presence of calcium chloride [17].

Chemically, GG is a linear polymer with a tetrasaccharide repeating sequence which consists of two residues of β-D-glucose, one of β-D-glucuronate and one of α- L- rhamnose (Figure 1.2). The native poly-saccharide, as it is biosynthesised as a high-acyl GG, has an L-glyceryl substituent on O(2) of the 3-linked glucose residue of the tetrasaccharide sequence and, in at least some of the repeat units, an acetyl group at O(6) of the same residue. In normal commercial production, however, both types of substituent are removed by treatment of the fermentation broth with hot alkali. The resulting deacylated polymer is known generically as 'gellan gum' or low acyl GG [16].

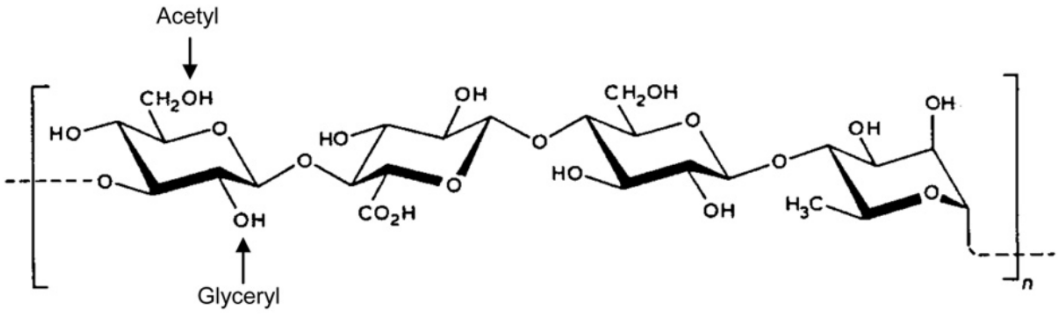


Figure 1.2: Chemical structure of gellan gum.

In 1996, Miyoshi [18] proposed folding mechanisms of GG molecules (Figure 1.3) based on the results obtained by DSC (Differential scanning calorimetry) and rheometry. At an elevated temperature, GG molecules form random coil structures in a water solution. When temperature is decreased, molecules start to form double helices. If the concentration of the GG is less than 2 wt. %, helices can form aggregates, whereas above 2 wt. % a more ordered structure can form, i.e. weak gel is formed. With the addition of positively charged ions, stronger gel can be obtained and at lower concentration of GG in water.

Crosslinking of gellan gum with the addition of Ca^{2+} makes for a stronger gel at lower concentrations of GG. Ca^{2+} ions lead to the formation of ionic bonds between the carboxyl groups between the gellan gum molecules in double helices [20]. It was also shown that monovalent ions also crosslink gellan gum, however, the effect of divalent ions is more promeinent [18].

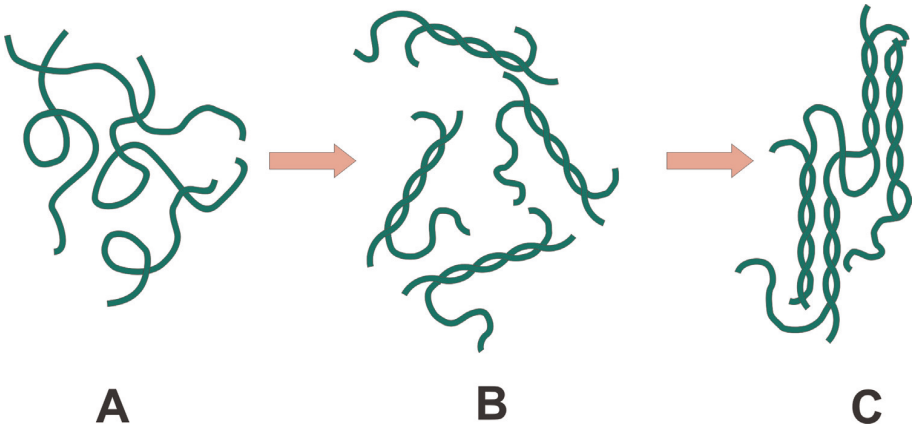


Figure 1.3: Schematic representation of GG structure during cooling and formation of double helices [19].

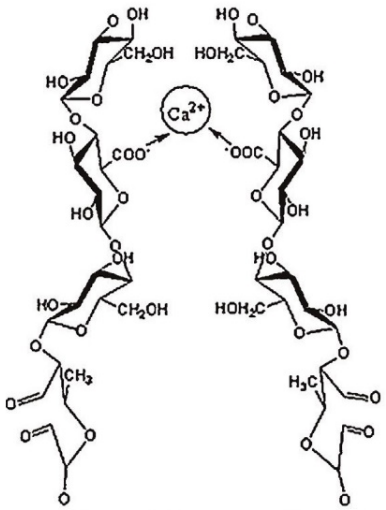


Figure 1.4: Crosslinking of GG double helices with additional Ca^{2+} [19].

1.2.2 Bioactive glass (BAG)

Bioactive glass (BAG) was found to be a promising material for tissue regeneration [21]. It has been extensively studied in the field of bone tissue engineering [22], due to hydroxyapatite layer formation on the surface of BAG scaffolds. This in terms enhances bone tissue regeneration [23] making it a very appealing bioactive material. On top of this, it exhibits high elastic moduli that are comparable to the one of bone. This can be seen as a beneficial mechanical property, however when a porous BAG scaffold is deformed, it experiences high stresses. The combination of high stresses and its inherent brittleness results in scaffolds that are unreliable for any kind of loadbearing applications. Therefore, a lot of effort is put into reducing brittles of BAG by tailoring its chemical structure or combining it with polymer to make composite scaffolds.

A lot of research is now focused in making BAG particles embedded in a polymer matrix. Choosing different polymers we can tailor mechanical properties of composite scaffolds to also be applicable for tissue regeneration. Recent work has shown that BAG

can promote angiogenesis that is crucial to numerous applications in tissue regeneration, such as neovascularization for bone regeneration and healing of soft tissue wounds [22].

1.2.3 Mechanical properties of materials

Polymers in general exhibit viscoelastic behavior due to their nature of molecular rearrangement when subjected to the external stress. In order to understand this we have to consider 'Theory of linear elasticity'. Linear elasticity can be explained by the first law of thermodynamics (FLT). For a closed system, the change in internal energy ΔU is considered a combination of work done on the system (W) and heat added to the system (Q):

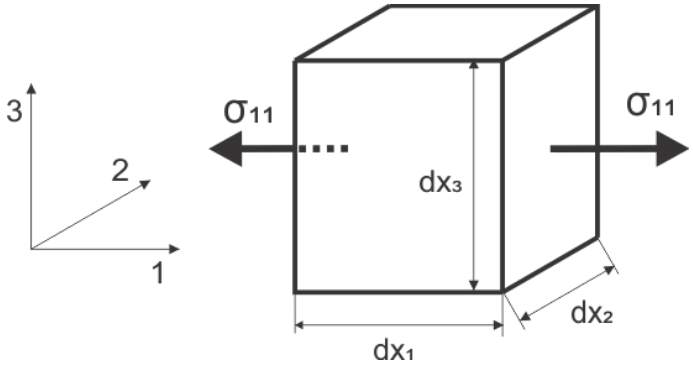


Figure 1.5: Small volume element.

We start with a simple system of observation, a small volume element (Figure 1.5). Therefore, we can write the expression in the following way:

$$du = dw + dq \tag{1.1}$$

where dw is work done on the volume element. If an outside normal force F_{11} is exerted only on the element along the first axis, this volumetric work can be expressed in terms of strain energy:

$$dw = F_{11}(dx_1' - dx_1) = d\sigma_{11}dx_2dx_3d\epsilon_{11}dx_1 = d\sigma_{11}d\epsilon_{11}dV \tag{1.2}$$

Assuming the thermal process is reversible, dq from the FLT equation for a small element is heat absorbed by the material, which can be written in the following way:

$$dq = TdS \tag{1.3}$$

where T is the temperature and dS is change in entropy of the material volume element. These relations give us the following expression:

$$du = dVd\sigma d\epsilon + TdS \tag{1.4}$$

To correlate the derived equation to an elastic modulus, one needs to solve the previous equation for the stress and derive stress with respect to strain:

$$d\sigma = \frac{1}{dV}\frac{du}{d\epsilon} - \frac{T}{dV}\frac{dS}{d\epsilon} \tag{1.5}$$

$$E = \frac{d\sigma}{d\epsilon} = \frac{1}{dV}\frac{d^2u}{d^2\epsilon} - \frac{T}{dV}\frac{d^2S}{d^2\epsilon} \tag{1.6}$$

Elastic modulus is therefore related to the change in internal energy and change of entropy of the material. Depending on the type of material, one or the other can prevail. It is also obvious from the equation that for some materials changing the temperature can have an effect on which of the contributions will be prominent. If we lower the temperature enough, internal energy will have a bigger effect, and vice versa. This is the case with polymers, they can exhibit either internal energy driven elasticity or entropy driven elasticity. This is not determined only by the temperature, but also pressure, dissolution, etc. which all change the mobility of the polymer molecules.

The point at which elastic behavior changes from internal energy to entropy driven elasticity is known as glass transition temperature [24]. Polymers with internal energy driven elasticity are below glass transition temperature and are in a so-called glassy state, whereas polymers above glass transition temperature have more molecular mobility therefore exhibit entropy driven elasticity and are in rubbery state. Mobility of molecules of a polymer in a glassy state is restricted to vibrations of atoms or bonds and reorientation of small groups of atoms. However, when a polymer is in a rubbery state, molecular mobility increases to motion and rotation of molecular segments. Also amplitude, frequency and rate of movements, as well as their sensitivity to temperature increases.

Polymers in rubbery state therefore have viscoelastic properties. Characterization of such materials is more complex, due to time dependence i.e. relaxation of polymers under external load. Viscoelastic behavior can be characterized by a time-dependent modulus ($G_{(t)}$) or by frequency-dependent moduli (G' and G''). Time- and frequency-dependent properties of a material can be interconverted from one to the other using developed mathematical relations [25], [26]. However, frequency dependence is most commonly used to characterize viscoelastic materials, due to the amount of data one can obtain in a certain amount of time.

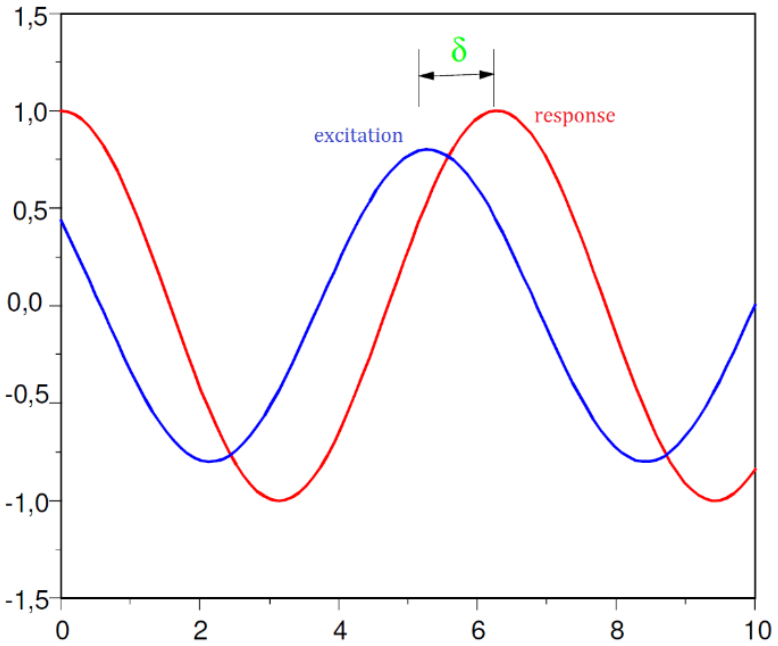


Figure 1.6: Sinusoidal wave forms of excitation and response during rheological measurement.

Frequency-dependent properties are obtained using small amplitude oscillatory measurements. Most commonly, such measurements are done on a rheometer, where small

amplitude oscillatory shear (SAOS) properties are measured, where material is excited by an oscillating shear displacement and the responding force is measured (Figure 1.6). The intensity of the response is proportional to the shear complex modulus (G^*), while the horizontal shift between excitation and response wave represents the damping factor (δ). From these two, we can calculate G' (storage or elastic shear modulus) and G'' (loss or dissipative shear modulus) in the following way:

$$G' = G^* \cos(\delta) \tag{1.7}$$

$$G'' = G^* \sin(\delta) \tag{1.8}$$

Viscoelastic moduli depend on the frequency of excitation, amplitude of deformation, pressure, temperature, etc. Storage modulus (G' in shear test) provides information on the stored energy during deformation that is released upon removal of the force, while loss modulus (G'' in shear test) gives insight on dissipation of energy in the material. Ratio between G' and G'' is defined by a damping factor ($\tan(\delta) = \frac{G''}{G'}$) which gives information on the state of material. Material with high damping factor ($\tan(\delta) >> 1$) behaves as a solid, small damping factor ($\tan(\delta) << 1$) behaves as a liquid and when damping factor is close to one ($\tan(\delta) \gtrapprox 1$) material behaves viscoelastic. This gives an opportunity to observe material's melting point, softening or gelation. These phenomena can be observed over time, by changing temperature or by other means. The following Figure 1.7 shows the change of viscoelastic properties of two polymers of the same type with different densities of crosslinks. Because their polymer chains are of the same chemical composition, viscoelastic properties in glassy region are overlapping. With increasing temperature the mobility of the chains also increases, at which point the different densities of crosslinks come into play by restricting the mobility of the polymer network. The polymer network with higher crosslinking density is more restricted and thus shows higher moduli and vice versa.

In Figure 1.7 viscoelastic moduli is marked as G in brackets and as E. This represents different types of deformation, where shear deformation is marked with G and uniaxial compression or tension is marked with E. In both types of deformation, we can induce constant deformation and obtain time dependant moduli ($G_{(t)}$ and $E_{(t)}$) or oscillatory deformation and obtain storage (G' and E') and loss (G'' and E'') moduli.

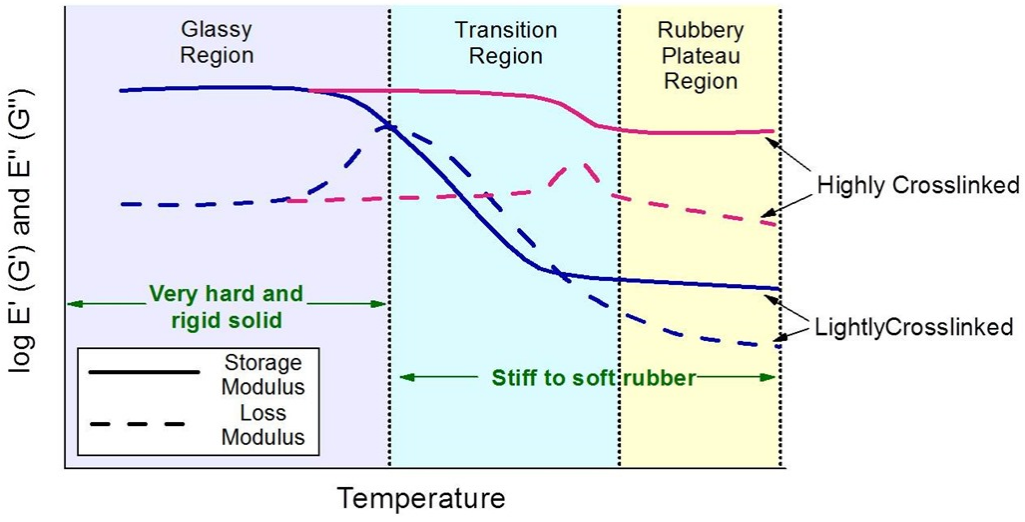


Figure 1.7: Master curve of highly and lightly crosslinked polymer [27].

When performing frequency sweep experiments, temperature and the amplitude of

deformation is kept constant while frequency is increased in logarithmic steps. This excites the measured material at different frequencies that can provide different responses over the measured frequency range. The shape and relation of the measured G' and G" can provide even more information. Figure 1.8 shows how different systems can be determined from rheological measurements over a range of frequencies, i.e. frequency sweep.

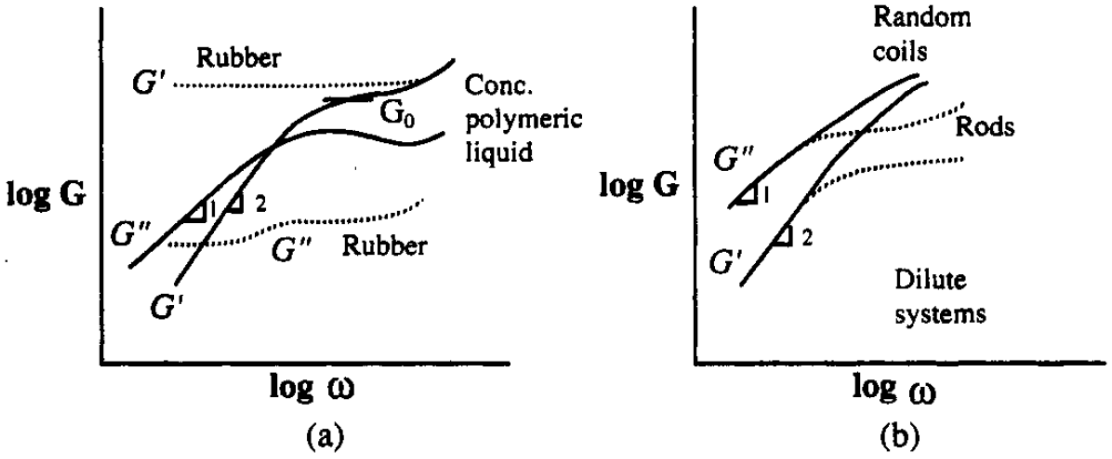


Figure 1.8: Typical behavior of the dynamic moduli for (a) rubber and concentrated polymeric liquids and (b) dilute solution of random coils and rod-like particles.

Hydrogels in general are always in rubbery state [28], because the water molecules increase mobility of the polymer network. Therefore, hydrogels always exhibit entropic elasticity. Only when dried, due to the lack of water molecules, polymer molecules stick together which reduces their mobility. This in terms turns their behavior to glassy-like, making them stiffer but more brittle.

1.2.4 Characterization of mechanical properties

Most commonly studied materials for scaffolds vary significantly in their mechanical response. Ranging from practically elastic inorganic materials (ceramics), to highly viscoelastic materials as polymers and their composites. Consequently many different techniques for measuring their mechanical properties are found in literature. Some techniques measure only quasi-static mechanical properties, whereas others also provide properties under dynamic loading that are physiologically relevant. In addition, during degradation of a scaffold, mechanical properties are changing. Therefore determination of essential material properties is needed.

Hydrogels are known to have complex mechanical properties, due to their polymer network and high content of water in them. Therefore, it is crucial to understand how such materials i.e. implants behave under different mechanical stimuli that would later occur in a body.

Hydrogels behave differently under stress and strain-induced deformations. In literature we most often find strain-induced tests of engineering materials, like uniaxial compression, indentation, bending test, etc. [29]. However, in real life, loadbearing implants are exposed to the weight of the patient's body, in other words to stress. One can understand this easily by exposing a hydrogel to a large constant strain or stress, in a non-linear deformation region. Under step-up strain, i.e. relaxation experiment, hydrogel will show an immediate stress increase and with time will relax down to a certain stress value. The relaxation is

time-dependent due to viscoelastic properties of polymer network in the hydrogel as well as flow of water in it. However, when we expose a hydrogel sample to a stress-up, i.e. creep experiment, hydrogel will first show immediate deformation followed by a time-dependent deformation. If the stress is high enough, deformation will not reach a plateau, but instead keep on deforming. This happens because of a high enough constant stress, water keeps on flowing out of the sample. This results in relaxation modulus (E^{∞}) and creep compliance (D^{∞}), which are not necessarily connected.

Therefore, we have studied different techniques that measure mechanical response of a material under different conditions and see if the results can be correlated for our hydrogel composites. Techniques that we tested were uniaxial compression, shear rheology, dynamic mechanical analysis, indentation and ultrasonic wave propagation. Each of the techniques differs from another, some in dimensions of the sample (from thickness of 0.4 mm to 11-12 mm), others in type of excitation (quasi-static, dynamic, ramp, etc.) and type of deformation (shear, uniaxial compression, indentation, etc.).

More precisely **monotonic uniaxial unconfined compression** is a common method for testing a variety of engineering materials. It is also used to characterize polymers for tissue engineering applications. During measurement the sample is compressed at a certain strain rate (strain-controlled measurement), stops at a predetermined deformation for a time to let the sample relax and then the sample is released i.e. stretched to the point where the stresses in the sample diminish to zero. In this way, we obtain different types of information of materials mechanical behavior. The most common data extracted is elastic or Young's modulus (E), which, in our case, is calculated from the initial linear part of the slope of the loading cycle in the stress-strain curve. This procedure assumes that the initial deformation corresponds to the pure elastic behavior of the material [30]. Unloading part of the curve gives us additional data on viscous dissipation, which is prominent with hydrogels.

Rheometry is a very useful technique for characterization of mechanical properties of liquids, solids, emulsions, polymers, gels, etc. Depending on the material and sample fixture, it can measure viscosity, elasticity and viscous dissipation, relaxation, creep, gelation, melting/solidification, polymerization, and many other material properties. Standard rheometers measure deformation in shear, but there are also special fixtures for measuring extensional rheology. In this work, we use a standard shear rheometer to measure our hydrogels and hydrogel composites. Although shear is not a predominant type of deformation of tissue engineering scaffolds, it gives us an insight on the relative difference of mechanical properties among different compositions and on gelation of samples.

Dynamic mechanical analysis (DMA) is a technique similar to rheometry. Dynamic mechanical analyzer induces sinusoidal deformation on the sample, from which elastic and dissipative moduli are obtained. Some DMA can also measure creep and relaxation. The main difference between rheometry and DMA is that the latter is primarily constructed to induce uniaxial (compression or tension) deformation on the sample, whereas rheometry induces torsional shear deformation. Consequently, DMA is more convenient to induce compression, tension as well as bending deformation, making it more suitable to measure solid samples. However, there are also specific sample fixtures that allow shear deformation and can be used to measure liquids with higher viscosity.

Both techniques, rheometry and DMA, can perform several experiments in a similar manner. Frequency sweep, amplitude sweep and temperature sweep can all be performed on both machines. Rheometers are primarily constructed to perform measurements in shear, because of the rotational motor which induces deformation. However, there are also additional sample holders for tension, while no compression holders are available. On the other hand, DMA is mainly intendent to measure samples in compression, tension or

bending, due to its linear motor. However, with a specific sample holder it can also measure shear, but usually requires two identical samples that have high viscosity or are viscoelastic. To sum up, both of the techniques are mainly aimed at measuring viscoelastic materials, however rheometers are mainly intended to measure samples in shear, while DMA for other forms of deformation.

Indentation is a technique used primarily to measure indentation hardness of a material. It relies on measuring indentation depth of a tip depending on the amount of force that was put on the tip. Depending on the type of a material, we might choose a different indentation test. Indentation tests first differ on the volume of deformation of the sample under the tip: macro-, micro- or nano-indentation. The deformation volume is proportional to the applied force, but also depends on the geometry of the tip. Micro- and nano-indentation of harder materials (steel, ceramics, etc.) usually relies on sharp tips shaped like a pyramid with different angles (Vickers or Knoop hardness). For softer materials like thermoplastic polymers, wood, elastomers, etc., tips with different geometries are used. The most common ones are spherical tip (Brinell, Rockwell or Shore C hardness) or with a truncated cone (Shore A). This in terms reduces local stress at the tip, avoiding damage of the sample's surface.

Using a more sophisticated hardness measuring device that has a controlled strain deformation, we can obtain a stress-strain curve similar to the one obtained with a compression test. However, we need to keep in mind that indentation stress-strain curve is far from the one obtained by compression test, and cannot be compared, due to the following reasons. Tip geometries like pyramid and sphere increase the surface with which they exert force on the sample during indentation, decreasing applied stress on the sample during indentation. The second reason is that deformation under the tip is non-uniform. Under the tip, there are higher shear and compression stresses, whereas along the surface around the tip the material is stretched. Deeper into the sample, the stresses slowly diminish, and as a rule of thumb it is said that the material is deformed 10 times deeper than the depth of the indenter tip. Because of such differences in stresses, a crack in the material can occur under the tip, especially with harder materials like metals and ceramics.

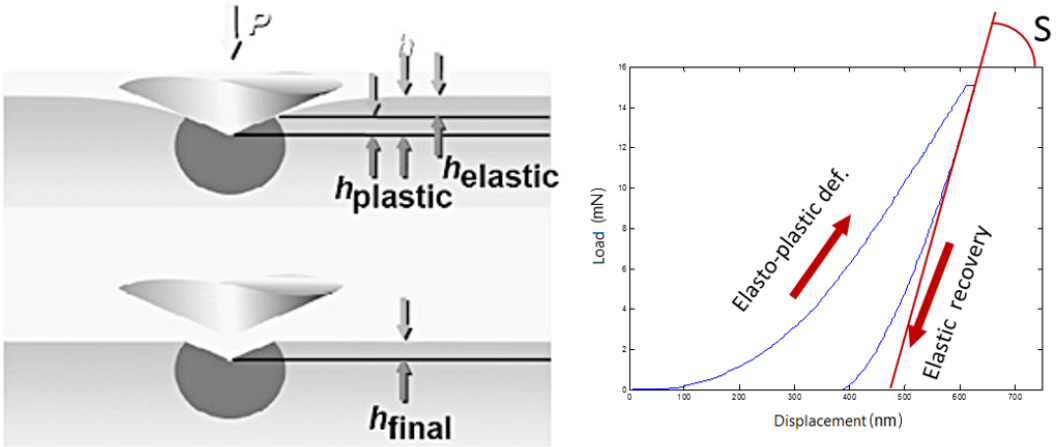


Figure 1.9: Sketch of a deformed sample's surface during and after indentation (a) and the load-displacement curve of the experiment (b).

Indentation is mostly used to measure hardness of the material, but it can also be used to measure elastic modulus (E) of materials. Unlike with uniaxial compression where

E is obtained at the beginning of the loading curve, with indentation we extract the E_r (reduced elastic modulus) from the unloading curve (Figure 1.9) using Equation 1.9. Unloading curve is selected in order to avoid the measuring fracture of the material and assuming we are in a linear region. As stated in the previous paragraph, during loading of indenter tip both elastic deformation and cracking. However, when unloading the tip, it is assumed that initially only elastic deformation is the cause of force decrease. In equation, β is a geometric constant specific for the tip used, and A_p is the projected area of the indentation. By providing additional data like Poisson's ratio of the sample $\upsilon_s = 0.255$ and data of the diamond tip ($E_i = 1150GPa$ and $\upsilon_i = 0,07$), elastic modulus of the sample E can be calculated according to Equation 1.10b from Oliver and Pharr [31].

$$E_r = \frac{1}{\beta}\frac{\sqrt{\phi}}{2}\frac{S}{\sqrt{A_p}} \tag{1.9}$$

$$1/E_r = (1 - {\upsilon_i}^2)/E_i + (1 - {\upsilon_s}^2)/E \tag{1.10}$$

Ultrasonic wave propagation also known as acoustic measurement is a technique where mechanical properties of a material are calculated from the speed of sound in the material. It is a very appealing technique, because it is a non-destructive technique that measures bulk mechanical properties of a material. Using different transducers, we can obtain a whole stiffness matrix of the sample. Frequencies in the range of kHz to GHz are usually used, but results can differ with different frequencies. Most often speed of longitudinal and transversal waves is recorded, each one of them providing different information. Longitudinal waves propagate in all states of matter (solid, liquid and gas) and refers to displacement of the medium in the direction of the medium. A common example for longitudinal waves is the sound that we hear. On the other hand, we can also induce transversal waves that only propagate in solids (elastic or viscoelastic materials), where displacement of the medium is perpendicular to the direction of propagation.

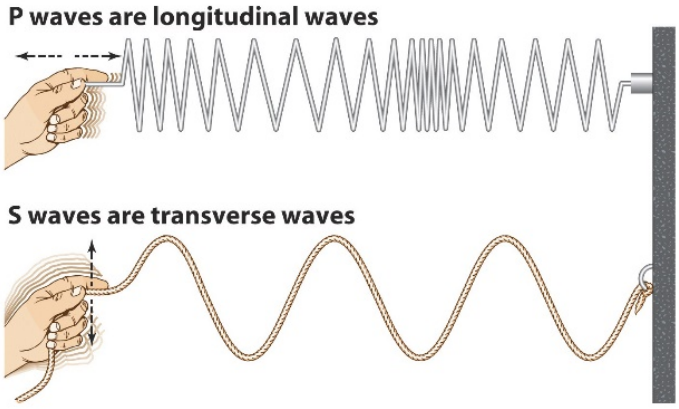


Figure 1.10: Example of longitudinal and transversal wave propagation [32].

To understand acoustic measurements, we need to understand what a stiffness matrix is and how it connects to elastic moduli. First, we need to start with a Generalized Hook's Law:

$$\sigma_{ij} = C_{ijkl}\epsilon_{kl} \tag{1.11}$$

where C_{ijkl} is a fourth-order stiffness tensor of a material or elastic moduli. Such a tensor has 81 and 16 components for a three- and two-dimensional problem, respectively.

For an orthotropic material that is exposed to a uniaxial strain state, stiffness matrix can be significantly simplified [33]:

$$\begin{bmatrix} \sigma_{11} \\ \sigma_{22} \\ \sigma_{33} \\ \sqrt{2}\sigma_{23} \\ \sqrt{2}\sigma_{13} \\ \sqrt{2}\sigma_{12} \end{bmatrix} = \begin{bmatrix} C_{1111} & C_{1122} & C_{1133} & 0 & 0 & 0 \\ C_{2211} & C_{2222} & C_{2233} & 0 & 0 & 0 \\ C_{3311} & C_{3322} & C_{3333} & 0 & 0 & 0 \\ 0 & 0 & 0 & 2C_{2323} & 0 & 0 \\ 0 & 0 & 0 & 0 & 2C_{1313} & 0 \\ 0 & 0 & 0 & 0 & 0 & 2C_{1212} \end{bmatrix} \begin{bmatrix} \epsilon_{11} \\ \epsilon_{22} \\ \epsilon_{33} \\ \sqrt{2}\epsilon_{23} \\ \sqrt{2}\epsilon_{13} \\ \sqrt{2}\epsilon_{12} \end{bmatrix} \tag{1.12}$$

$$C_{2211} = C_{1122} \tag{1.13}$$

$$C_{3311} = C_{1133} \tag{1.14}$$

$$C_{3322} = C_{2233} \tag{1.15}$$

Since the materials studied in this work have no specific orientation in their structure, they can be considered as an isotropic material, reducing stiffness matrix down to components C_{1111} and C_{1212}, where $C_{1122} = C_{1111} - C_{1212}$.

$$\begin{bmatrix} \sigma_{11} \\ \sigma_{22} \\ \sigma_{33} \\ \sqrt{2}\sigma_{23} \\ \sqrt{2}\sigma_{13} \\ \sqrt{2}\sigma_{12} \end{bmatrix} = \begin{bmatrix} C_{1111} & C_{1122} & C_{1122} & 0 & 0 & 0 \\ C_{1122} & C_{1111} & C_{1122} & 0 & 0 & 0 \\ C_{1122} & C_{1122} & C_{1111} & 0 & 0 & 0 \\ 0 & 0 & 0 & 2C_{1212} & 0 & 0 \\ 0 & 0 & 0 & 0 & 2C_{1212} & 0 \\ 0 & 0 & 0 & 0 & 0 & 2C_{1212} \end{bmatrix} \begin{bmatrix} \epsilon_{11} \\ \epsilon_{22} \\ \epsilon_{33} \\ \sqrt{2}\epsilon_{23} \\ \sqrt{2}\epsilon_{13} \\ \sqrt{2}\epsilon_{12} \end{bmatrix} \tag{1.16}$$

This also means that by knowing these two components we can compute all material constants for such a material, like Young's modulus E, Poisson's ratio υ, bulk modulus K and shear modulus G, as:

$$E = \frac{C_{1212}(3C_{1111} - 4C_{1212})}{C_{1111} - C_{1212}} \tag{1.17}$$

$$\upsilon = \frac{C_{1111} - 2C_{1212}}{2(C_{1111} - C_{1212})} \tag{1.18}$$

$$K = C_{1111} - \frac{4}{3}C_{1212} \tag{1.19}$$

$$G = C_{1212} \tag{1.20}$$

Both stiffness components C_{1111} and C_{1212} can be calculated by knowing speed of ultrasonic wave propagation and density of the material:

$$C_{1111} = \rho {v_l}^2 \tag{1.21}$$

$$C_{1212} = \rho {v_t}^2 \tag{1.22}$$

where ρ is density of the material and v_l and v_t speed of longitudinal and transversal wave propagation, respectively. This implies that besides measuring speed of sound propagation, knowing density is also crucial.

1.3 Shaping Techniques for Producing Porous 3D Scaffolds

Three-dimensional tissue-engineering scaffolds need a porous structure in which cells will be able to attach, proliferate and differentiate. The first requirement is that the porosity needs to be open, meaning that pores are interconnected. This allows us to seed the cells not only on the surface of the scaffold, but also in the deeper parts of the scaffold. This is especially important in parts where all three dimensions have bigger dimensions, whereas it is less important for 2D sheet like scaffolds. Being able to seed the cells deeper reduces the time for the cells to overgrow the scaffold. The second reason for the open porosity is the possibility of nutrition and growth factors to flow through, so the cells can survive and form new tissue.

It is known that there is a critical range of pore size for scaffolds [34], but it depends on the cell type used and tissue being engineered. For bone tissue engineering, mean pore size of 325 μm is optimal [35]. Some sources [36] state that porosity should be greater than 70 % while others [12] that it should exceed 90 %.

Porosity of a scaffold can be achieved in several different ways. The method of making pores is firstly dictated by the material being used for the scaffold, whether it is metal, ceramic or polymeric [37]. Metallic scaffolds for instance can be made by sintering metallic fiber meshes, laser perforation, selective laser melting, acid etching, machining, etc. Ceramic scaffolds are mainly done by casting into a sacrificial polymer, foaming or salt leaching. Polymers on the other hand can be made porous in many different ways, however the most appropriate technique usually determined by the material. The most common techniques are freeze-drying, melt spinning, electrospinning, foaming, salt leaching, 3D printing, etc. Some of the techniques can be used together, one after another (e.g. 3D printing and freeze-drying afterwards). Hydrogels have a large amount of water, which makes them suitable to use for freeze-drying since the water freezes and creates large open pores.

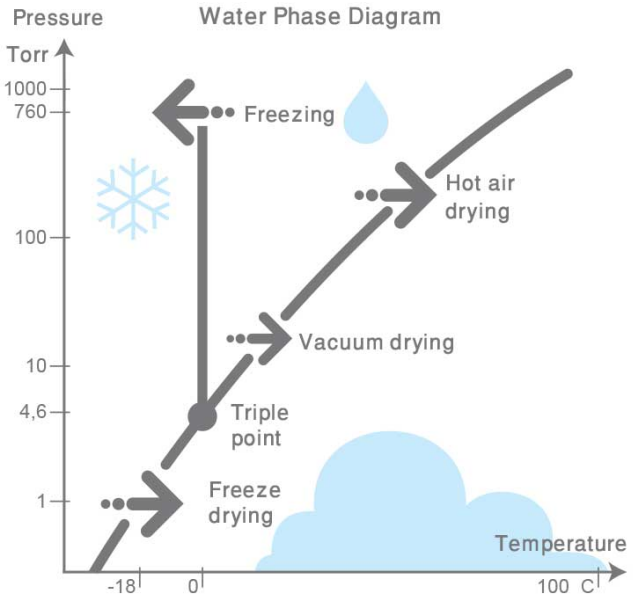


Figure 1.11: Phase diagram of water [38].

1.3.1 Freeze-drying

Freeze-drying is a quick and, at first glance, a very easy process. The process is based on removing water and keeping the polymer network. The process (1.11) starts with freezing a hydrogel sample. The unbound water in the hydrogel forms ice crystals that will dictate the shape of pores later on. In order to sublimate the ice crystals, the pressure has to be lowered below the water's triple point and then the temperature raised back to the ambient. In this way, the frozen ice crystals are removed, leaving a porous, foamy-like structure.

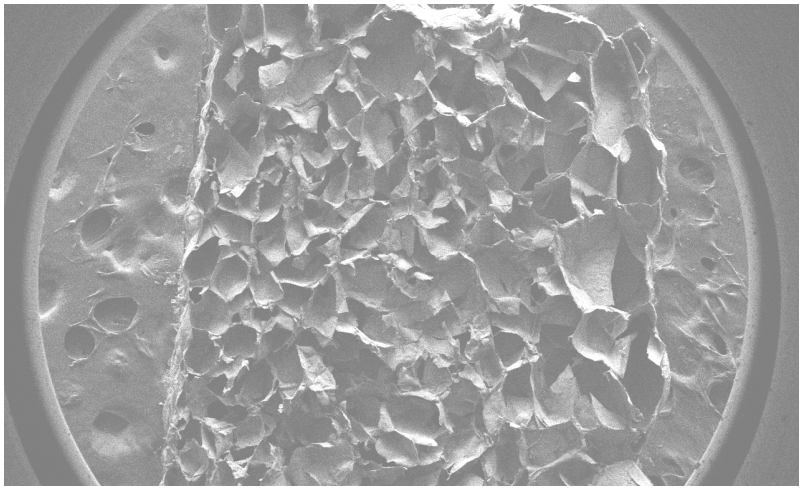


Figure 1.12: SEM picture of a porous sample of GG hydrogel after freeze-drying.

The process of freeze-drying is straightforward, but as it turns out there are many parameters affecting the final porosity (freezing speed, nucleation points in the material, sublimation parameters, etc.), some of which are hard to control [13].

1.3.2 Additive manufacturing

Significant advances of additive manufacturing or 3D printing techniques have happened in the last years. We came to the point where we can print molds for complex parts, make iteration of prototypes much faster or even print functional parts. Not only are there large industrial 3D printers, but also affordable 3D printers that almost anybody can have at home. We can print plastic, gypsum, concrete, metal and in recent years, printing organs and tissues caught attention of my researcher groups [39]. However, the principle of 3D printing was first mentioned in the 70's by a Slovene physicist Prof. Dr. Igor Grabec. This is the first patent [40] mentioning a possibility of a three-dimensional printer and it looked very similar to the laminated object manufacturing method, where flat sheets of a material are cut and then stacked one on top of each other (Figure 1.13). Prof. Grabec has foreseen the use of polystyrene foam sheets, whereas today paper is used that allows for higher precision of final products. The issue at that time was that technology was not yet at the point where such an invention could be realized [41].

In 1983, first SLA (stereolithography apparatus) was made by the soon-to-come company 3Dsystems. In the following years, additive manufacturing has evolved and several different 3D printing processes are available now. Choosing the right process is crucial and depends on several parameters like material for printing, required precision of the final product, speed of printing, required complexity of the product and the cost of the 3D printer. Common types of additive manufacturing techniques are listed in Table 1.1.

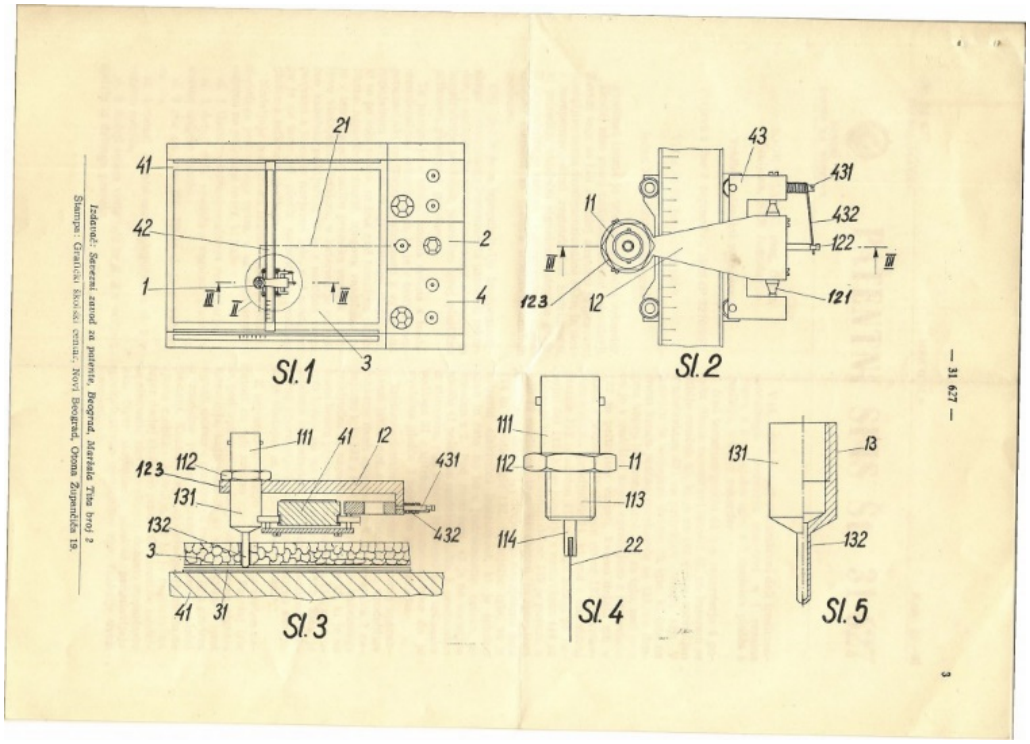


Figure 1.13: Patented design idea of a 3D printed from Prof. Grabec [42].

Table 1.1: Additive manufacturing techniques [43].

Type	Technologies
Extrusion	Fused deposition modeling (FDM) or Fused filament fabrication (FFF) Robocasting or Direct Ink Writing (DIW)
Light polymerization	Stereolithography (SLA) Digital Light Processing (DLP)
Powder Bed	Powder bed and inkjet 3D printing (3DP) Electron-beam melting (EBM) Selective laser melting (SLM) Selective heat sintering (SHS) Selective laser sintering (SLS) Direct metal laser sintering (DMLS)
Laminated	Laminated object manufacturing (LOM)
Powder fed	Directed Energy Deposition
Wire	Electron beam freeform fabrication

Bioprinting has also shown a lot of potential as a specific branch of additive manufacturing. It is often stated that bioprinting refers to 3D printing living organs, which can be misleading. Tissues cannot be directly printed, as it needs a certain time to grow on its own. Bioprinting refers to additive manufacturing of 3D porous structures or scaffolds that act as temporary supports for the cells to live and proliferate in. Meaning that bioprinting is only the first step of constructing new organs. After the scaffold is made using a bioprinter, cells are seeded on it and then everything is put into a bioreactor, where nu-

trition and other stimuli are added to make cells differentiate. The most commonly used techniques for 3D printing scaffolds range from 3DP and SLS for ceramic scaffolds, SLM for metallic and FFF for hydrogel scaffolds. The latter ones are usually stored in a syringe as a water solution of a polymer (Figure 1.14). Such solutions must then solidify when extruded from the syringe, which can be done in different ways depending on the material. Some materials solidify or crosslink under UV light, others upon cooling down and some by crosslinking agents.

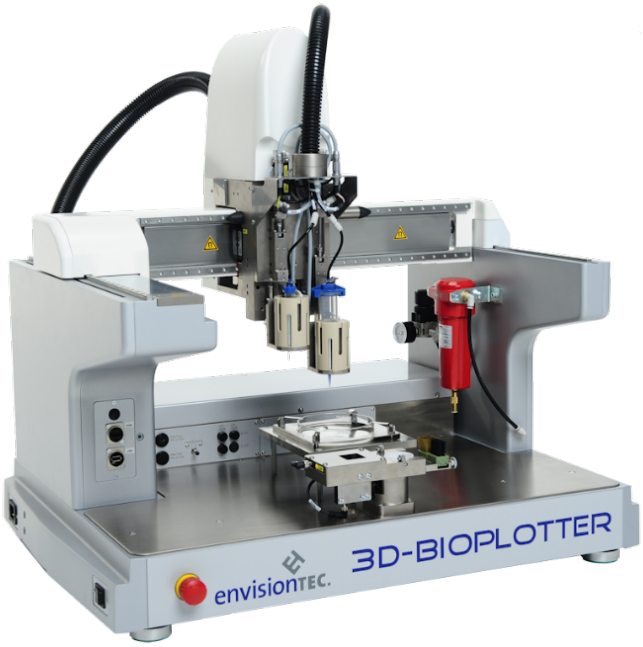


Figure 1.14: 3D bioprinter EnvisionTEC.

Chapter 2

Aim and Hypothesis

Tissue engineering scaffolds have a role of temporary support and providing an environment for stem cells and newly grown tissue. Meaning that a scaffold is not only to provide a certain level of mechanical stiffness, but also to maintain its mechanical stiffness until the newly grown tissue replaces it. Replacing different organs and in different patients requires scaffolds with tailored mechanical properties for each individual case. Mechanical properties of materials for tissue engineering scaffolds are often characterized with different techniques, which are difficult to compare, especially due to complex viscoelastic properties of materials used for scaffolds. Moreover, there is even less known on how mechanical properties change during degradation.

The aim of this work is to verify which technique is the most suitable for measuring mechanical properties of hydrogel-composite materials used for tissue engineering scaffolds. Gellan gum (GG) and bioactive glass particles (BAG) were the materials that we chose for this work. The most suitable technique will be used to measure mechanical properties of these hydrogel-composite samples during a long term submersion in simulated bodily fluid (SBF) to assess degradation. All the samples measured were in the form of a hydrogel, without porosity in order to eliminate the uncertainty of measurements due to the induced porosity.

The first hypothesis of this work was that the polymer-based scaffold made of GG would **degrade during submersion in simulated bodily fluid** (SBF). This would simulate degradation of the scaffold without interference of stem cells and newly grown tissue.

Because of the addition of BAG in the GG hydrogel, the **mechanical properties were expected to improve**. Since GG hydrogel on its own is too weak to serve as a scaffold, it needs to be reinforced. Tailoring mechanical properties for specific patients could also be done by adjusting the amount of BAG particles added to a scaffold.

During submersion of samples in SBF, **formation of hydroxyapatite (HA) is expected, which should consequently reinforce the scaffold**. To reliably follow the changes of mechanical properties of a scaffold, we had to first choose the most appropriate technique to measure scaffold's mechanical properties. Polymer matrix by itself implies that the scaffold will exhibit a viscoelastic and non-linear response that the measuring technique should be able to capture and quantify.

In order to make patient-specific scaffolds, it would be helpful **to be able to 3D print GG hydrogel composites**. Since each wound is different, making scaffolds that fit each patient is a plus.

Chapter 3

Materials and Methods

3.1 Materials

3.1.1 Gellan gum and BAG composites

Samples were prepared with a polysaccharide gellan gum (GG). The polymer in the form of a powder (Sigma, USA) was dissolved with the help of magnetic stirrer in ultrapure water (MilliQ), which was preheated to 90 $°C$. Different amounts of GG powder were added to water to find a compromise between stiffness of the final hydrogel and easiness of preparation. The latter one depends upon the time for the GG powder to dissolve in water. We were able to go up to 4.0 $wt.$ % of GG, but the solubility of the powder and homogeneity of the samples was at question. Final concentration of 2.0 $wt.$ % was chosen.

With a purpose of increasing mechanical properties and bioactivity of GG hydrogel, bioactive glass (BAG) powder was added. Sodium-free BAG was synthesized using a sol gel technique [4], with a composition of 70 $wt.$ % SiO_2 and 30 $wt.$ % CaO. The BAG particles have an approximate size of 100 nm (Figure 3.1A) that are known to cluster and form 10 μm large agglomerates (Figure 3.1F).

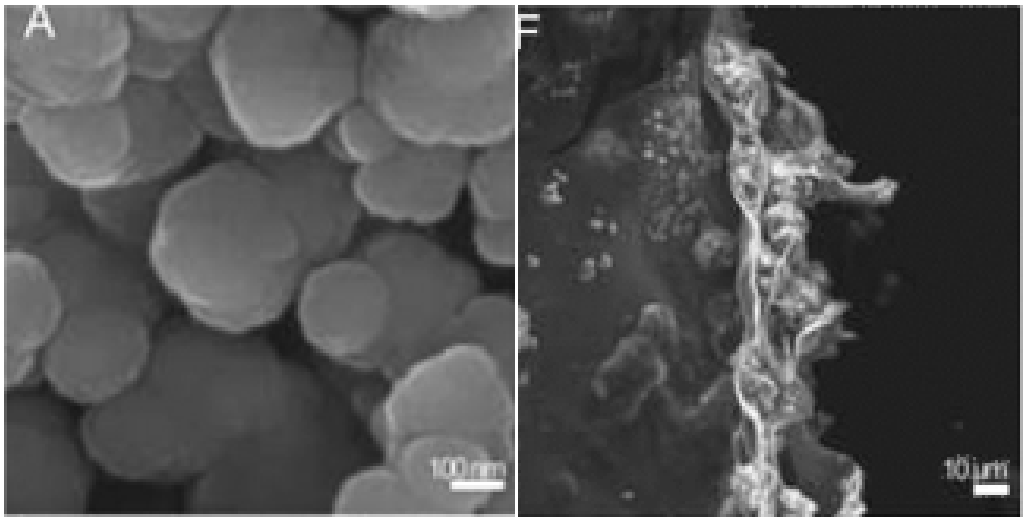


Figure 3.1: SEM micrograph of BAG particles (A) and agglomerates of BAG on hydrogel scaffold (F)[11].

The GG and BAG composites were prepared by adding up to 8.0 $wt.$ % of BAG powder into a solution of 2 $wt.$ % of GG (see Table 3.1) and sonicating with high power sonicator

(Hielscher UP400S, Germany) to disperse and de-agglomerate the BAG particles. Depending on the characterization method used later, hydrogel samples were either prepared in advance or poured as a suspension in a measuring device and gelled there (in the case of rheological tests). The samples that were prepared in advance were poured as a hot suspension of BAG and GG into a preheated Petri dish. After cooling down to room temperature, the suspension gelled, and the samples were cut out using a punch with 6 mm or 12 mm diameter, depending on the measurements they were used for. The height of the cylindrical samples was around 4 mm. For the sake of simplicity, we have assigned all the composite samples with the following names that represent BAG to GG weight ratio, keeping the amount of GG in water constant (Table 3.1).

Table 3.1: Composite samples of GG hydrogel and BAG particles.

Name	GG ($wt.$ %)	BAG ($wt.$ %)	BAG/GG ( )
H0	2	0	0
H1	2	2	1
H2	2	4	2
H3	2	6	3
H4	2	8	4

Mechanical properties of BAG were measured by making sintered cylindrically shaped samples of BAG powder. To get a suitable sample, we compressed BAG powder at 20 bars in a die, which had a diameter of 6.0 mm and height of 11 ± 1 mm. The 'green samples' were then sintered with a heating rate of 3.3 $°C/min$ from room temperature to 850 $°C$, holding this temperature for 2 hours and cooled down to 6.6 $°C$. This ensured that the BAG particles fused together and stayed in amorphous form.

3.1.2 Gellan gum with $CaCl_2$

For comparison to the GG and BAG composites, $CaCl_2$ was added to the 2 $wt.$ % GG solution without BAG. This was done to compare the resulting gelation temperature and the final stiffness of the samples. The amount of $CaCl_2$ was initially chosen from the Ph.D. work of Dr. Gantar [44] at 0.03 $wt.$ % and increased for other compositions (Table 3.2).

Table 3.2: Samples of GG hydrogel and $CaCl_2$.

Name	GG ($wt.$ %)	BAG ($wt.$ %)	BAG/GG ()	Ca ($wt.$ %)	Ca (mM)
H0	2	0	0	0	0
H0Ca1	2	2	1	0.03	2.7
H0Ca2	2	4	2	0.06	5.4
H0Ca3	2	6	3	0.09	8.1
H0Ca4	2	8	4	0.12	10.8
H0Ca5	2	8	4	0.18	16.2
H0Ca6	2	8	4	0.24	21.6

3.1.3 Simulated bodily fluid

Degradation tests were performed in simulated bodily fluid that was prepared from Hanks' Balanced Salt Solution or HBSS (Sigma Aldrich, USA). Looking at the table below (Table 3.3), HBSS does not have enough Ca^{2+} ions compared to blood plasma. Therefore, we added 137 mg of $CaCl_2$ in a 1 l of HBSS, to increase the total amount of Ca^{2+} ions to 5.0 mM. The resulting solution i.e. modified HBSS was used for the degradation experiments and was referred to as SBF.

Table 3.3: Nominal ion concentrations (mM) blood plasma, Original SBF [45], HBSS and modified HBSS.

	Blood plasma	Original SBF	HBSS	Modified HBSS
Na^+	142.0	142.0	142.6	142.6
K^+	5.0	5.0	5.77	5.77
Mg^{2+}	1.5	1.5	0.91	0.91
Ca^{2+}	2.5	2.5	1.26	2.5
Cl^-	103.0	147.8	146.85	148.09
HCO_3^-	27.0	4.2	4.0	4.0
HPO_4^{2-}	1.0	1.0	0.74	0.74
SO_4^{2-}	0.5	0.5	0.41	0.41

3.2 Characterization of Viscoelastic Properties of Hydrogel Composites

3.2.1 Uniaxial compression

Samples with 11.9±0.1 mm of diameter and 11.5±0.6 mm of height were tested in uniaxial unconfined compression at room temperature (22 $°C$), with the universal testing machine (Galdabini Quasar 50, Italy), using 100 N load cell. The samples were not submerged in water during the experiments, since during the compression water was coming out of the sample, keeping the surface of the sample wet. The loading rate of compression was 0.2 mm/min, equivalent to a strain rate of the order of $\approx 3{*}10^{-4}$ $1/s$ [46]. Quasi-static Young's modulus (E) was determined from the initial slope of the stress-strain curve.

3.2.2 Rheometry

Rheological measurements were done on an AntonPaar MCR 301 (Austria) rheometer with a 50 mm cone and plate fixture, with a cone angle of 1°. The sample holder was preheated to 90 $°C$ as the suspension/solution sample. An exact amount of 680 μl of the heated solution was pipetted and dropped onto the fixture. This assures a good contact between the sample and the fixture [47]. To prevent evaporation of water from the sample, paraffin oil was poured around the perimeter of the sample, and the insulating chamber was closed. In the end, the samples were visually checked that there was no mixing of the sample with the paraffin oil.

The specimens were cooled down to 25 $°C$ at the rate of 0.5 K/min [18], during which viscoelastic properties were measured. During this temperature sweep, gelation was

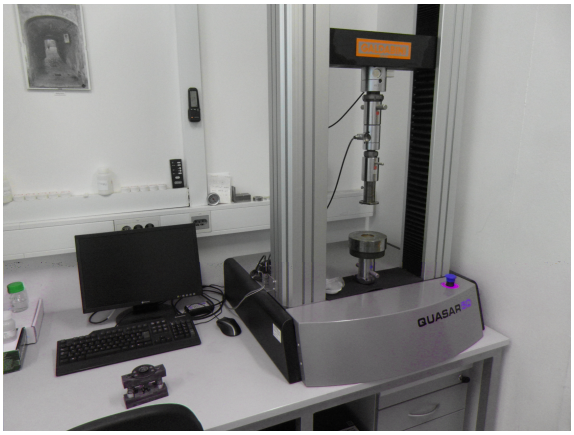


Figure 3.2: Benchtop testing machine Galdabini Quasar 50.



Figure 3.3: Rheometer Anton Paar MCR 301.

observed. The temperature of gelation was defined by the highest slope of the G'. Separate strain sweep tests were made, to determine the linear viscoelastic (VE) region of hydrogels. Based on these results, a common strain value was chosen and later used to record VE properties during cooling, and frequency sweeps. Each sample was used for a strain sweep test in a strain-controlled mode at the end to ensure that all the measurements were done in the linear region.

3.2.3 Dynamical mechanical analysis

Measurements were carried out using DMA242C (Netzsch Gerätebau, Germany). Samples with $5.9 \pm 0.1\ mm$ of diameter and $5 \pm 0.4\ mm$ of height were used since the maximum height was limited by the DMA sample holder. Sample's aspect ratio was kept the same as with uniaxial unconfined compression to ensure similar loading mode. To prevent evaporation of water from the sample's surface, all the samples were submerged in deionized water during measurements at 25 $°C$. Strain sweep tests were made to determine the linear viscoelastic

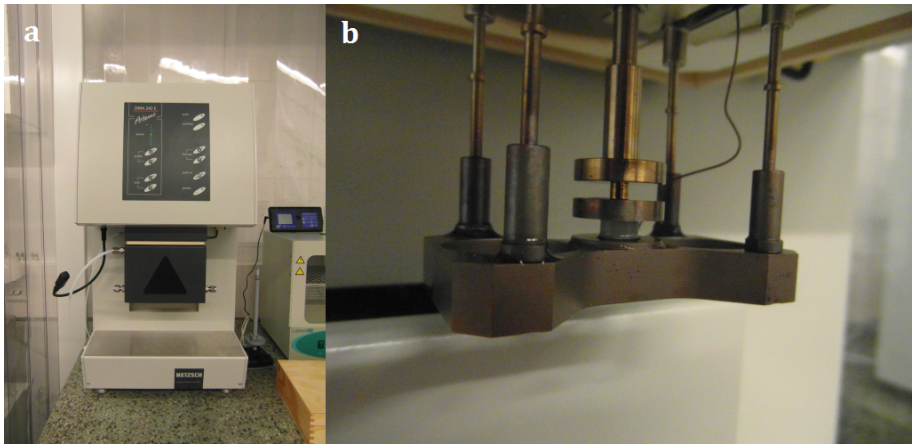


Figure 3.4: DMA machine Netzsch Gerätebau DMA242C (a) and a sample in the fixture (b).

region of deformation, by deforming from 1 μm to 20 μm amplitudes with steps of 1 μm at 1 Hz frequency, resulting in $0.6 - 0.7$ % maximum compressive deformation. Once the strain sweeps were accomplished, frequency sweep tests from 10 to 0.1 Hz were performed in the linear viscoelastic region. All strain and frequency sweeps have been performed with a proportional factor (PF) of 1.1, meaning that the 0.1 of the applied force amplitude was always kept at the sample to ensure contact between the sample and the upper compression plate. Also, creep measurements were done at various forces (from 0.1 to 1.2 N) on H2 samples. After finding suitable creep forces, we also used them to characterize other compositions of GG and BAG composite samples. All samples were pre-strained with 5 μm of deformation.

3.2.4 Indentation

Indentation measurements were performed on indentor CSM Nano Hardness Tester® (Switzerland) at Technische Universität Wien (Austria). We have used a diamond Berkovich tip. All the measurements were done in the same conditions. Loading was done at a rate of 30.0 mN/min and stopped at 15.0 mN. The tip was held at this force for 10 s to release any residual stresses, after which the unloading procedure followed at 30.0 mN/min.



Figure 3.5: Indentor CSM Nano Hardness Tester® (Switzerland).

3.2.5 Ultrasonic wave propagation

Our measuring system consisted of a pulser-receiver (5077PR, Olympus NDT, USA), an oscilloscope (WaveRunner 62Xi, Lecroy, USA), and several transducers. The pulser unit emits an electrical square-pulse of up to $400V$, with frequencies from 0.05 to 20 MHz. The piezoelectric element inside the ultrasonic transducer transforms the electrical signal into a mechanical signal when operating in sending mode. The receiving transducer works on the same principal, but transforms the mechanical signal to electrical. The specimen is placed between these transducers. To ensure transfer of the ultrasonic signal between the transducers and the specimens, a coupling media (honey) is used. Depending on the cut and orientation of the piezoelectric element in the transducer, a longitudinal or transversal wave is emitted. The receiving unit of the pulser-receiver has a bandwidth of 0.1 to 35 MHz, and a voltage gain of up to 59 dB. The amplified signal is displayed on the oscilloscope with a bandwidth of 600 MHz and a sample rate of 10 GS/s (10^*10^9 samples per second).

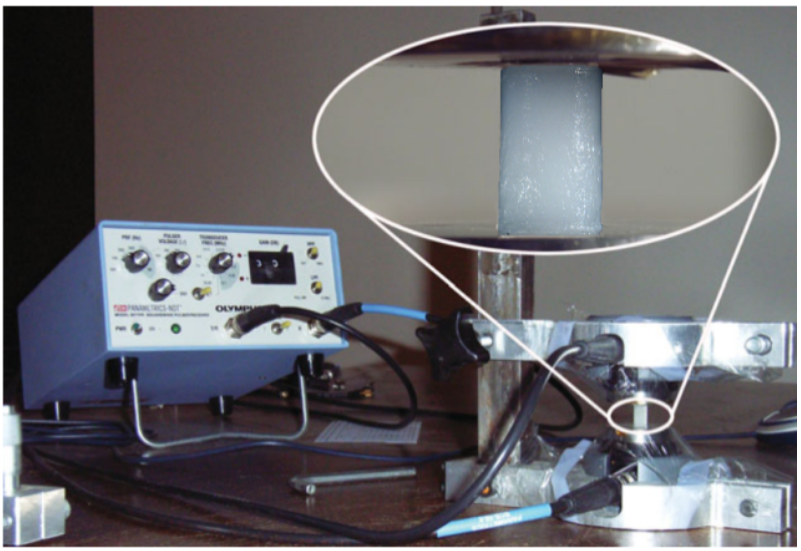


Figure 3.6: Setup for ultrasonic wave propagation measurements.

Tests were performed according to the established protocol [48]. By comparing a signal on the oscilloscope with and without the sample, time of ultrasonic wave propagation trough the sample can be determined (t_s). This time with the height of the sample (l_s) gives the speed of ultrasound propagation:

$$v_i = [l_s/t_s]_i \tag{3.1}$$

Where i stands for the type of excitation, either longitudinal (l) or transversal (t). Knowing speeds of both types of waves, we can compute material parameters using the following equations:

$$C_{1111} = \rho v_l^2 \tag{3.2}$$

$$C_{1212} = \rho v_t^2 \tag{3.3}$$

3.2.6 Density

Archimedes measuring technique was used to calculate the density of our samples. The technique is based on measuring the weight of the sample in the air and a fluid, water in

our case. Due to buoyant forces being different in air and water due to their density, this allows us to calculate the density of the sample from the following equation:

$$\rho_s = \frac{m_{air}(\rho_w - \rho_{air})}{K(m_{air} - m_w)} + \rho_{air} \tag{3.4}$$

Where m_{air} and m_w are measured masses of the sample in air and water, respectively. ρ_s, ρ_{air} and ρ_w stand for the density of the sample, air ($0.0012\ g/ml$) and water ($0.99756\ g/ml$), respectively, and $K = 0.99983$ is a correction factor that considers the sample holder that is submerged during measurement.

3.3 Degradation

Degradation was done for two types of scaffold material compositions. One composition with BAG and the other without BAG. The first had a composition H1 (2 *wt.* % GG with 2 *wt.* % BAG) and the other H0Ca1 (2 *wt.* % GG with 0.03 *wt.* % $CaCl_2$). Samples were 6 *mm* in diameter and $2-3$ *mm* in height. The samples were submerged in modified HBSS solution. Each sample was stored in a separate compartment in a 12 well multiwell plate at 36.5 $°C$ in 3 *ml* of SBF, which was around 50 times the volume of the sample. SBF was exchanged for a fresh one every other day.

Samples' degradation was evaluated using the most appropriate technique (Chapter 5.1.6), chosen based on the information we could extract from the samples, simplicity of use and reliability. Measurements of samples were taken at the following days: 0, 3, 7, 14, 21 and 28.

To verify the formation of hydroxyapatite (HA) samples were analyzed by FTIR and SEM after degradation.

3.3.1 FT-IR

To evaluate the formation of hydroxyapatite, FT-IR (Fourier Transform Infrared Spectroscopy) was used. For this, samples were freeze-dried in order to stop the formation or dissolution of hydroxyapatite. After DMA measurements had been done, the samples were put into a low-temperature freezer set at $-80\ °C$ for a minimum of 24 hours. Afterward, they were placed in a freeze-drier Lio-5 (Kambič, Slovenia) at 0.1 *mbar* and left for 72 hours, to ensure all the water sublimated. Measurements were done on a Spectrum 100 FT-IR (PerkinElmer, USA) equipped with an ATR (Attenuated Total Reflection) in the IR range $400 - 4000\ cm^{-1}$ and resolution of $2\ cm^{-1}$.

3.3.2 SEM

Formation of hydroxyapatite (HA) on the samples was also observed with SEM (Scanning Electron Microscope) on a FEG (field emission gun) SEM JSM 7600F (Jeol Inc., Japan). Samples were observed under accelerating voltage of 5.0 kV in order not to damage the sample during observation. For this, freeze-dried samples were also used and were prepared following the same procedure as for FT-IR. Dry samples were then cut to show either a cross-section or surface of the sample, placed onto a SEM holder and sputtered with carbon.

3.4 Additive Manufacturing

For 3D printing of hydrogels, an off-the-shelf 3D printer Replicator 2X (MakerBot, USA) was used (Figure 3.7). The printer is based on FFF technology (fused filament deposition).

It has a maximum print size of 25 *cm* x 16 *cm* x 15 *cm* (length/width/height). Default printing material is ABS and can print two materials at once. The printing volume is enclosed to provide an elevated temperature of the printed object, to avoid shrinkage of the ABS.

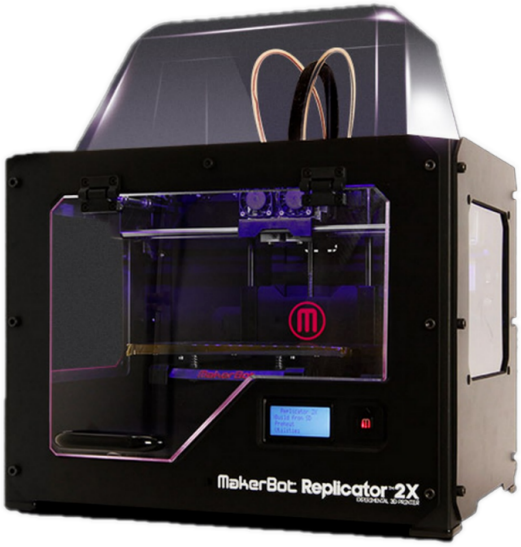


Figure 3.7: Default 3D printer MakerBot Replicator 2X.

3.4.1 Hardware modification

To extrude the hydrogel solution during printing, the default extruder head (Figure 3.8) was not appropriate. Unlike thermoplastic materials (ABS) that are stored as a filament and then melted quickly at the extruder head, GG hydrogel needs to be kept at an elevated temperature before printed. Therefore, we used a 20 *ml* glass syringe in which we filled the hot hydrogel solution. To keep the solution at an elevated temperature, a costume heating foil was used (Fly Heating Tech. Ltd., China). The foil is 45 *mm* wide and 65 *mm* long with an adhesive tape on one side so it could be wrapped around the syringe. The temperature of the syringe was monitored with the default thermocouple.

The holder for the syringe and the extrusion system had to be designed. The new holder was designed in SolidWorks modeling software in a way it could utilize the default stepper motor and could be attached on the original x-carriage.

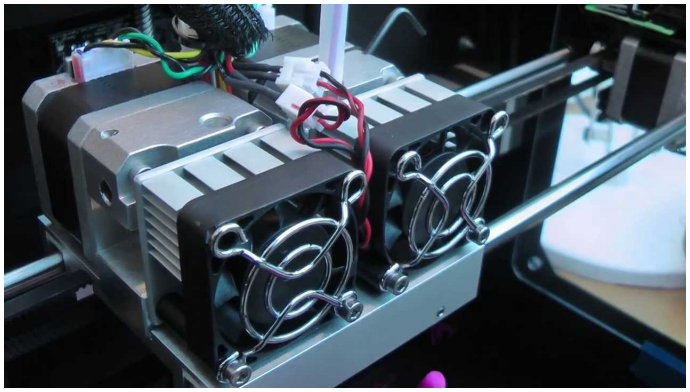


Figure 3.8: Default extruder head for printing thermoplastic polymers on a black plastic x-carriage.

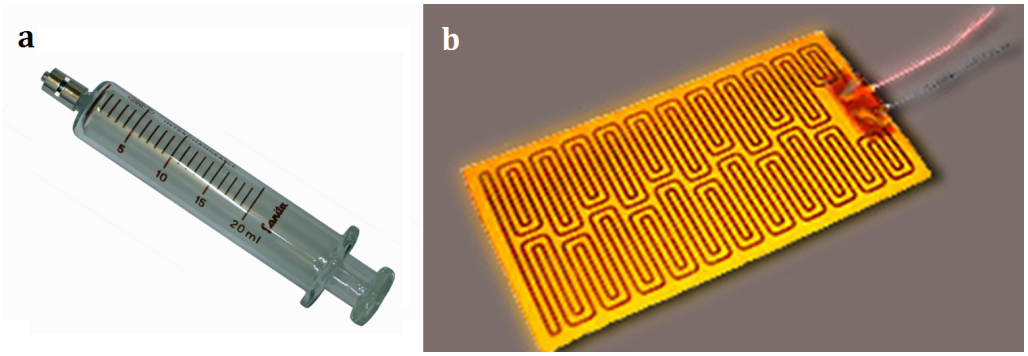


Figure 3.9: 20 ml glass syringe (a) and costume foil heater (b).

Chapter 4

Results

4.1 Characterization of Viscoelastic Properties of Gellan Gum BAG Composite

Samples for all the measuring techniques, except for rheometry, were made in advance. Samples in Figure 4.1 were used for the ultrasonic wave propagation technique. Sample H0 in Figure 4.1a has 2.0 *wt.* % of GG and no BAG particles and appears transparent. After the addition of 4.0 *wt.* % of BAG, the sample (H2) appears opaque, due to evenly distributed BAG particles during gelation of the samples.

Most techniques demand parallel top and bottom surface of the samples. Therefore, all samples were gelled in a Petri dish that was put on a levelled surface. At the same time, surface tension would lift up the hydrogel solution on the edge of the Petri dish during gelation. This could not be avoided, therefore the samples were punched from the middle part of the Petri dish where the top surface was flat, discarding the hydrogel that was affected by the surface tension. Glass Petri dishes with a diameter of 90 *mm* were used, resulting in around 13 samples with a diameter of 12 *mm*.

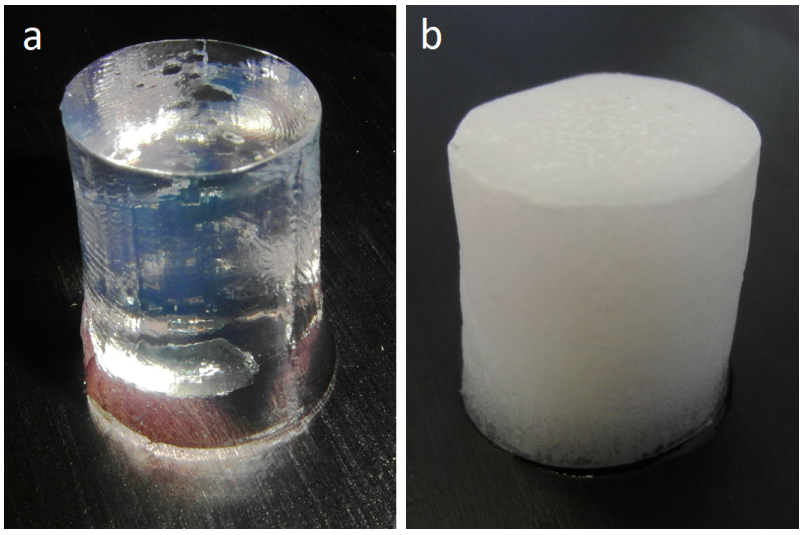


Figure 4.1: Prepared samples H0 (a) and H2 (b).

4.1.1 Uniaxial compression

Stress-strain curves (Figure 4.2) of pure GG hydrogel (H0) and a composite of GG hydrogel with BAG particles (H1) show high non-linearity. Purely elastic solid materials are expected to show linear slope at the beginning of the deformation, followed by yield stress, plastic deformation and failure. H1 composite shows a similar trend, as we can see the initial linear slope that bends at around $3 - 6$ % deformation into a lower angle slope. This latter part of deformation ($6 - 25$ %) does show some spikes pointing downwards, which might indicate a gradual failure of the polymer network. However, there is no clear indication of the initial point of failure of the sample. When the sample is unloaded, the stress drops down to zero with a similar rate as the initial slope of deformation. This shows the release of the stored elastic energy. Looking at the difference of deformation at the start and the end of the experiment, we can see how much of the polymer network was permanently deformed i.e. broken.

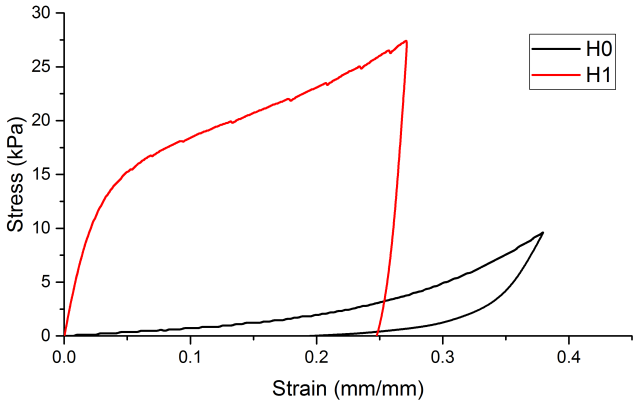


Figure 4.2: Stress-strain diagram of GG (H0) and GG-BAG composite (H1).

The H0 sample deformed in a different manner, having a more nonlinear deformation throughout the whole measurement. Despite larger deformation (up to 38 %) we can see less 'permanent deformation', meaning that the polymer network is less damaged as the H1 sample.

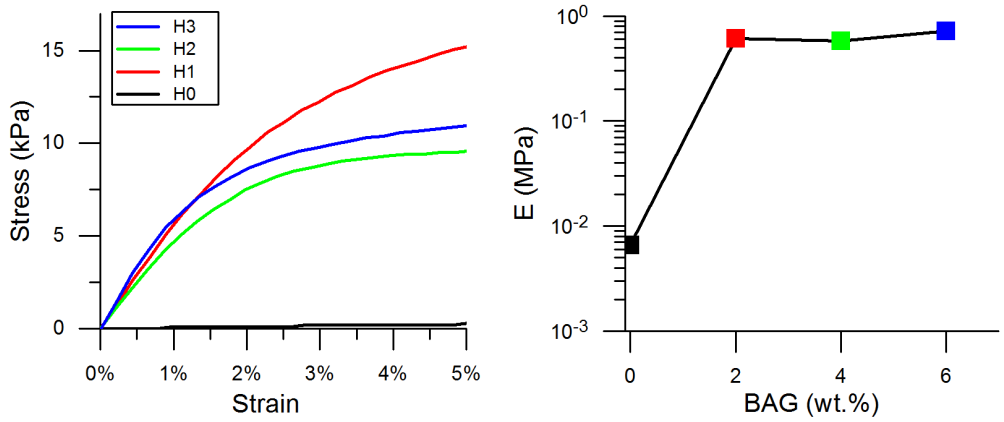


Figure 4.3: Stress-strain diagram at small deformations (a) and elastic moduli (b) of the pure GG and composite samples.

Elastic moduli (E) in compression measurements were obtained from the initial slope of the stress-strain curves (Figure 4.3a), which is the same as in Figure 4.2 except for a smaller scale. Measurement of pure H0 showed $E = 6.6 \pm 0.8\, kPa$ (Figure 4.3 b). With the addition of BAG particles, Youngs's modulus increased to $500 - 800\ kPa$. By further increasing the amount of BAG, there is no prominent trend of reinforcement.

4.1.2 Shear rheology

Temperature sweep measurements (Figure 4.6) allowed not only measurements of gelled hydrogels, but also determination of the temperature of gelation. Looking at the shear storage modulus (G'), we can see the increase with the increasing amount of BAG (Figure 4.4). The increase in shear loss modulus (G'') is not so evident, since the values are approximately ten times smaller. The obvious difference is also in the increasing temperature of gelation that shows a clear linear trend in the chosen range of BAG particles.

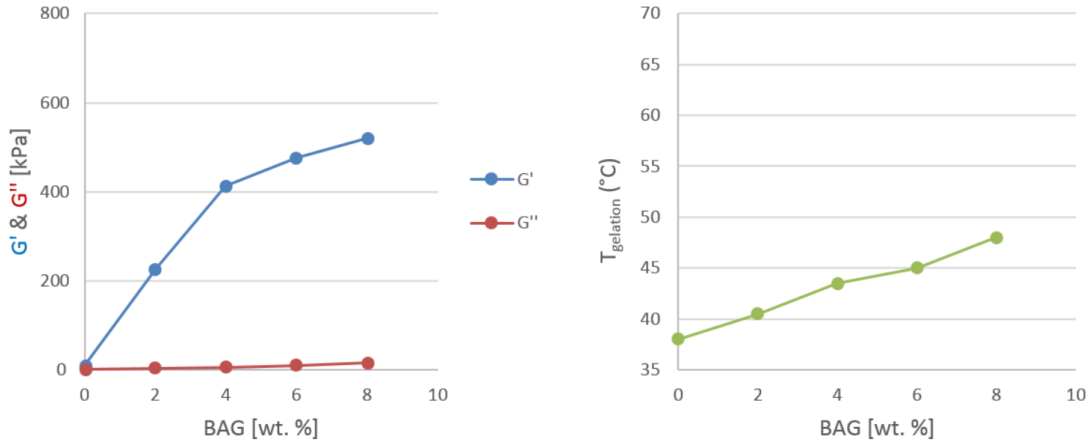


Figure 4.4: Viscoelastic moduli (left) and temperature of gelation (right) of solid i.e. gelled hydrogel samples with different amounts of BAG (without added $CaCl_2$).

We have also done measurements of different amounts of dissolved $CaCl_2$ in the 2 $wt.$ % GG hydrogel (Figure 4.5), without added BAG particles. Ca^{2+} ions act as crosslinkers of GG and are also present in BAG. Increase in elastic modulus and temperature of gellation is again observed. At 0.12 $wt.$ % of $CaCl^2$ the shear elastic modulus (G') reaches maximum. With a further increase of $CaCl_2$, the modulus starts to decrease, whereas the temperature of gelation keeps on rising.

Unlike uniaxial compression, rheometry allows measurements of hydrogels from the liquid to the solid state. By measuring viscoelastic properties during the temperature sweep starting with liquid samples, we can observe the gelation process in more detail.

Figure 4.6 shows results of the temperature sweeps of different compositions that clearly show a difference between the compositions. The difference starts already at the beginning when the sample is still in the liquid form. With decreasing temperature, we can observe the difference in the starting temperature of gelation while the end of gelation stays at almost the same temperature for all the compositions. At room temperature, the difference in moduli is the most prominent.

As the sample is in the liquid form at the beginning of the measurement, it shows the lowest moduli. It is quite clear that the measurements at this point show some deviation with time, which is a consequence of a poor signal. This could be avoided with a larger diameter of the measuring cone or with a larger amplitude of deformation. However,

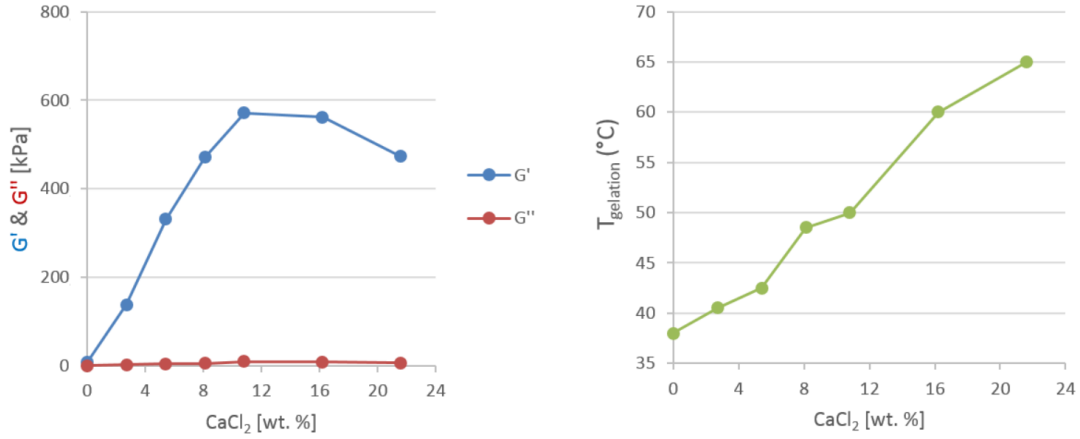


Figure 4.5: Viscoelastic moduli (left) and temperature of gelation (right) of solid i.e. gelled hydrogel samples with different amounts of $CaCl_2$ (without added BAG).

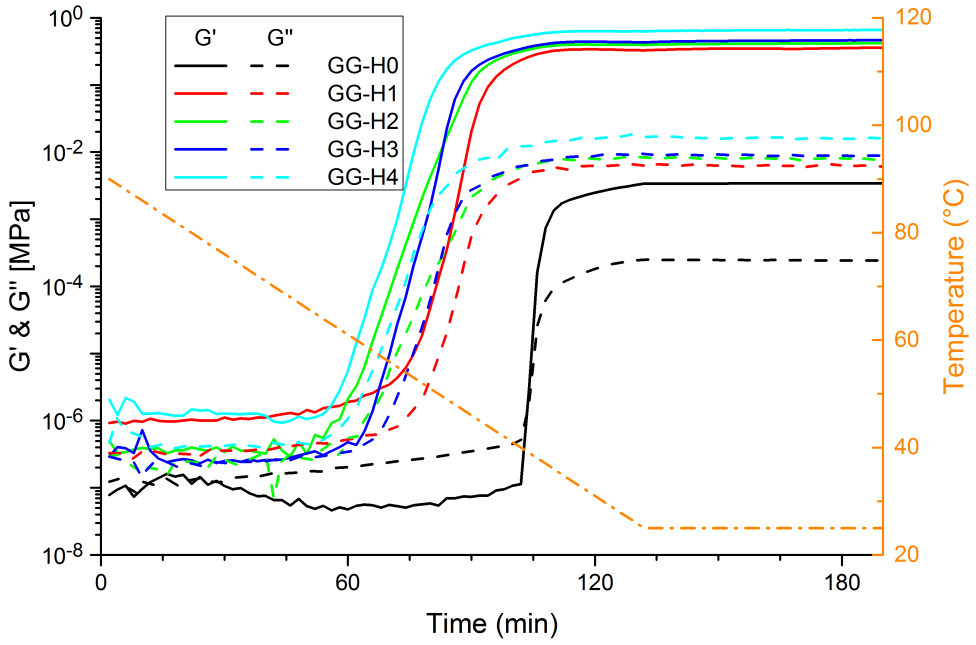


Figure 4.6: Viscoelastic measurements of hydrogels with a varying amount of BAG during the temperature sweep.

this would lead to non-linear deformation of the sample in the solid form. Therefore, a compromise had to be taken in order the measure the sample in the whole temperature range with the same measuring parameters.

Dissipative moduli (G″) of the samples in the liquid form increase with the addition of BAG, but show almost no increase with further addition of BAG. On the other hand, elastic moduli (G′) do not show any particular trend. This could be a consequence of the sample preparation. As the sample is poured on the bottom fixture, the water starts to evaporate from the surface of the sample immediately, especially due to the temperature of 90 $°C$.

This increases the polymer content locally on the surface of the sample. During lowering of the upper fixture, the sample is slightly mixed decreasing the non-homogeneous polymer concentration. When the upper fixture stops at the final height, the sample is checked and its surface is covered with paraffin oil. In this time evaporation continues, meaning that on the outer perimeter of the sample (at the contact with paraffin oil), the sample could be dry or at least the polymer concentration can be higher. Since the rheometer is intrinsically the most sensitive to the outer diameter of the sample, any elasticity in this region can show on the results.

Gelation region, where both G′ and G″ considerably increase, shows some obvious differences. The starting temperature of gelation as well as the temperature 'window' of gelation change with the addition of BAG particles. Pure GG has a very sudden gelation point starting at 40 $°C$ and finishing at 36 $°C$. With the addition of BAG (sample H1), the starting temperature of gelation raises to 57 $°C$ finishing at 40 $°C$. Further increase of BAG particles increases the starting and finishing temperature of gelation but not as prominently.

After gelation, at 25 $°C$ the sample was kept at this temperature for another hour. This was to ensure that the gelation finished, however it can be seen that there is little change in rheological properties after the temperature has stopped decreasing. This implies that cooling was done slow enough to ensure temperature equilibration and gelation is mainly temperature driven. Significant difference can also be observed in the final moduli. Addition of BAG shows reinforcement of samples, but again the reinforcement effect seems to diminish with a further increase of BAG particles. On the other hand, the difference between G″ and G′ seems to be similar in all the cases. This will be better seen on the measurements of frequency sweeps (Figure 4.7).

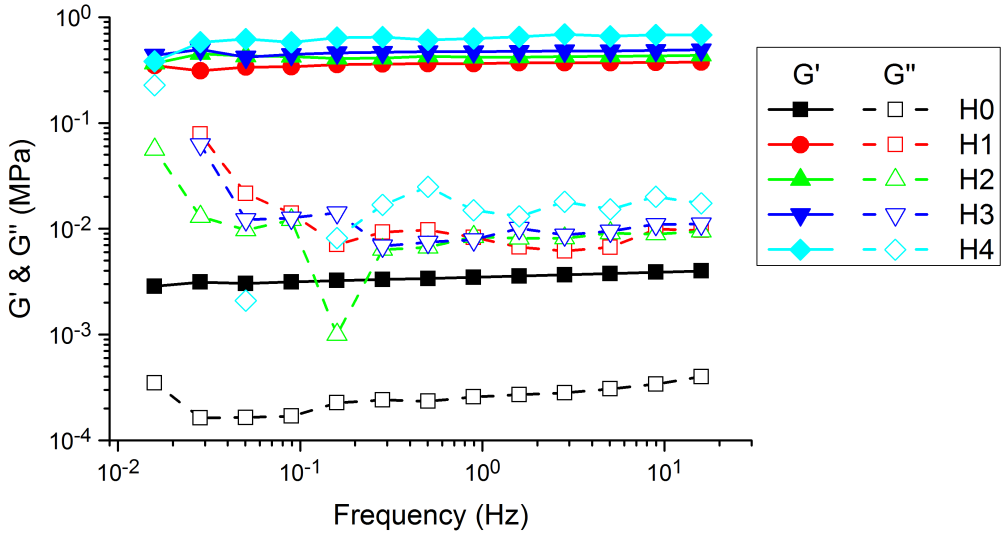


Figure 4.7: Frequency sweeps of GG samples (rheometry) with different amounts of BAG.

At the end of the temperature sweep experiment, each sample was measured in the frequency and strain sweep. Frequency sweep results (Figure 4.7) show very little frequency dependence and G′ above G″ for all compositions. However, it is worth noticing that pure GG along with lower moduli than other composites also exhibit less separation between G′ and G″, i.e. higher dissipation factor $\tan(\delta)$ (Figure 4.8).

Strain sweep also shows an obvious change of the linear deformation region i.e. where

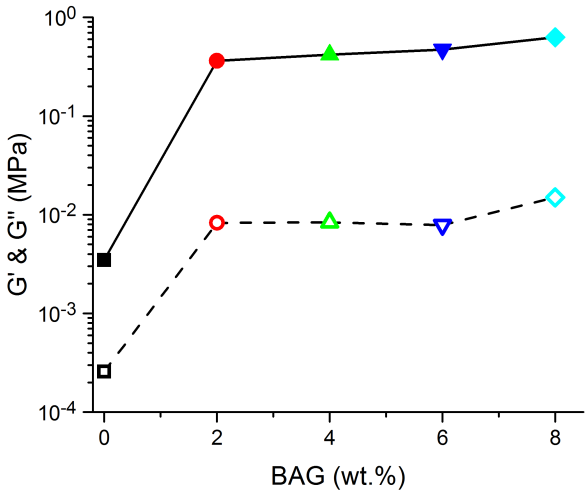


Figure 4.8: Shear moduli (G′ and G″) of GG samples (rheometry) with different amounts of BAG at 1 Hz.

both G′ and G″ are constant. Linear deformation region of H0 extends up to 20 % of deformation, whereas upon addition of BAG it decreases to 0.3 % (looking at the linearity of G″). Results of samples with added BAG also showed high instability above 1 % deformation, therefore the results were cropped from this point on. On the other hand, H0 showed stable measurements even in the nonlinear deformation region.

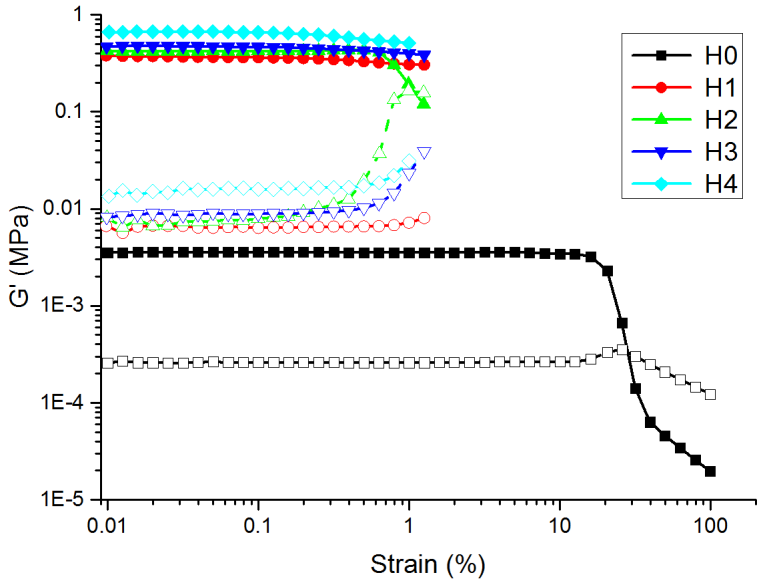


Figure 4.9: Strain sweep of GG samples (rheometry) with different amounts of BAG.

4.1.3 Dynamic Mechanical Analysis

Strain sweep was done to determine the linear deformation region. Maximum deformation of 20 μm was applied on the samples, which resulted in 0.65 to 0.75 %, depending on

the height of the samples. Sample H1 shows linear deformation i.e. constant slope on stress-strain diagram, in the measured region. However, samples H2, H3 and H4 show some nonlinearity above 0.5 %, where the slope increases.

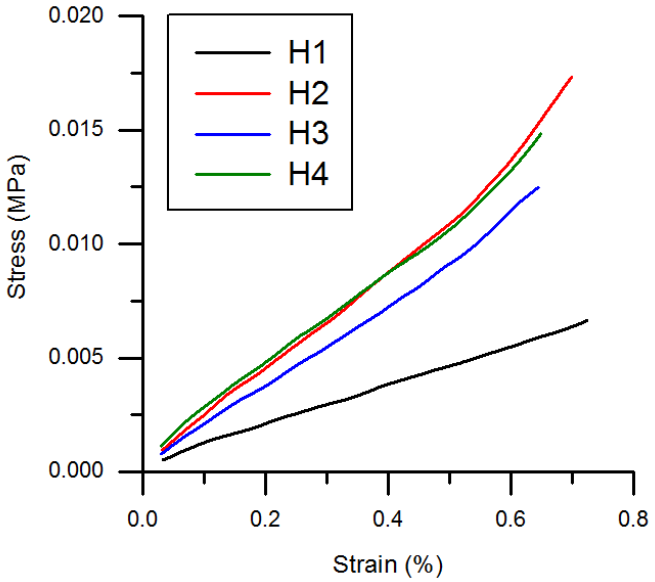


Figure 4.10: Strain sweep measurements of GG and BAG composite samples in DMA at 1 Hz.

Results of DMA frequency sweep (Figure 4.11a) are similar to the results of the frequency sweep of rheometry (Figure 4.7). Uniaxial storage modulus (E') is constant for all the samples in the measured frequency sweep. However, uniaxial loss modulus (E'') shows more frequency dependence, especially for samples H0 and H4. Similar to the rheometry measurements, storage modulus is about one decade higher than the loss modulus, only for H0 and H4 at higher frequencies where dissipation in the samples increased, i.e. higher ratio between E'' and E'. Figure 4.11b shows a drastic increase in moduli from H0 to H1 sample, however samples do not show steady reinforcement with further increase of the amount of BAG.

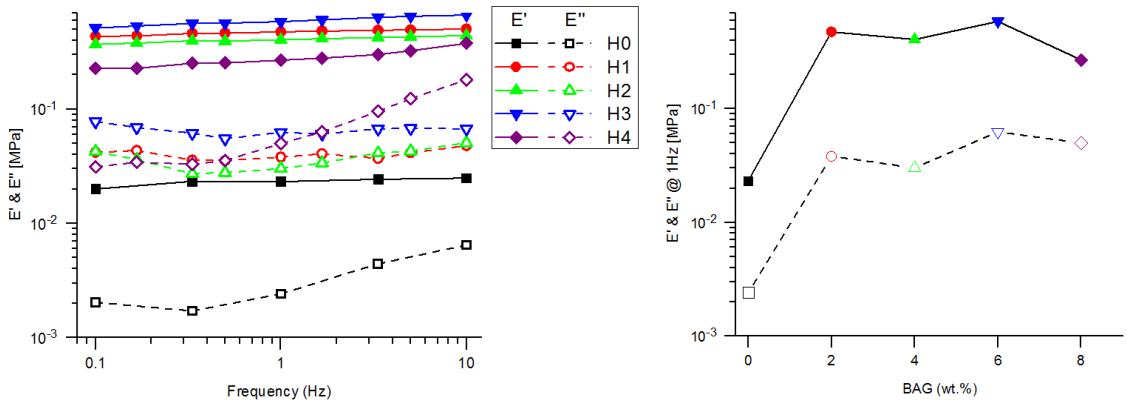


Figure 4.11: Frequency sweeps of hydrogels (DMA) with a varying amount of BAG (a) and moduli (E' and E'') at $1Hz$ (b).

Creep experiments show how samples deform under constant load over time. Compared to the frequency sweep where the samples used were 6 mm in diameter, in creep we used samples with 12 mm in diameter, which allowed for higher precision of creep force control. We have started by measuring H2 samples at various forces ranging from 0.1 N to 1.2 N. Upon further analysis we have determined 0.2 and 0.4 N of creep force to be the most suitable to be used for other samples (H1, H3 and H4) and still be a reversible region of deformation, because higher forces resulted in failure of the H2 sample. Sample H0 was too weak to be measured at comparable forces, since it failed even at 0.1 N creep force.

	0.1 N	0.2 N	0.4 N	0.8 N	1.2 N
H0	H0_Creep_0,1N_ 25C_12mm				
H1		H1_Creep_0,2N_ 25C_12mm	H1_Creep_0,4N_ 25C_12mm		
H2	H2_Creep_0,1N_ 25C_12mm	H2_Creep_0,2N_ 25C_12mm	H2_Creep_0,4N_ 25C_12mm_2	H2_Creep_0,8N_ 25C_12mm	H2_Creep_1,2N_ 25C_12mm
H3		H3_Creep_0,2N_ 25C_12mm	H3_Creep_0,4N_ 25C_12mm		
H4		H4_Creep_0,2N_ 25C_12mm	H4_Creep_0,4N_ 25C_12mm		

Table 4.1: List of samples measured in creep where some failed (red) and some withstood the creep forces (green).

Figure 4.12 shows results of creep measurements of H2. In the first 2 min, deformation is non-linear, after which it tends to reach steady state. Samples exposed to creep force 0.4 N and lower reach deformation plateau after this initial nonlinear deformation. From 2 until 10 min in experiment, deformation does not change for these samples. Sample at a creep force of 0.8N already shows some additional creep between 2 and 10 min, while at 1.2 N the sample clearly creeps.

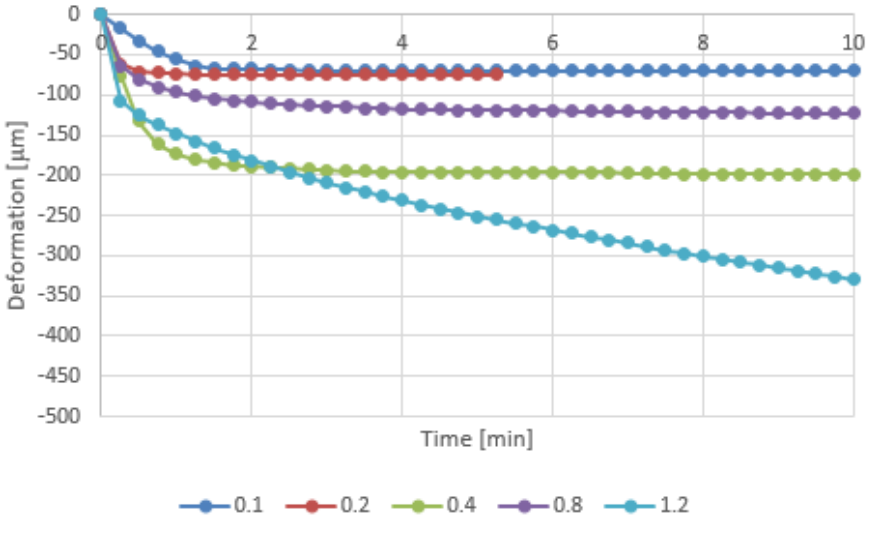


Figure 4.12: Creep experiments at different creeping forces of the H2 sample.

To further explain the initial non-linear creep of the experiment, it is worth noting the actual creep force that is exerted on the samples. In an ideal case, DMA would instantaneously exert the necessary creep force on the sample, from 0 to the chosen value. However, due to inherent properties of the measuring system, DMA needs some time to

reach the necessary creep force. The actual force is therefore measured separately (Figure 4.13). We can see that with H2 samples, DMA needs around 1 *min* to stabilize to the desired creep force, however at 0.1 *N* creep force, the time to stabilize increases to almost 2 *min*.

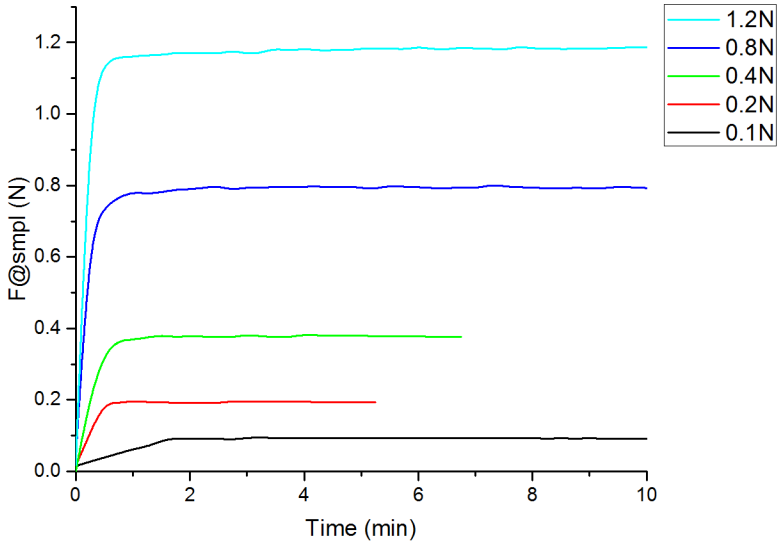


Figure 4.13: Force at the sample during creep measurement for H2 samples.

Creep experiments were then performed at two different creep forces (0.2 and 0.4 *N*) for all the GG and BAG composites (without H0). We could see that in average, creep deformation of the samples at 0.4 *N* is higher, which was expected. All the samples reached steady state deformation after approximately 2 *min*. However, the steady state deformation of the samples does not show any specific trend according to the amount of BAG in the samples. At a creep force of 0.2 *N* the stiffest material, i.e. the one that deforms the least, is H2 and on the other side the sample that deforms the most is H3. At a creep force of 0.4 *N* the stiffest material is H1 and the softest H3. If we exclude the sample H2 (since the sample could have been corrupted), we can see the samples follow the same trend at both 0.2 and 0.4 *N* creep force ranging from the stiffest to, softest in order: H1, H4 and H3.

4.1.4 Indentation

In the following figure (Figure 4.15), we see the profile of the indenter load, and the corresponding displacement along the time of measurement. Deformation increases the most at the beginning, due to the small initial contact area. When the force stops increasing and is held constant, deformation decreases significantly, but we can still observe some deformation. This corresponds to a time-dependent plastic deformation. Indentation measurements are often shown in a load-displacement diagram (Figure 4.15b) instead of stress-strain, since load-to-stress and displacement-to-strain relations are non-linear. The diagram shows how the loading curve does not match the unloading one, meaning that a part of the deformation is irreversible. This is a result of high shear and compression stresses around the indenter tip where plastic deformation occurs. As marked in Figure 1.9, elastic modulus was obtained from the start of the unloading curve.

Sintered bioactive glass sample was measured 23 times (Figure 4.16) at different locations (one of the measurements is in Figure 4.15). Mean measured elastic modulus was

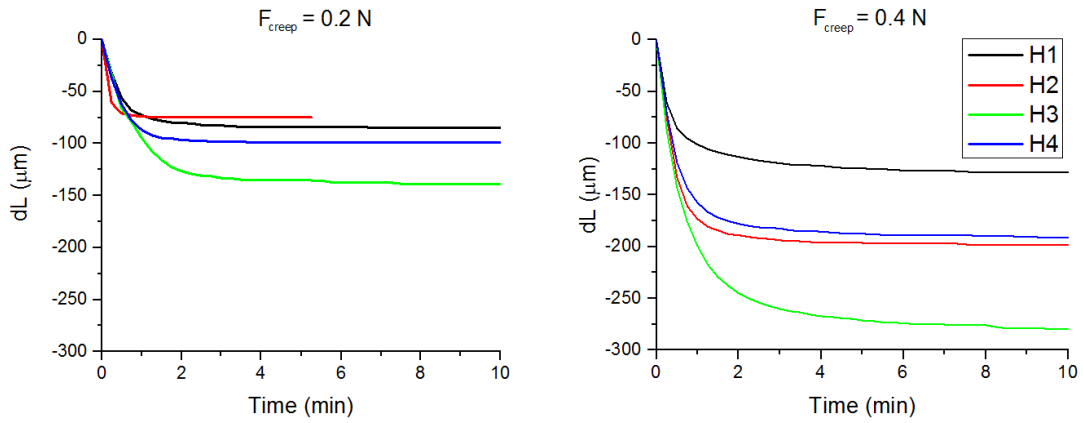


Figure 4.14: Creep experiments of GG and BAG composite samples at 0.2 (a) and 0.4 N (b) creep force.

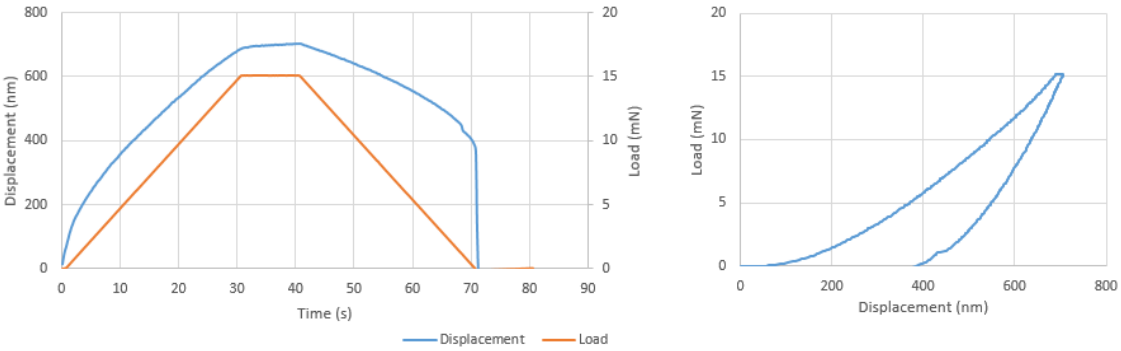


Figure 4.15: Load controlled indentation of sintered BAG sample with respect to time (a) and load-displacement diagram of the same indentation (b).

$E = 26.7 \pm 8.4\ GPa$, and was calculated using the following equations:

$$E = \frac{1}{23}\sum_{i=1}^{23} E_i \tag{4.1}$$

$$s = \sqrt{\frac{1}{23}\sum_{i=1}^{23}(E_i - E)^2} \tag{4.2}$$

Where E is mean elastic modulus and s is standard deviation of mean elastic modulus. Despite mechanical properties of GG and BAG composite samples being the focus of this work, it is crucial to know the mechanical properties of individual components to determine the contribution of each component.

Measurements of composite samples (H0, H1, H2, H3 and H4) were not possible. We have tried the strain-controlled mode and increased the indentation depth to 200 μm. For comparison, around 0.7 μm indentation was reached with sintered BAG samples. Despite this, the measured force of composite samples was so low, that it was in the range of sensor resolution ($\approx 0.01\ \mu N$) and did not show any observable trend.

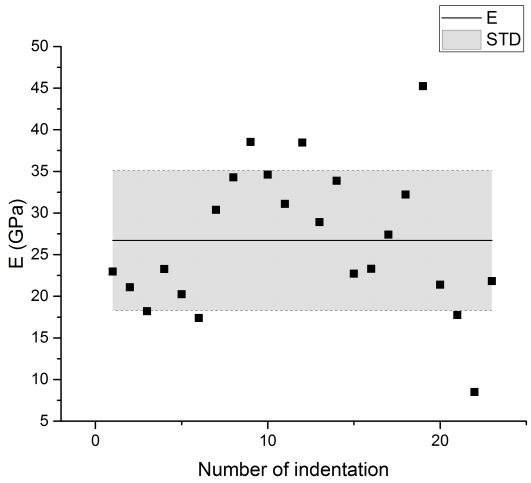


Figure 4.16: Indentation measurements plotted in the order they were measured with the mean elastic modulus with standard deviation region in grey area.

4.1.5 Ultrasonic wave propagation

To determine the mechanical stiffness of the samples with ultrasonic wave propagation, we first had to measure the samples' densities. Archimedes technique has turned out to be appropriate. Density of pure hydrogel was just above 1 g/cm^3 (density of water), while by adding BAG particles the density of the samples increased linearly. This is expected, since the density of BAG particles was measured to be 1.73 ± 0.02 g/cm^3.

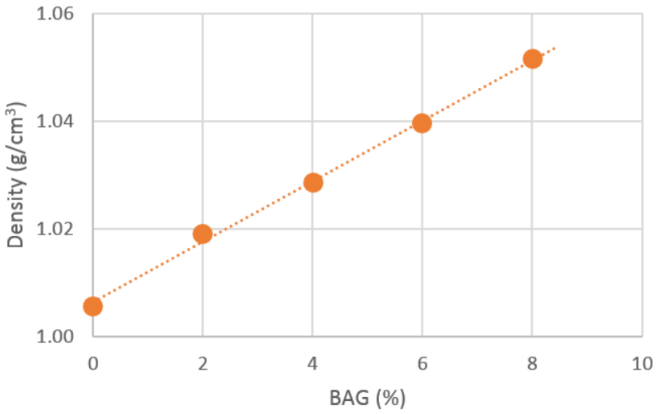


Figure 4.17: Density measurements of hydrogel samples with different amounts of BAG.

We measured the time of propagation of ultrasonic waves (longitudinal and transversal, with appropriate transducer for each type) and calculated elastic moduli (Figure 4.18) using Equation 3.2 and Equation 3.3. Speed of longitudinal ultrasonic waves for all the compositions was 1.51 ± 0.04 km/s, while the speed of transversal waves was 0.52 ± 0.03 km/s. There is no significant difference between different compositions and no particular trend of reinforcement, as seen with other techniques.

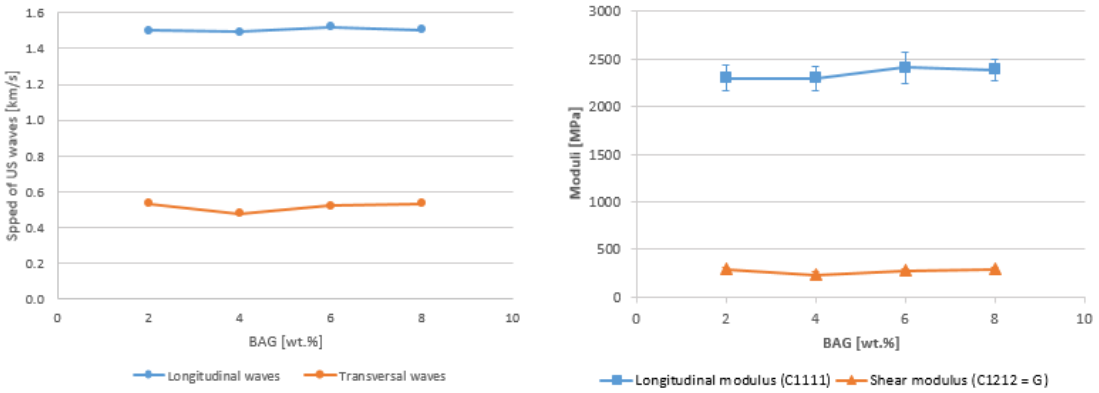


Figure 4.18: Speed of longitudinal and transversal ultrasonic waves in hydrogels (a) and corresponding elements of the stiffness matrix (b).

4.2 Viscoelastic Properties During Degradation

During degradation of the samples H0Ca1 and H1, viscoelastic properties were measured using DMA. This technique was chosen as the most suitable technique (Chapter 5.1.6). For each day of measurement (0, 3, 7, 14, 21 and 28) and sample composition, 6 samples were made making a total of 72 samples. All the samples were first put into SBF in 12 well multiwell plates in a mixer and taken out at 3 hours before measuring them. Samples on the day 0 were put into SBF for 3 hours in order that they swell up in SBF and reach equilibrium state.

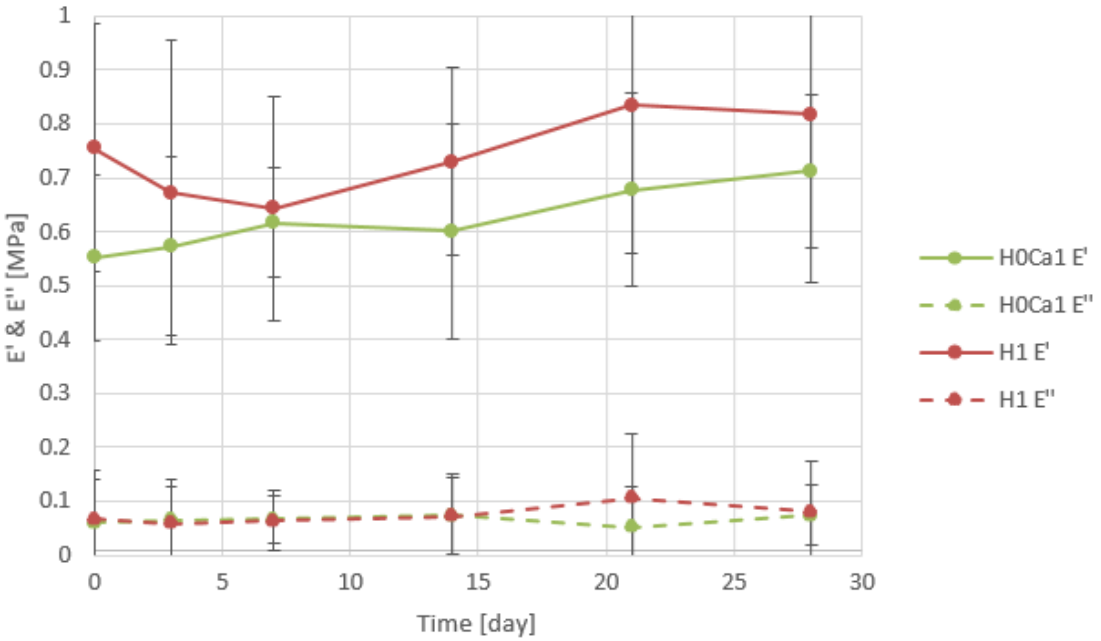


Figure 4.19: Viscoelastic moduli (E′ and E″) of hydrogel samples during the degradation experiment.

Elastic modulus (E') at the beginning, up to day 7, showed different trends (Figure

4.19). Samples H0Ca1 showed an increase of elastic modulus that continued throughout the whole experiment. On the other hand, H1 showed a decreasing elastic modulus up to day 7, after which the modulus started increasing. The trend of reinforcement of both (H0Ca1 and H1) compositions was similar after 14 day of incubation. Dissipative modulus of both compositions followed a similar trend.

4.2.1 Fourier Transform Infrared Spectroscopy (FT-IR)

The formation of hydroxyapatite (HA) was studied by FT-IR on freeze-dried samples. Figure 4.20 shows FT-IR spectra of H0Ca1 and H1 at 0 and 28 days of immersion in SBF. The bands at 1095 cm^{-1} and 1033 cm^{-1} correlate to the *P-O* stretching vibration modes of HA [23], [49]. The band at 872 cm^{-1} corresponds to CO_3^{2-} incorporation of carbonate into the apatite, resulting in nonstoichiometric hydroxycarbonated apatite [50]. The bands at 601 cm^{-1} and 562 cm^{-1} represent the bending mode of the *O-P-O* [49] and *P-O* bending mode [23] of HA, respectively. Splitting of 556 cm^{-1} and 601 cm^{-1} bend is an evidence for crystalline hydroxyapatite [23], [51], [52]. The bands at 1410 cm^{-1} correspond to symmetrical stretching of *COO-* group [44], and are more pronounced for the H1 samples. Much more intense is the peak at 1025 cm^{-1} which represents the stretching of the *C-O* bonds in the GG polysaccharide ring [44], but is overlapping the band of *P-O* stretching modes at 1033 cm^{-1}.

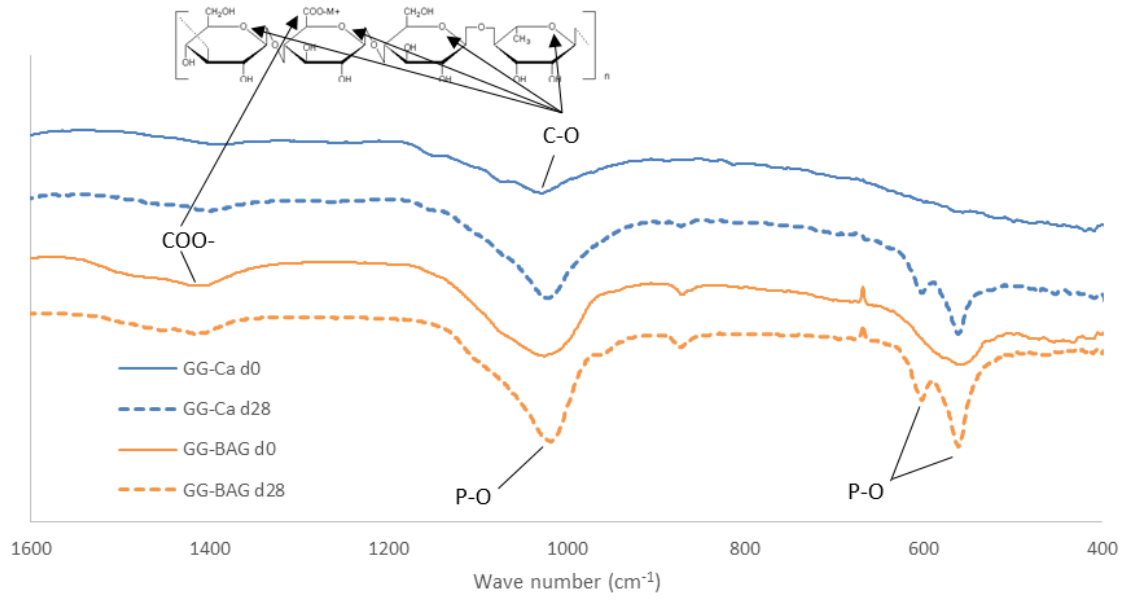


Figure 4.20: FTIR spectrum of hydrogel samples for degradation before the experiment (d0) and after 28 days of incubation (d28).

4.2.2 SEM

Freeze-dried samples were also studied with SEM to see possible changes in structure. Figure 4.21 shows the structure of both compositions after the freeze drying process. Samples show porosity in the center, however the outer surfaces are mostly closed. Porosity also varies between the samples. Sample H0Ca1 showed smaller pores around 200 μm in diameter with homogenous distribution, whereas the H1 sample showed larger pores with cross-sections up to 500 μm, larger distribution of pore size and more elongated pores.

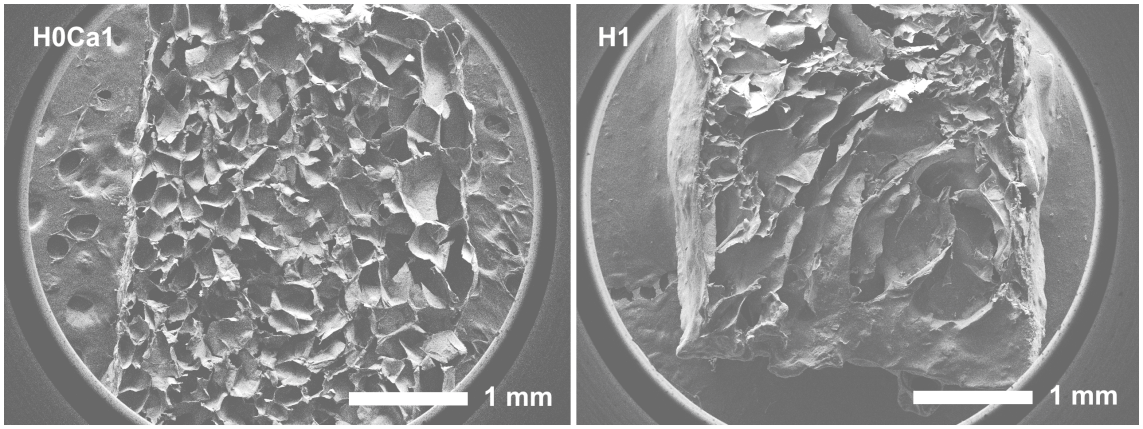


Figure 4.21: Porosity of H0Ca1 (left) and H1 (right) samples after freeze-drying.

Surfaces of all samples seemed to be covered in particles (Figure 4.22). Sample H0Ca1 still has a visible surface of the polymer on day 0, whereas H1 composition is already fully covered. After 28 days both sample surfaces are completely covered with particles.

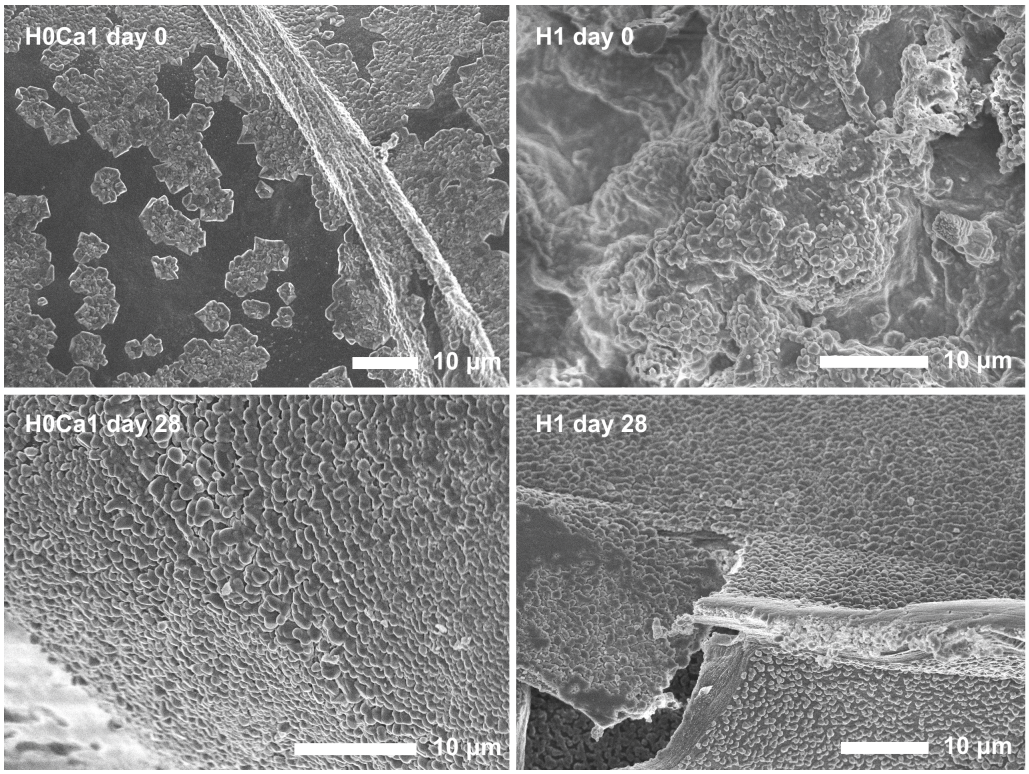


Figure 4.22: Figures at the top show micrographs of the samples at day 0 (submerged in SBF for 3 hours) and the bottom figures show micrographs of the samples after 28 days in SBF.

At higher magnification (Figure 4.23), particles on both samples at day 0 look similar and are approximately 500 nm in diameter. Since polymer matrix is covered on the H1 sample, we cannot see BAG particles. Samples that were kept in SBF showed aggregates of smaller particles, with a diameter bellow 100 nm. H0Ca1 sample contains more of these

aggregates, however this varies significantly on the place on the sample where the photo was taken.

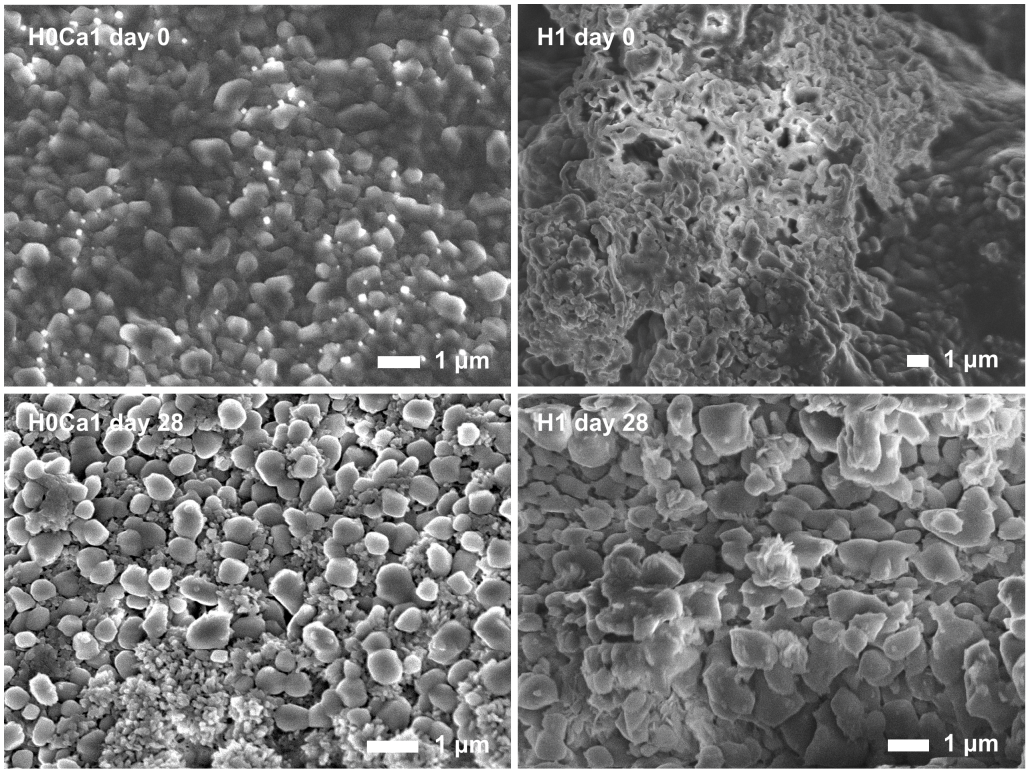


Figure 4.23: Figures at the top show micrographs of the samples at day 0 (submerged in SBF for 3 hours) and the bottom figures show micrographs of the samples after 28 days in SBF.

4.3 Additive Manufacturing

The main frame of the 3D printer was kept intact, however several modifications had to be made. The upper acrylic cover was removed due to a larger size of the syringe extruder. The front acrylic doors were also removed for easier handling of the samples.

4.3.1 Design of a syringe extruder

The new extruder (Figure 4.24) of the 3D printer had to be able to print hydrogel polymers. After the hydrogel solution is made, it needs to be kept at an elevated temperature. For this, a heated syringe was used. This syringe is then moved by the 3D printer's software and at the same time, the syringe is pressed to extrude the material. When the hydrogel solution is extruded out of the nozzle onto the printing surface, the solution cools down due to the lower temperature of air and printing surface. This causes the hydrogel solution to solidify, giving the possibility to print layer on layer to form a 3D model.

The new extruder is built around a syringe that is positioned in a way that the nozzle is in the same position where the nozzle of the original extruder was. Therefore, the syringe is positioned vertically, as well as other components (guide rods, threaded rod, etc.). This also ensures that the new extruder is not much wider than the old one, giving the possibility to use most of the printing area.

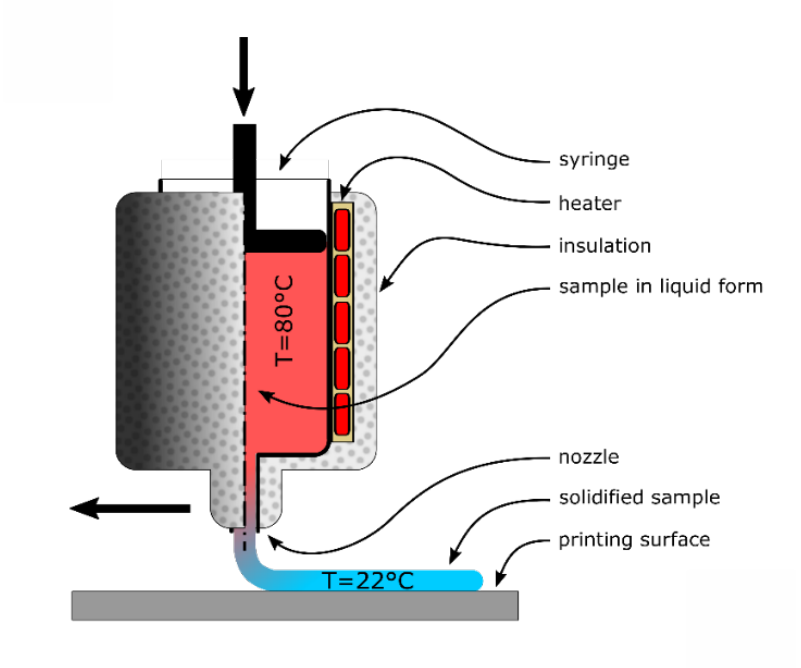


Figure 4.24: Schematic design of the new modified extruder head and the temperature of the material during extrusion.

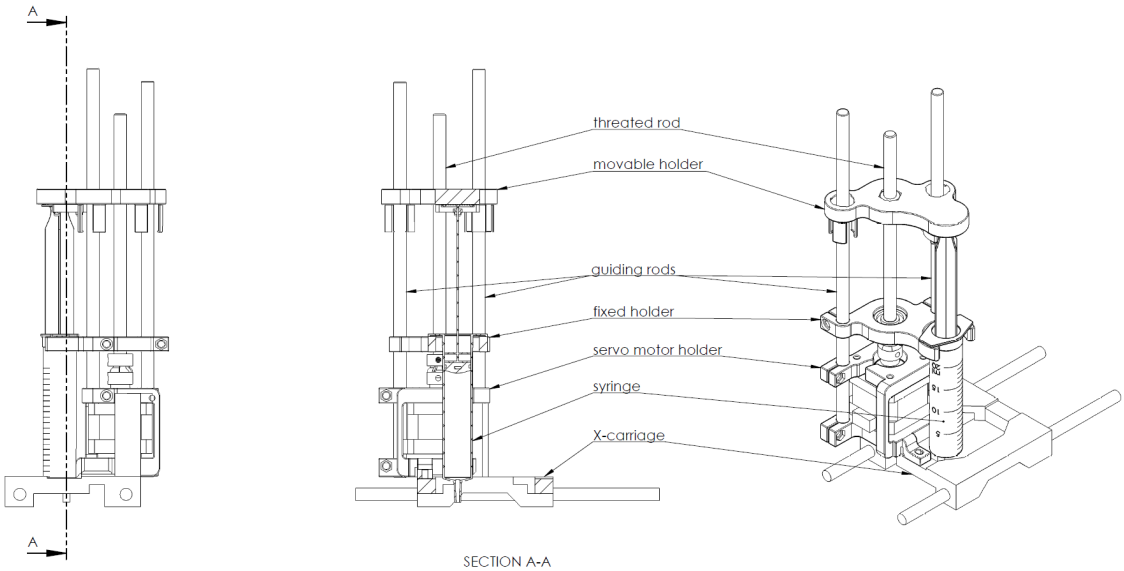


Figure 4.25: Drawing of the new extruder head with a syringe without the nozzle in side view (on the left), cross-section (in the middle) and isometric view (on the right).

Besides positioning the syringe, reliable extrusion is also important. Original stepper motor was used in vertical position, on which a threaded rod was attached using a flex coupler. The threated rod is 5 mm in diameter with a 0.8 mm pitch and it moves the movable holder up and down in order to squeeze the material out of the syringe. In order for the movable holder to stay leveled, it is held by two 8 mm guiding rods and two ball

bushings (25 mm long). This ensures that the syringe is compressed evenly through-out the whole travel.

The height of the syringe nozzle can be adjusted. The nozzle of the syringe can be changed, giving opportunity to test different diameters and lengths of a nozzle. To simplify changes of the nozzle, the whole syringe can be moved up and down. The syringe sits on the fixed holder. By moving the fixed holder up or down the guiding rods, and tightening it with screws, we can adjust the height of the end of the nozzle.



Figure 4.26: 3D rendering of the modified extruder head.

All the parts were printed with the same MakerBot Replicator 2X. Parts were made from ABS, at a vertical resolution of 0.2 mm. To ensure sufficient stiffness of the parts, they were printed with three shells, and 20 % diamond infill. Despite the effort of minimizing the size of the new extruder, we had to limit the movements of the extruder in x-axis in the software, and y-axis in software as well as make a physical adapter to offset the homing position.

4.3.2 Software for controlling the 3D printer

All the 3D models were done in SolidWorks or Meshmixer and exported in STL files. This is a file format initially made for stereolithography CAD (computer-aided design) software created by 3D Systems (USA). STL file describes surface geometries of a three-dimensional object without information of its color, texture, etc. Some models of bones (Figure bellow left) were obtained from real CT scans, and then processed in a software 3DSlicer 4.5.0. This software takes images from CT scans, builds a 3D model and exports it in a STL file. Such a model usually needs post-processing in Meshmixer.

Software Simplify3D and MakeBot Desktop 3.10 were used for slicing and printing. Both programs are also known as 'slicers'. A slicer is a software that takes an STL file and

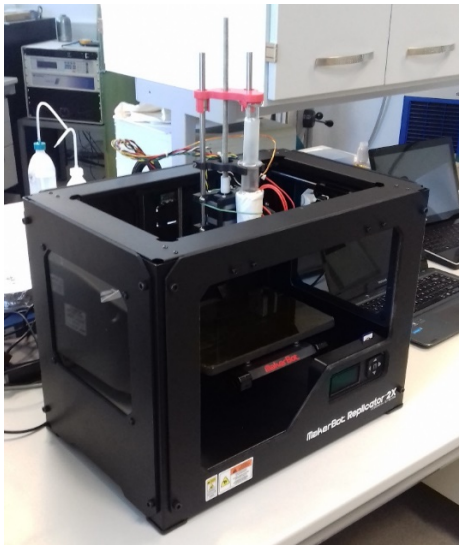


Figure 4.27: New extruder on the original x-carriage of the 3D printer.

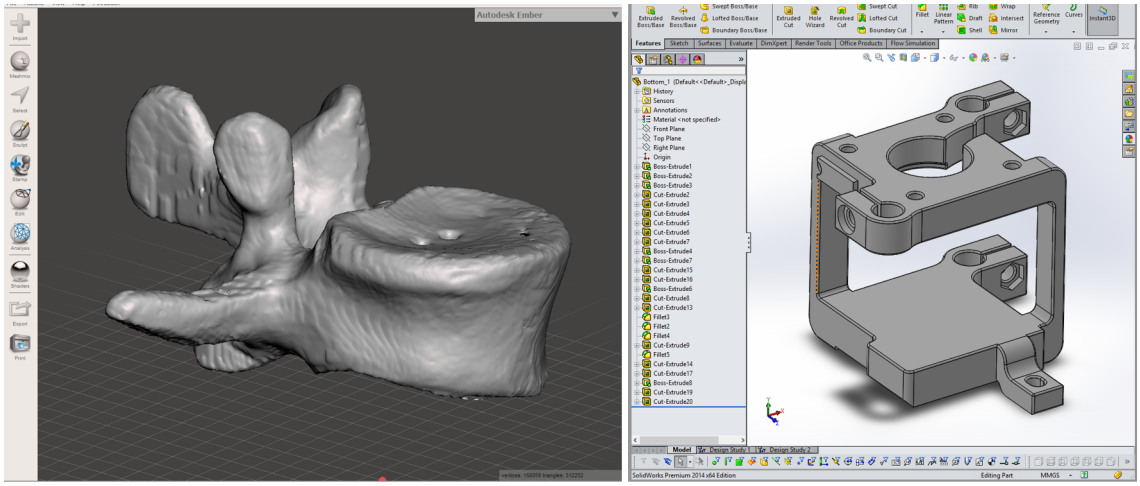


Figure 4.28: Example of a post-processed CT scan file in Meshmixer of a vertebra (left) and a model of a stepper motor holder of the new extruder in SolidWorks (right).

gives out a code that a 3D printer can read. A slicer needs to know all the parameters of the printer (printing area, type of a printer, maximum printing speeds, size of the nozzle etc.) and the used material (temperature of extrusion, die swell, diameter of the filament, etc.). Other parameters of a slicer also include layer height, number of shells, amount of infill, supports, raft, etc. Layer height defines the precision of printed models in vertical direction (most common layer height is $0.2mm$, but $0.1mm$ can be used for smaller parts or if higher precision is required). The number of shells defines the number of passes an extruder makes perpendicular to the surface of the model in horizontal direction (more shells are used for parts that need to be stiffer). Infill is the inner space of the model that is enclosed by the printed shells (surface of the model). Infill can be filled with different patterns giving a model structural rigidity. It is usually set to 10-20%, giving enough stiffness on one hand while reducing the total amount of material used for printing. Some models need temporary supports to be successfully printed (bridges, overhangs, etc.).

Knowing all these parameters, a slicer can generate a code that a printer can read.

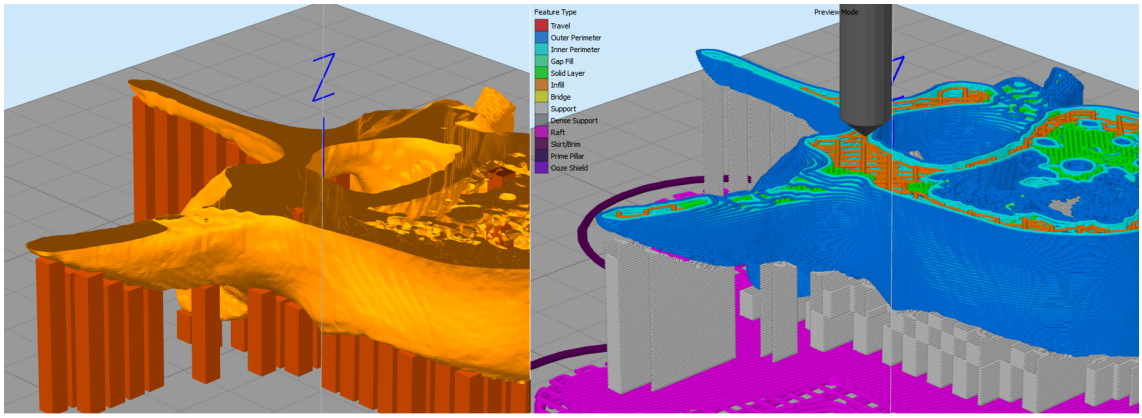


Figure 4.29: Example of a cross-section of a model of a vertebra in Simplify3D with supports (left) and the same model sliced (right), with different parts in different colors (shells in light and dark blue, infill in orange, supports in grey, raft in purple, etc.)

Ultimately, a model needs to be created (Figure 4.28), exported in STL file and put into a slicer (left in Figure 4.29). A slicer needs to know all the parameters of a 3D printer and how the model needs to be sliced. This allows the slicer to slice the 3D model (right in Figure 4.29) and generate a code. This code is usually written in g-code or x3g file. G-code is a standard code used by a variety of 3D printers and CNC machines. Whereas, MakerBot uses x3g files, that are essentially the same thing except they are written in a binary code. Both Simplify3D and MakeBot Desktop can output x3g files. Software MakeBot Desktop is the default slicer for MakeBot 3D printers. It was used for slicing all the models that were later printed in ABS. However, MakerBot does not allow for a manual control of the 3D printer. For printing with the hydrogels with a modified extruder, Simplify3D had to be used. It allows for a fully customizable printing area, dimensions of a nozzle and different federate of the material. This is essential, since the whole extruder was replaced and because of this modification the maximum printing area had to be reduced. This software also allowed us to preheat the syringe, and keep the temperature at all times, whereas MakerBot Desktop would stop heating after a print was done.

4.3.3 Printing hydrogels

To start printing hydrogels, we had to first modify the 3D printer's hardware, adapt the slicer's parameters based on the modifications and the material's rheological measurements, choose a 3D model and print it. We started with the GG hydrogel solution H0Ca1 and tried to print a model of a cube with a length of the edges of 10 mm without any infill and with two shells (each side wall of the cube had two passes of the printed hydrogel). Temperature of the hydrogel solution was chosen to be 3 $°C$ higher than the measured temperature of gelation (Figure 4.5). In the case of H0Ca1 where the temperature of gelation was measured at 41 $°C$, we set the temperature of the printing syringe to 44 $°C$.

After a few attempts, we managed to successfully print a square wall (Figure 4.30). The line printed around the square wall that measures only one layer in height, was printed for each model. This was done in order to start the hydrogel flowing making a more reliable first layer of the actual model. The layer height was set at 0.2 mm and the layers can be distinguished in the top layers. In the bottom part the surface is more smooth and the layers are not so visible. This is because after several printed layers, the hydrogel solution from the nozzle spilled on the surface, smoothing the surface after gelation. It is also worth

noting that the outside width of the square wall is increasing as the sample was built in height. Several samples also failed after being printed about 5 mm. The extruder stopped making continuous layer lines and started dropping droplets of hydrogel. Also, at the 90° corners it appeared that there was always more extruded material than in the straight line. Therefore we tested a more difficult model that would increase the difference between printing sharp edges and straight lines.

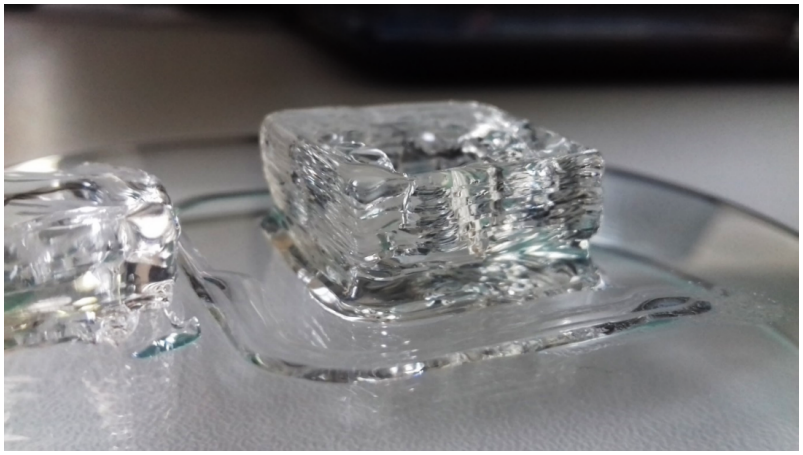


Figure 4.30: Square-shaped wall printed with H0Ca1 hydrogel solution with the side edge of 10 mm.

We printed a zig-zag pattern to compare printing straight lines to sharp 180° corners. The 3D model for this print was a regular cuboid with lower edges of 20 mm in length and height of 3 mm. However, we sliced the model differently than the previous example. We reduced the number of outer shells to zero, set the infill to 20 % and chose rectilinear infill pattern. This resulted in the pattern seen in Figure 4.31a. We can clearly see that the straight lines are very much alike and have a constant width. Also the 180° corners appear to be repeatable, but are wider than the straight lines. In Figure 4.31b we are looking at the same model from the side. We can see that the printed edges are higher (on the sides) than the straight lines (in the middle).

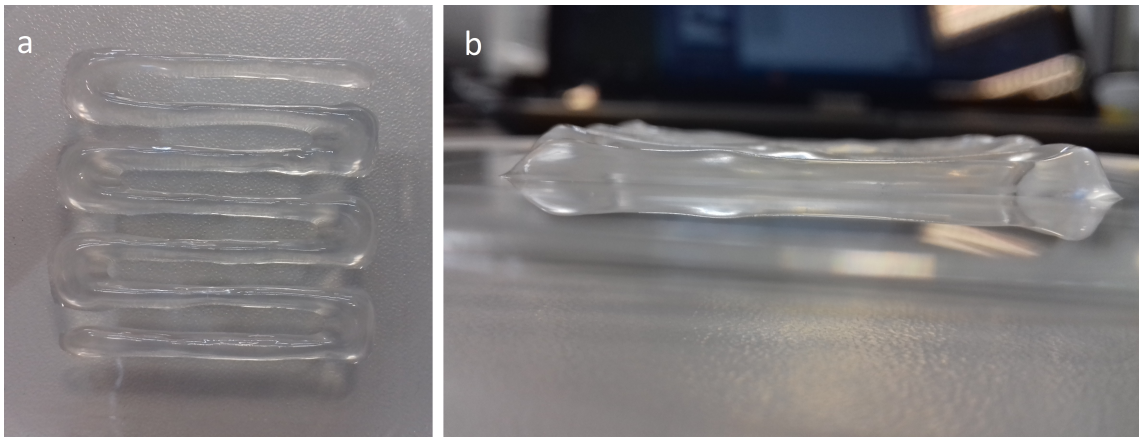


Figure 4.31: Zig-zag pattern printed with H0Ca1 hydrogel solution viewed from top (a) and side (b).

Another model was made where sharp edges were removed making it easier to print

(Figure 4.32). A cylindrical 3D model was made and the same as with the first example, the infill was reduced to 0 % and the number of outer shells set to two. These prints were more repeatable, whereas the surface finish was smooth and no layer lines are observed.

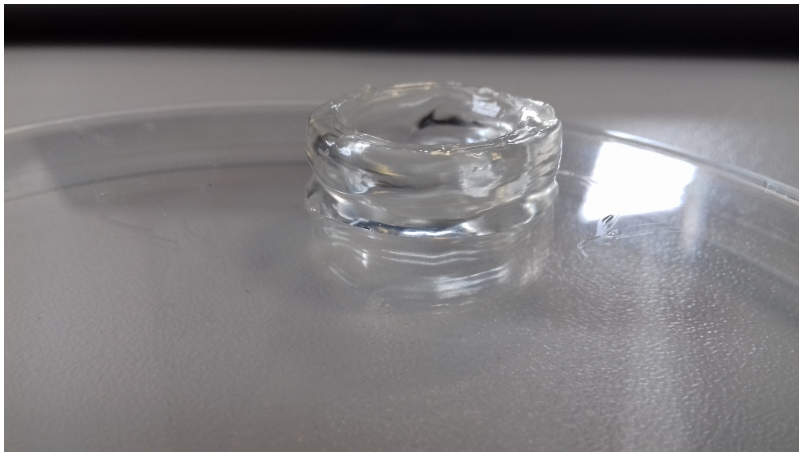


Figure 4.32: Cylindrically shaped wall printed with H0Ca1 hydrogel solution with a diameter of 10 mm.

Chapter 5

Discussion

Tissue engineering scaffolds need to meet several characteristics such as biocompatibility and biodegradability, however mechanical properties are also crucial, especially in load-bearing applications. In this discussion, I will explain the results we obtained from the five commonly found techniques that are used to measure mechanical properties, which we chose to test. I will critically evaluate each of the techniques, and at the end decide on one (or more) most suitable technique. This technique was used to track mechanical properties of the hydrogel samples submerged in the simulated bodily fluid (SBF). At the end, I will also comment on the possibilities of 3D printing GG hydrogel scaffolds. I will also try to convince you of the importance of the rheological properties of the hydrogel during 3D printing, and how rheometry can provide information needed for successful 3D printing.

5.1 Choosing the Technique for Characterization of VE Properties of Hydrogel Composites

In the tissue engineering field, it is already well established that mechanical properties of scaffolds are crucial and need to suit each individual patient. Therefore we can find a lot of information on mechanical properties of scaffolds, however it is often difficult to compare these results. This can be due to the different preparation of the samples, different measuring techniques and different measuring parameters. Very often we also see SEM micrographs of dried and porous hydrogel-based scaffolds that are related to its mechanical properties. Such dried scaffolds have very different mechanical properties as in hydrated state. Dried hydrogel scaffold behaves more as an elastic brittle material, opposed to a viscoelastic hydrated scaffold (explained in the last paragraph in Chapter 1.2.3). Mechanical properties of dried scaffolds depend on the architecture of its porous structure, which depends on the technique used to dry the scaffold. However, after such a dry scaffold is rehydrated, pores close due to the swelling of hydrogel material. Such a rehydrated scaffold exhibits the same mechanical properties at small deformation as the initial hydrogel sample that was used to prepare the porous scaffold [11]. Based on this, we have performed all the measurements on hydrogel samples, since they are expected to show a similar mechanical response as rehydrated scaffolds, which is how they would be used in a patient.

5.1.1 Uniaxial compression

Uniaxial compression is often encountered in literature as a method to represent mechanical properties of scaffold materials. From the measurements of samples (Chapter 4.1.1) we can

observe the expected reinforcement of the addition of BAG (Figure 4.3b), however after the initial reinforcement (by adding 2 wt. % of BAG) there is little additional reinforcement with a further addition of BAG. By looking at the stress-strain diagram (Figure 4.3b) it is even less obvious what the actual trend of reinforcement is. This comes from the fact that there are several factors, which affect compression measurements. Geometrical precision of the samples can be difficult to achieve with hydrogel samples, since they cannot be additionally grinded and polished. Therefore, a lot of care should be taken when pouring the samples in the mould to assure the top and bottom surface are as parallel as they can be. Since the samples had to be bigger than for the other techniques, deviation from the parallel surface could sometimes be observed visually. Consequently, we had to pre-compress the samples in order to ensure that the samples were in full contact with the measuring device. This again puts a question whether the samples reached non-linear deformation in this phase.

Non-linearity and viscoelastic deformation are also hard to define in uniaxial compression. At the beginning of the measurement, at the point where elastic modulus is extracted, deformation is not in a 'steady state', but more of a step up deformation coming from a standstill to a deformation of a certain strain rate. If the sample is purely elastic, this does not cause problems, but a viscoelastic nonlinear sample brings a lot of uncertainty.

Besides measuring elastic modulus of material, it is also very important to know at which point the material fails or irreversibly deforms. This should be observed in the stress-strain diagram (Figure 4.2). However, there is no obvious breaking point of the material, except for the GG-BAG sample there are some spikes at the end of the loading cycle. Looking at the unloading cycle it is clear that the sample could not recover approximately 25 % of the 27 % of deformation. This, along with a visual inspection, is a clear indication that the sample failed during experiment, but the measurement cannot provide the point at which this happened. This is because the hydrogels do not break abruptly as e.g. ceramics, but they start flowing.

5.1.2 Rheometry

Moving to the next technique, rheometry i.e. shear rheology, the results give many more information about our materials. Rheological measurements helped us to clarify the 'BAG particle reinforcement' that we saw while initially using uniaxial compression. The reinforcement effect could come from the addition of stiff BAG particles, or some other effect of BAG particles directly on the hydrogel matrix. While on the short term scientific mission in TUW, I learned about Mori-Tanaka model. This is a micro mechanical model used to predict mechanical properties of composites reinforced with homogeneously distributed particles. These particles can be spherical, as in our case, or even more rod-like with a specific orientation. The model requires mechanical properties of the matrix and the reinforcing particles. More known models like Voigt and Reuss model are meant for continuously reinforced composites with properties parallel and perpendicular to the reinforcement, respectively.

By using a measured elastic modulus of GG (uniaxial compression) and BAG (from indentation), we could predict the elastic modulus of composites with a desired amount of BAG particles (Figure 5.1). We soon realize that by the addition of 8 % of BAG, the increase in elastic properties is only 10 %. This is significantly less to what we have measured in compression, where the increase of elastic modulus was more than 100 times. Therefore, the increase of mechanical stiffness does not come only from the reinforcement of the particles themselves, but also by another mechanism.

Rheological measurements provided temperature of gelation of the composites. As we can see from Figure 4.4, the temperature of gelation linearly increases with the addition of

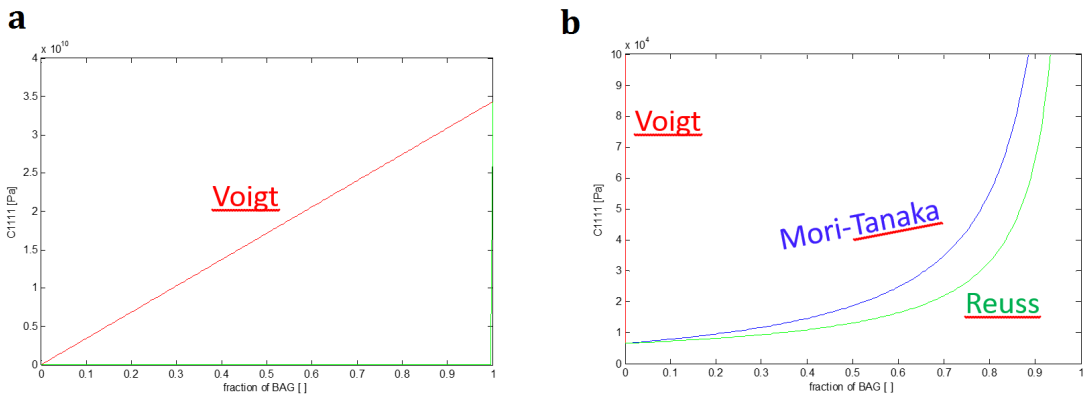


Figure 5.1: Models for predicting mechanical properties of composites with unidirectional fibres (Voigt and Reuss) and spherical particles (Mori-Tanaka) depending on the amount of reinforcing phase.

BAG. This means that the BAG particles also somehow affect the gelation process of GG gelation. One of the most probable explanations was that BAG partially dissolves during mixing in the water. This means that Ca^{2+} and Si^{4+} ions dissolve in water and can act as cross linkers. Therefore, we measured samples with 2 wt. % GG and without BAG with the same temperature sweep and added different amounts of $CaCl_2$ that would provide Ca^{2+} ions (Figure 4.5). A similar trend of increasing elastic modulus and temperature of gelation can be observed.

Looking at the results of added $CaCl_2$ we can observe a peak of shear modulus around 0.15 wt. % and a drop afterwards. However, the temperature of gelation seems to rise linearly until the highest measured concentration of $CaCl_2$. Since the solubility of $CaCl_2$ in water at room temperature is 0.42 wt. % and even higher at elevated temperatures, it means that during the measurements the samples never reached or surpassed the saturation point of $CaCl_2$. We can see from these results, that Ca^{2+} ions increase attraction forces among GG molecules when in the form of a solution, therefore even molecules with more energy, i.e. molecules at higher temperatures, can crosslink and form a polymer network. However, there is a limitation on how much Ca^{2+} ions can actually bond in GG double helixes, making the polymer network stronger. At highest concentrations of $CaCl_2$, where we see a decrease of elastic modulus, we can also assume that the non-bonded Ca^{2+} ions might actually affect the stiffness in a negative way.

Combining the results of added BAG and $CaCl_2$ (Figure 5.2), we can see similar behaviour for lower concentrations of added components. Up to 5 wt. % of BAG or 0.1 wt. % of $CaCl_2$ we can see a similar trend of reinforcement. Higher amounts of BAG were not added, since it was harder to achieve a homogeneous distribution of BAG in samples. There is some discrepancy in the results at higher concentrations of added components, which can be due to the additional Si^{4+} ions released from BAG that also act as cross-linkers.

Rheometry turned out to provide valuable information on our samples, however we had to prepare the samples in the rheometer fixture and then measure them. Such samples cannot be put out of the rheometer and back again to do another measurement. The first reason is that they are too thin and would be damaged, as well as the rheometer relies on a very precise geometry and positioning of the sample in the fixture that could not be assured by removing and again placing the sample by hand. Therefore, a similar but a more robust technique is the dynamic mechanical analysis (DMA).

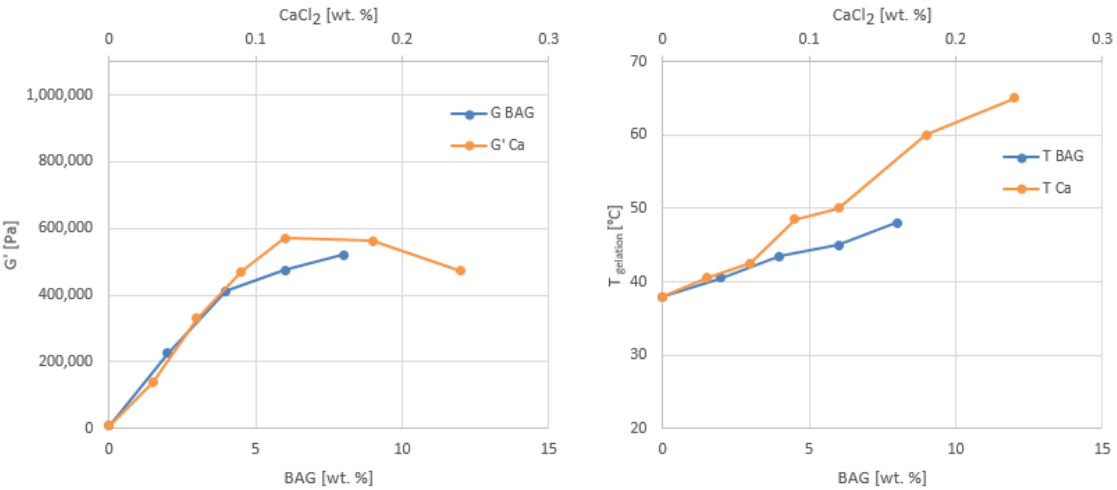


Figure 5.2: Storage modulus (left) and temperature of gelation (right) of composite samples of GG and BAG, and GG with added $CaCl_2$. Scales of BAG and $CaCl_2$ addition are fit based on the shape of curves.

5.1.3 Dynamic mechanical analysis

DMA frequency sweep results of gelled samples can be directly compared to the frequency sweep in rheology (Figure 5.3). We can see that the frequency dependence of G′ and E′ is very close, while the frequency dependence of G″ and E″ deviates at higher frequencies. The reason lies in the type of deformation. While both deformations are sinusoidal in the linear region, DMA measures in compression while rheometry in shear. There is one fundamental difference in compression and shear. In compression (uniaxial and unconfined), the volume of the sample changes, while in pure shear the volume does not change. Since hydrogel samples contain a lot of water, a change of volume i.e. deviator stress will impose fluid flow in the sample. If volume changes are slow and small, the water flow induces negligible forces, but when the volume changes are faster, the dissipation forces increase. This can be seen in the figure below. Hydrogel network by itself has a distinct frequency dependence of loss modulus (dissipation) that is observed in the results of shear rheology, while in DMA results the frequency dependence is similar but with higher dissipation at higher frequencies because of the flow of water.

DMA could also provide measurement of the point of failure of hydrogel samples. As stated, knowing the point of failure of tissue engineering scaffolds is crucial, however there is little information on how to determine it. Creep measurements are possible on some DMA devices, but not all. By measuring the creep, we can determine if the sample can resist a certain stress for a desired amount of time. Simple uniaxial compression measuring devices usually do not provide stress-controlled measurements, but only strain-controlled measurements that have less relevance to the actual situation of an implanted scaffold.

In Figure 4.12 we see the results of creep experiments of GG-BAG composite samples at different compression forces. All of them show viscoelastic response in the first minute, after which the deformation stabilized. Most of the samples stabilized to a horizontal plateau, except for the last sample that was exposed to 1.2 N creep force. The first samples reaches a plateau and stops deforming. This is a proof that such a sample can withstand stresses that are exerted at a compression force of 0.8 N and lower. However, when the compression force is raised to 1.2 N, we can see that after the initial viscoelastic deformation, the deformation does not stop. The sample keeps on deforming. This means

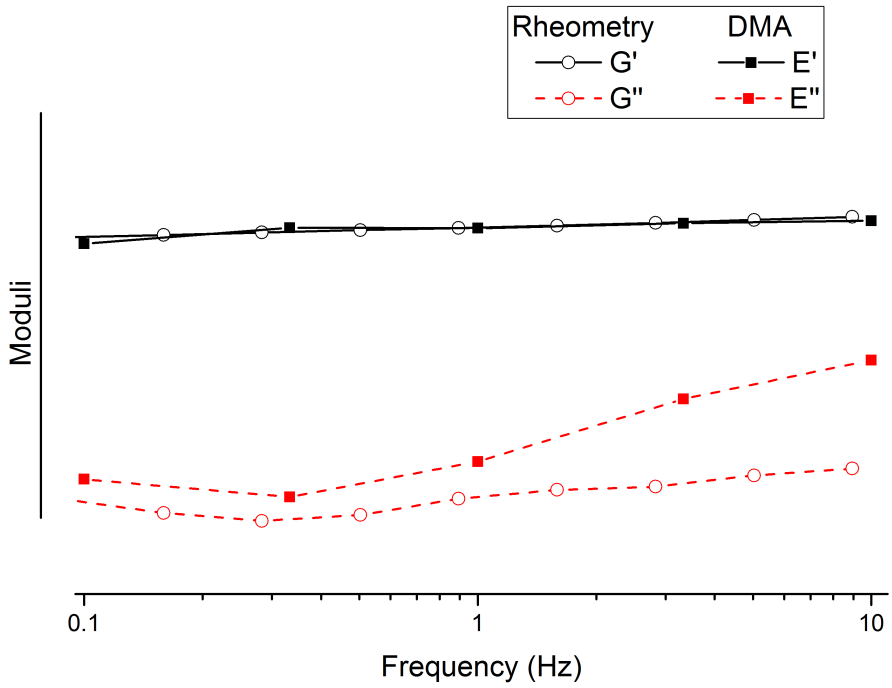


Figure 5.3: Frequency sweep of H0 sample from rheometry (open circles) and DMA (full squares) vertically shifted to match the storage moduli.

that eventually the sample will be squeezed, as it cannot withstand the stresses.

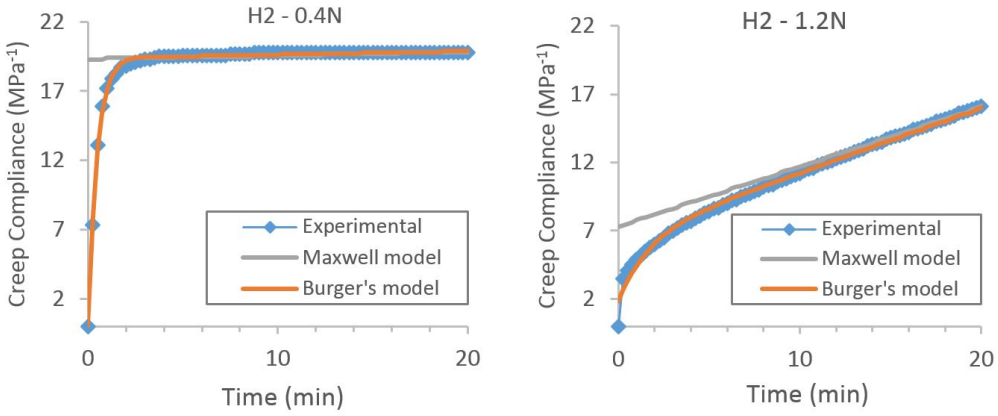


Figure 5.4: Creep experiments of H2 sample at 0.4 N (a) and 1.2 N (b), with fitted Maxwell and Burger's model.

In order to determine the maximum stress a sample can withstand, we need to find a parameter that will describe at which point the material starts flowing. In order to do that, we fitted the data to the Burger's model (Figure 5.5). This was performed using a Matlab script with the least squares method using the following Equation 5.1.

$$D = \frac{t}{\eta_2} + \frac{1}{E_1}(1 - \exp(-t/\tau_1)) + \frac{1}{E_2} \tag{5.1}$$

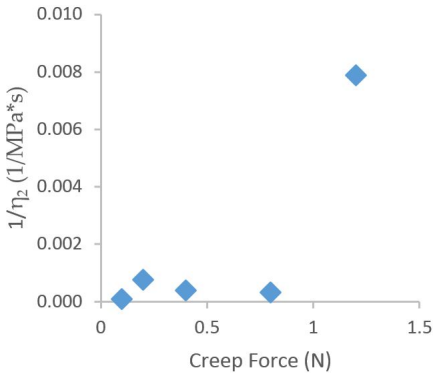


Figure 5.5: Flowability of H2 samples ($1/\eta_2$).

From the plot of the fitted parameters of flowability ($1/\eta_2$), we can now observe at which creep forces the samples starts to 'flow' i.e. breaks. In order to determine the maximum stress such samples can withstand with higher precision, we would need to perform more experiments at different creep forces. However, from the obtained results we can see that below 0.8 N the sample will retain its shape and not fail. Such a force results in a pressure of 29.3 kPa in the material, that can be compared to a steady-state pressure in the articular cartilage [53].

Further improvement of this method should also include determination of the scale of observation. As we can observe from the diagram above (Figure 5.5), we can see that the fitted parameter is always above zero. This means that there is always some flow of the material, which can be neglected in practice. However, one could assume that there was failure of the sample already at 0.2 N if the vertical axis would range from 0 to 0.001 $1/MPa^*s$, since the flowability is higher than with the sample at 0.1 N. Therefore, there is a need to determine either the maximum amount of flow that is not considered as a failure of the sample or a way to describe the point at which the flowability drastically increases.

5.1.4 Indentation

Another technique we used was indentation. Unfortunately, most of indenters are meant for stiffer materials, therefore we could not measure even our most stiff samples. There are also so-called nano-indenters that can measure forces in the range of nN (10^{-9} $Newtons$), which would be able to characterize our samples, but unfortunately we did not have such a device available. However, indentation provided reliable measurements of our BAG.

Since an individual particle of BAG could not be measured, we have sintered BAG at low enough temperatures not to induce any crystallization. The obtained value of $E = 26.7 \pm 8.4\ GPa$ seemed appropriate for a fully amorphous BAG, although there was a substantial deviation of the results. Under closer observation, we have observed that there might actually be a bimodal distribution of measured elastic moduli. Each measurement (Figure 4.16) was assigned, a certain standard deviation and then all measurements were summed up using the probability density function (PDF) using the following Equation 5.2.

$$P = \sum_{i=1}^{23} \left(\frac{1}{\sigma\sqrt{2\pi}} \exp^{\frac{-(x-\mu_i)^2}{2\sigma^2}} \right) \tag{5.2}$$

Where σ is standard deviation of a measurement that was chosen (0.1, 2.0 or 8.4 GPa) and μ_i is the result of each measurement.

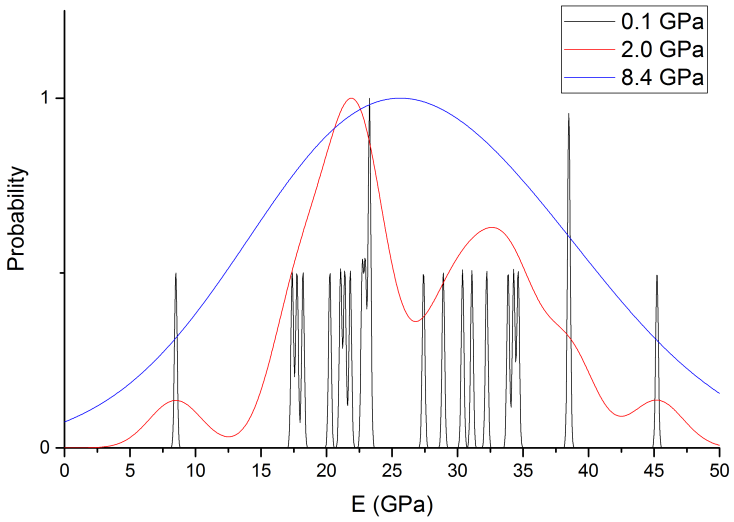


Figure 5.6: Indentation measurements fitted to PDF with different standard deviation values (0.1, 2.0 and 8.4 GPa).

Starting at the calculated standard deviation of 8.4 GPa, we can observe a distribution close to a Gaussian. However, as we decrease standard deviation, we start to observe a bimodal distribution. By setting the standard deviation to 0.1 GPa we could observe peaks of individual measurements, which gave us a better look at the fact that the measurements occur more often around two values. This can be seen more clearly at standard deviation of 2.0 GPa, where we can observe two distinct peaks at 21.9 and 32.6 GPa (Figure 5.8).

Two distinct moduli could occur due to several reasons. By keeping the temperature of sintering low enough, we are assuming that all the BAG particles are still amorphous and there should be no difference in elastic moduli of individual fused particles. We are also assuming that the surface is sufficiently flat. This was observed by an optical microscope, which is not the most reliable method, but it was obvious that there were no visible imperfections where the indentations were made. In addition, the position of each indentation was beforehand determined by looking through a microscope. Since sintered BAG is porous, there is a possibility that the indenter is sometimes indenting in an area below which pores are positioned (Figure 5.8). These kinds of places on the sample induce lower stresses, therefore the material seems softer. To determine the right cause of two distinct values of measured moduli, a more detailed study should be done. Since this is not the main focus of this work, elastic modulus of 26.7 ± 8.4 GPa was used.

5.1.5 Ultrasonic Wave Propagation

For measuring the density of GG-BAG composites the Archimedes measuring technique was chosen. The problem with calculating the density of hydrogels based on dimensions

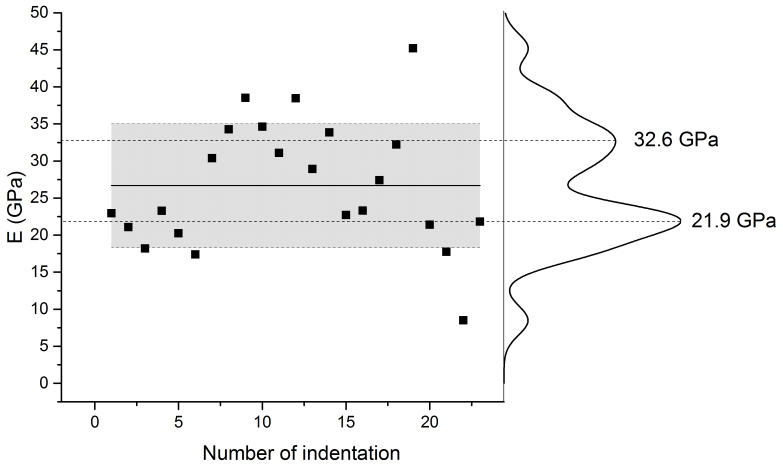


Figure 5.7: Results of indentation measurements and probability of measured elastic modulus at $\sigma = 2.0\ GPa$.

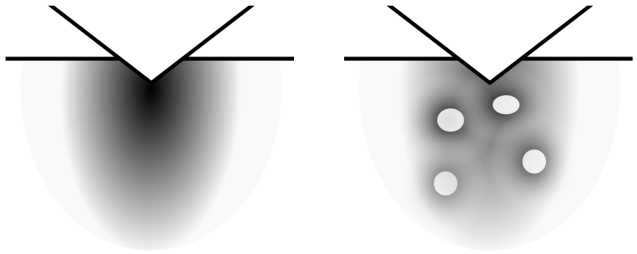


Figure 5.8: Indentation in bulk (left) or porous (right) material.

and mass is measuring the dimensions. The problem is using calipers to measure hydrogel samples, because pure hydrogels are very soft and they deform significantly when compressed with a caliper. After the addition of BAG, hydrogels became stiffer, resulting in less deformation of the samples when measuring with a caliper. This can be seen in Figure 4.17, where the measured densities by both techniques are closer for the samples with a higher amount of BAG, whereas the deviation is higher for the samples with less BAG. This means that different compositions deformed differently, therefore not just the absolute density measured by calipers and scale is questionable, but also a relative difference between the composites. A solution we could have taken, would be to measure the samples' volumes by the displaced liquid method, where one measures the amount of liquid a sample displaces, which is equivalent to the sample's volume. Forces on a sample in this case are negligible.

On the other hand, Archimedes density measuring technique provided measurements that are more consistent. This was because mechanical stiffness of the samples does not affect the measurements. What looked to be a problem was the fact that we measured the weight of the hydrogels ($90 - 98\%$ of water) in water. This meant that the buoyant force of the sample was close to the weight of the sample, resulting in small weight reading on the scale while the sample was submerged in water. Despite this we were able to measure

the density well. We could have replaced the liquid in which we measured the samples in, with a liquid with a smaller density, but we had no such appropriate liquid at that time.

We expected different speeds of ultrasonic wave propagation through the samples of different compositions, since uniaxial compression, rheometry and DMA showed reinforcement with the addition of BAG. However, speed of ultrasonic wave propagation did not change with the addition of BAG (Figure 4.18a), only the calculated moduli (Figure 4.18b) showed a small reinforcement, which was only due to the change in density. It is also worth noting the significant standard deviation of the calculated elastic moduli, which is due to squaring of the measured velocity of ultrasonic waves. This implies that precisely measuring the velocity is crucial for good results of the calculated elastic moduli.

Calculated elastic moduli are also too high compared to the results of other techniques. The calculated values of elastic moduli are around 800 MPa, whereas other techniques give results under 1 MPa. Therefore, it is obvious that these results do not represent the actual mechanical properties of these samples that we observe with other techniques. Speed of longitudinal waves is $1.51 \pm 0.04\ km/s$, which is similar to the speed of ultrasonic waves in water (1.48 km/s). Since longitudinal waves can propagate trough water and all the samples contain more than 90 % of water, we can conclude that the longitudinal waves mainly propagate through the water in the samples. However, transversal waves cannot travel through liquids, therefore they had to travel through the hydrogel matrix. Despite that, measured shear modulus of the hydrogel is almost three orders of magnitude higher compared to other techniques.

The high frequency of the measuring technique like ultrasonic wave propagation (0.1–1 MHz) is known to be able to measure mechanical properties of metals and ceramics [Handbook of Materials Selection], whereas it is not well defined for polymers. Several polymers were measured with this technique [54], but no direct connection to elastic modulus was mentioned. Therefore, I gathered measurements of ultrasonic wave propagation technique and other conventional techniques from different sources [54]–[56] and put them in the following diagram:

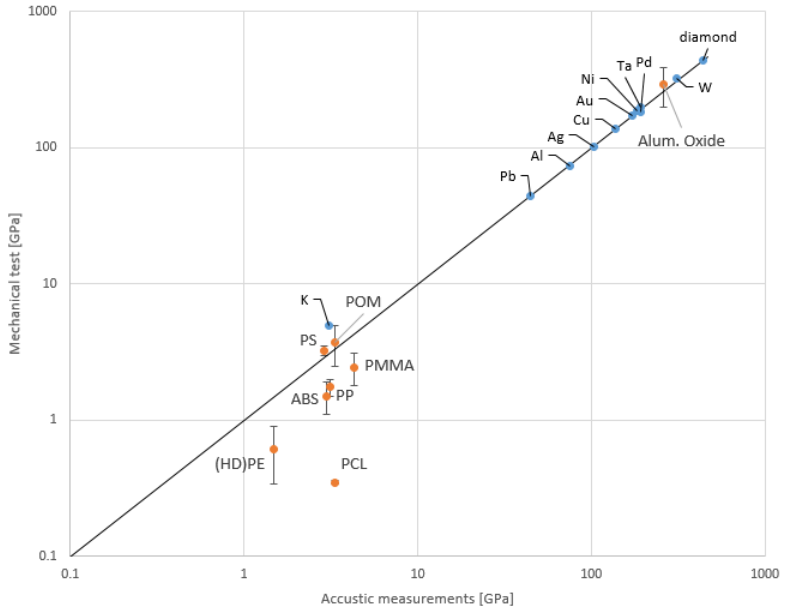


Figure 5.9: Comparison of elastic modulus measured with mechanical test and predicted with acoustic measurements for different materials.

We can clearly see the good agreement between the measurements of conventional tests and acoustic measurements for the metallic materials, whereas several polymers show significant deviation. This could be a consequence of frequency dependant behaviour. PCL (polycaprolactone) and HDPE (high-density polyethylene) have the biggest deviation and what they have in common is a low temperature of glass transition ($-60\ °C$ and $-120\ °C$, respectively), meaning that they are in a rubbery region under room conditions. While conventional techniques measure samples at room temperature at physiologically relevant frequencies, ultrasonic wave propagation measures these samples at very high frequencies (10^6 higher frequencies).

Based on the high elastic modulus calculated from ultrasonic wave propagation technique and poor agreement for polymers in rubbery region, we can assume that ultrasonic wave propagation measurements give mechanical properties of polymers in a glassy region. As discussed in Chapter 1.2.3, mechanical properties of polymers in a glassy region depend on internal energy between atoms in the polymer molecules, resulting in orders of magnitude higher elastic moduli than polymers in rubbery region, where the main driving force of elasticity is entropy of polymer molecules. This implies that the main reason for the difference in measured elastic modulus, e.g. between rheometry and transversal ultrasonic wave propagation, is the difference in the frequency of excitation combined with the high frequency-dependent mechanical properties of polymers.

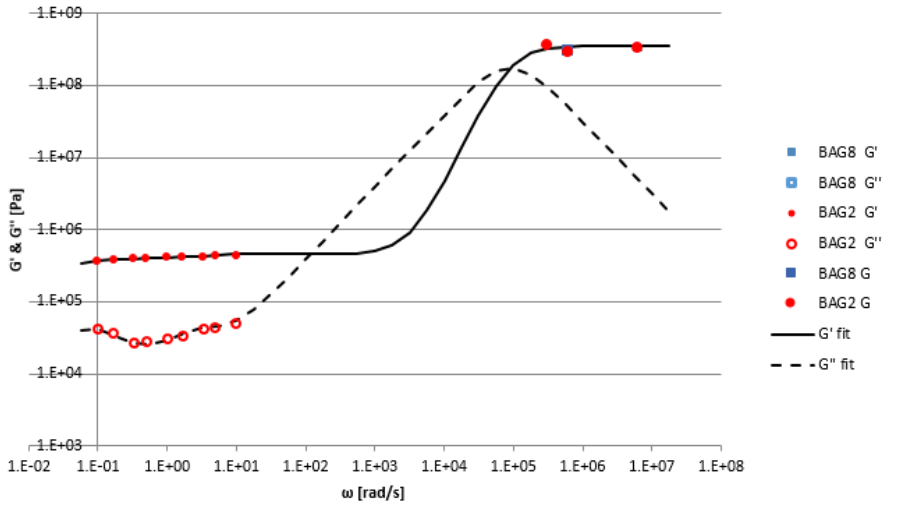


Figure 5.10: Rheometry and ultrasonic wave propagation measurements linked using generalized Maxwell model.

By combining results of rheometry and transversal ultrasonic wave propagation for H1 composite samples on a frequency scale diagram, we can clearly see the difference. Besides glassy and rubbery region, polymers exhibit a transition region in which polymer molecules relax from one state to another. The fastest way for a polymer molecule i.e. viscoelastic material to relax is by a Maxwell model, which we fitted to the results of both techniques. Complex modulus of a Maxwell model is obtained in the following way:

$$G' = G_0 + \sum_i G_i \frac{\lambda_i^2 \omega^2}{1 + \omega^2 \lambda_i^2} \tag{5.3}$$

$$G'' = \sum_i G_i \frac{\lambda_i \omega}{1 + \omega^2 \lambda_i^2} \tag{5.4}$$

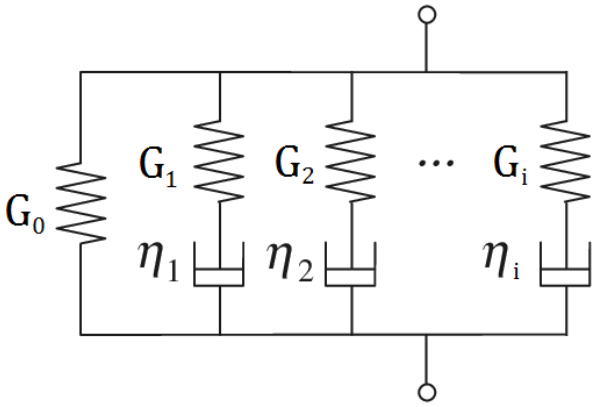


Figure 5.11: Schematic of Generalized Maxwell model.

Fitted constants are listed in the following Table 5.10.

Table 5.1: Constants of Generalized Maxwell model (Figure 5.11) that were used in Figure 5.10.

i	$1/\lambda$ $[1/s]$	λ $[s]$	G $[Pa]$	η $[Pa*s]$
0			$3.20*10^5$	
1	$1.25*10^{-2}$	$8.00*10^1$	$8.00*10^4$	$6.40*10^6$
2	$3.33*10^{-1}$	$3.00*10^0$	$2.00*10^4$	$6.00*10^4$
3	$5.00*10^{-1}$	$2.00*10^0$	$4.00*10^4$	$8.00*10^4$
4	$1.43*10^4$	$7.00*10^{-5}$	$3.50*10^8$	$2.45*10^4$

We can see from the fitted curve (Figure 5.10) that by using one Maxwell model ($i = 4$ in Table 5.1) we can fit results from ultrasonic wave propagation measurements, while several models in parallel ($i = 0, 1, 2$ & 3) had to be used to fit results from rheometry. After the fitting to the experimental results, we can see that the model allows relaxation of the polymer molecules to happen in the frequency window between both techniques. This shows that the ultrasonic wave propagation technique could give data on glassy modulus of a hydrogel at ambient conditions. Otherwise, hydrogels are mainly in a rubbery region, due to the water molecules acting like a solvent and increasing the mobility of molecules. This means that the obtained results have no practical correlation with the actual mechanical properties of hydrogels.

There were several attempts to clarify results of ultrasonic wave propagation measurements of hydrogels, but none of them provided any solid proof. [57] did work on agarose hydrogels, where several concentrations of polymer were used to make hydrogels. Looking at Figure 5.12, we can see similar results as we obtained. Conventional method (unconfined uniaxial compression) gave results in the range of MPa, while ultrasonic wave propagation measurements gave results two orders of magnitude higher. They have tried to explain the results using a poroelastic model, but provided no solid conclusions.

Ultrasonic wave propagation was also used to monitor crystallization of thermoplastic polymers [58]. While such a polymer is hard to compare to hydrogels, we can observe some

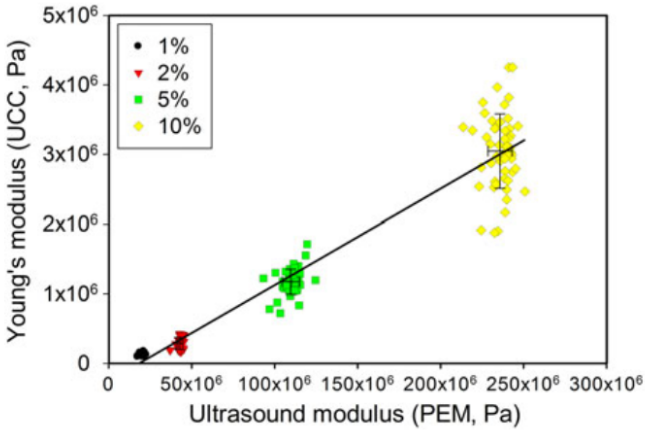


Figure 5.12: Correlation of results of mechanical and acoustic tests on agarose hydrogels with a concentration ranging from 1 to 10 % [57]

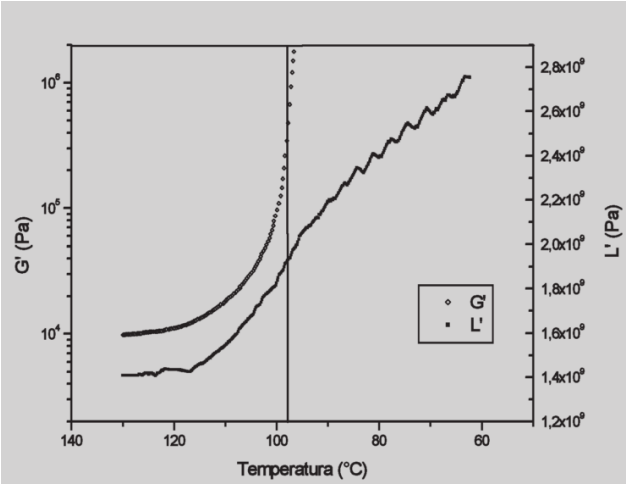


Figure 5.13: Correlation of shear modulus from DMA measurements (open circles) and longitudinal moduli from ultrasonic wave propagation (solid squares).

similarities. Thermoplastic polymer is in the form of a melt at a higher temperature and it crystalizes upon cooling. During crystallization, the mechanical i.e. viscoelastic properties increase. DMA shows increase of moduli (G') of several decades, while the longitudinal modulus (L') only shows an increase of by a factor of two. Again, the difference of measured moduli cannot be neglected.

In 2007, Hugh [59] did his PhD work called 'Ultrasonic Technique for the Dynamic Mechanical Analysis (DMA) of Polymers', where he explained the connection between DMA and ultrasonic wave propagation technique for an epoxy resin. In this work, he found out that he could connect results of both techniques using WLF (Williams–Landel–Ferry) time-temperature superposition [60].

5.1.6 Comparison of all techniques

For my work, the goal was to determine the most suitable technique for measuring polymeric scaffold materials i.e. hydrogels. We saw that indentation was not suitable for

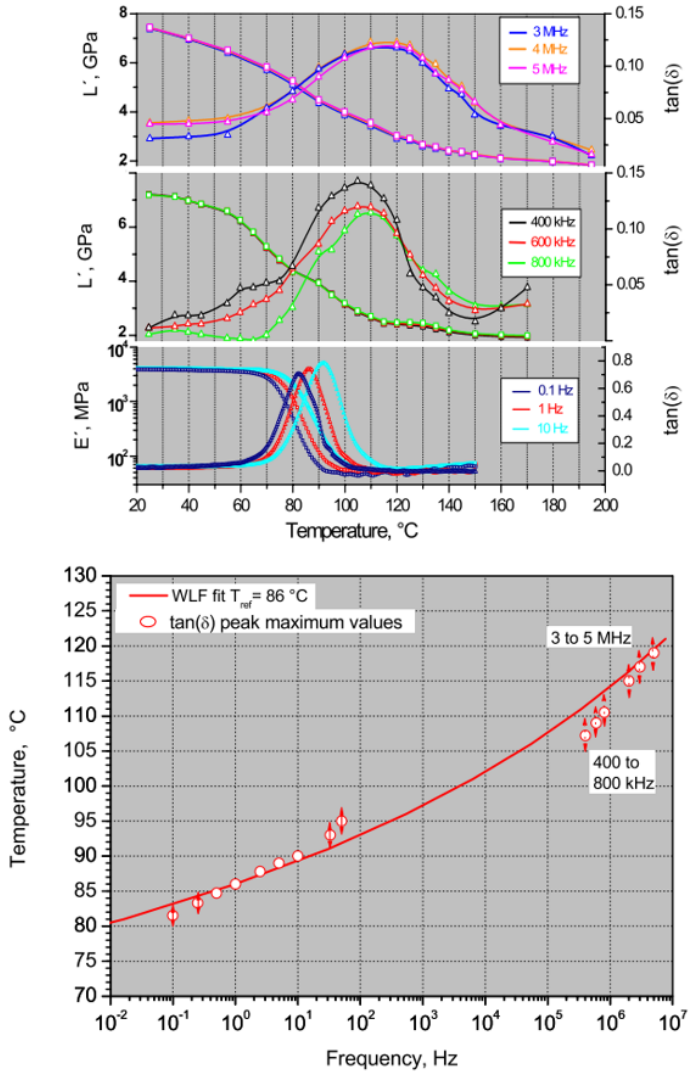


Figure 5.14: Coorelation of DMA and ultrasonic wave propagation measurements of epoxy by [59].

hydrogels, unless the indenter would be specifically made for such soft materials. Ultrasonic wave propagation technique was able to measure the samples, but the results are hard to interpret. We have concluded that the results do not represent mechanical i.e. viscoelastic properties of the samples at ambient conditions, but rather properties at higher frequencies that are not relevant in scaffold applications.

Other three techniques: uniaxial compression, rheometry and DMA were found to be more suitable. Rheometry provided viscoelastic properties of hydrogel samples during gelation of the samples, temperature of gelation, as well as viscoelastic properties of the hydrogels in a liquid and solid state. Uniaxial compression and DMA could only measure solid hydrogel samples, however the samples could be made in advance. While uniaxial compression can measure the sample's elastic modulus, dissipation i.e. viscosity cannot be reliably assessed without performing measurements of several samples of the same composition. DMA can reliably give results of elastic and dissipative modulus at different frequencies of excitation, which are relevant to the actual forces that can occur to an implanted scaffold [1].

Viscoelastic properties during degradation were measured using DMA. This technique was chosen based on the results from Chapter 4.1. Compared to uniaxial compression, it gives more information, like dissipative modulus and frequency dependence. DMA also requires smaller samples, which means that any uneven surface will be less pronounced. Rheometry does provide a similar amount of information, but it is not suitable due to the fact that the gelled samples cannot be taken out of the rheometer fixture and put back again, which is needed for the incubation.

5.2 Viscoelastic Properties During Degradation

Special care had to be taken to avoid evaporation of water during degradation tests. Having the samples at an elevated temperature (36.5 $°C$) in a multiwell plate would cause the water to evaporate from the SBF solution. This led to an increase of the concentration of ions in SBF and consequently precipitation of salts, mainly on the samples. This happened, because the multiwell plates do not provide an airtight seal. Initially, we tried to solve this with a plastic paraffin film (Parafilm, Bemis USA), but we still observed evaporation of water. At the end, we solved the problem using an electrical tape.

Every measuring day, the samples were taken from the incubator at least 2 hours before the measurement to cool down to room temperature. Special care was taken to ensure that the water from the samples did not evaporate, therefore they were kept in SBF until the time of measurement and once placed onto the measuring fixture, and a drop of SBF was placed around the sample. At the end of measurement, samples were checked that the excess SBF remained. Since the measurement took around 10 min per sample and it was done at room temperature, the evaporation during the measurement could be neglected. Nevertheless, each sample has gone through two consecutive frequency sweeps to be sure the measurements were repeatable.

In Figure 4.20, FT-IR measurements of all the samples show the typical bands for GG polymer. Whereas, typical bands for HA are most prominent for the samples that were incubated for 28 days. There is a clear separation of the 556 cm^{-1} and 601 cm^{-1} bend peaks that differentiates the samples at day 0 and day 28, suggesting that the amount of crystalline HA is significantly higher after a longer time of submersion in SBF. However, sample H1 at day 0 also shows a peak in the same area, but has a less significant separation of peaks. It also exhibits the *P-O* stretching vibration modes of HA around 1050 cm^{-1}, meaning that even at day 0 there is some HA on the H1 samples, whereas none is detected on H0Ca1. This most likely happened because even the samples at day 0 were left in SBF for 3 hours, in order for them to swell up. This clearly shows that the formation of HA is accelerated when BAG is added to the samples. However, after 28 days the difference becomes less obvious.

SEM micrographs have not shown the expected crystals of HA as seen in literature [11]. However, there was a difference in the degradation test, since I was changing the SBF solution every other day, they have kept the samples in the same SBF solution for the whole duration of the test. This means that in average my samples were exposed to a higher concentration of ions since we had fresh SBF constantly. The particles that cover our samples (Figure 4.22) and are 500 nm in diameter, are salt crystals. They have most likely precipitated during freeze drying. This could have been avoided if the samples would have been washed with pure water before being frozen. However, I wanted to avoid this, since washing with pure water would change the ionic concentration in the hydrogel changing the amount of swelling of samples and also their mechanical properties, that are the main focus of this work. Never-the-less, on a closer look, in Figure 4.23 we could see particles of 500 nm in size forming aggregates. These aggregates could be the HA that we

detected with FT-IR measurements. Since we were changing the SBF solution every other day, it is possible that the solution was constantly precipitating on the edges of just grown HA crystals, and the crystals did not have the time to slowly grow in larger crystals.

Viscoelastic (VE) properties measured with DMA (Figure 4.19) have not shown any degradation. We have expected that during 28 days of submersion samples' VE properties would decrease, at least for the H0Ca1 samples. However, on day 28, VE properties of H0Ca1 and H1 have increased. There was a small decrease of VE properties of the H1 samples in the first 7 days, after which the G' started ascending with a similar trend as H0Ca1 samples.

This suggests that both samples were too stable to degrade in SBF. Most likely, due to a significant crosslinking of both samples, the GG hydrogel network was too strong to allow for degradation of the network. However, even if the samples would have been less crosslinked, the high concentration of ions in SBF (also $CaCl_2$) could additionally crosslink the hydrogel samples. This would mean that no matter how much we crosslink the GG hydrogel in advance, it would not degrade. However, to confirm this statement, we would need to perform experiments to see if GG hydrogels can be crosslinked additionally in the presence of $CaCl_2$ ions.

5.3 Additive Manufacturing

While measuring the rheology of gellan gum hydrogels and their composites with BAG, we have seen the potential of using their thermal gelation for 3D printing. This would give new opportunities for shaping scaffolds for tissue engineering applications. 3D printing allows fabrication of shapes that cannot be made using other techniques, e.g. mould casting, salt leaching, freeze-drying, etc. However, 3D printer has to be able to work with the chosen material.

Since GG experiences thermal gelation upon cooling, the idea was to keep GG as a solution at an elevated temperature in a syringe and extrude it during printing. During extrusion, the solution comes out of the syringe nozzle, cooling down in contact with air and the printing surface. Cooling of the solution is a very complex, due to several parameters affecting it, for example: rate of extrusion, initial temperature of the solution, temperature of the surrounding air, speed of the air around the nozzle, etc. Because it is very hard to determine the effect of each parameter in advance, we rely mostly on the visual observation of the gelled material and final characteristics of the printed sample. Ideally, the material should gel right after coming out of the nozzle in order to leave a predictable trace of the gelled material on the printing surface or the lower printed layers, otherwise the solution can spread on the surface without control. If the material gels already in the nozzle, it could block the nozzle or just form an uneven trace of material. However, if the materials is too cold, it will not bond with the lower layer. This could end up with a sample that shows delamination, i.e. layers do not stick together.

Most commonly used materials for FFF (fused filament fabrication) printing are thermoplastic polymers. They work on a similar principle of thermal solidification of the polymer on exiting from the nozzle. However, most commonly used thermoplastic polymers (PLA, ABS, PA, etc.) exhibit solidification at higher temperatures (200 – 240 $°C$) which brings some advantages. One of them is that when such hot molten polymer exits the nozzle, it cools down very fast due to a high temperature difference between the polymer and the surrounding air. This also assures that the produced part will not melt at elevated room temperatures, although such polymers are not suitable for higher temperature applications. Another advantage of thermoplastic polymers is that they can be melted (unlike hydrogels that usually cannot liquefy upon heating), which means they can

be stored as solids (most commonly in the form of a filament).

Initially the syringe was heated with the original cylindrical metal heater that was used to heat the hot-end's brass nozzle up to 240 $°C$. The heater was powerful enough to heat up the syringe to 90 $°C$, but the heating was very uneven across the volume of the syringe. On top of that, the used plastic syringe deformed with time under elevated temperature. To solve these issues, we replaced the plastic syringe with a glass one together with a fully metal needle. To solve the issue with the heating, we replaced the original cylindrical metal heater with a costume-made flexible foil heater rated for 24 V and 15 W (made by Dongguan Gui Xiang Insulation Material Co., China). The foil heater, with an adhesive tape on one side, was adhered around the syringe barrel. The thermocouple was wrapped in aluminum foil, to insure a good heat conduction from the heating foil, and mounted on the outer side of the foil heater to control the temperature. Everything was then wrapped in insulating material to reduce heat loss and to keep the temperature in the syringe constant.

By keeping the original thermocouple and replacing the heating element, we could still control the temperature in with the printer's feedback loop. This means that we can now set the extruder temperature in the slicer (MakerBot Desktop 3.10 or Simplify3D) to the desired temperature and it will heat up the syringe to that temperature. For convenience, we also modified the default settings of the printer's firmware in the slicer by clicking 'device preference' and adjusting the preheating temperature to 80 $°C$. This allows us to preheat the empty syringe beforehand and avoid partial gelation of the suspension when it is poured in the syringe.

Hydrogel solution had to be carefully prepared each time. It is crucial that the solution does not gel, as it would cause uneven flow from the syringe, or it could clog the syringe nozzle. Therefore, the solution was always prepared at least 10 $°C$ above the expected gelation temperature. Special caution was put on the addition of $CaCl_2$ solution. It was always preheated and then slowly poured into the GG solution. If the solution gelled locally, it would show as a slightly opaque particle (Figure 5.15). Such a solution would be discarded and made again from the start.

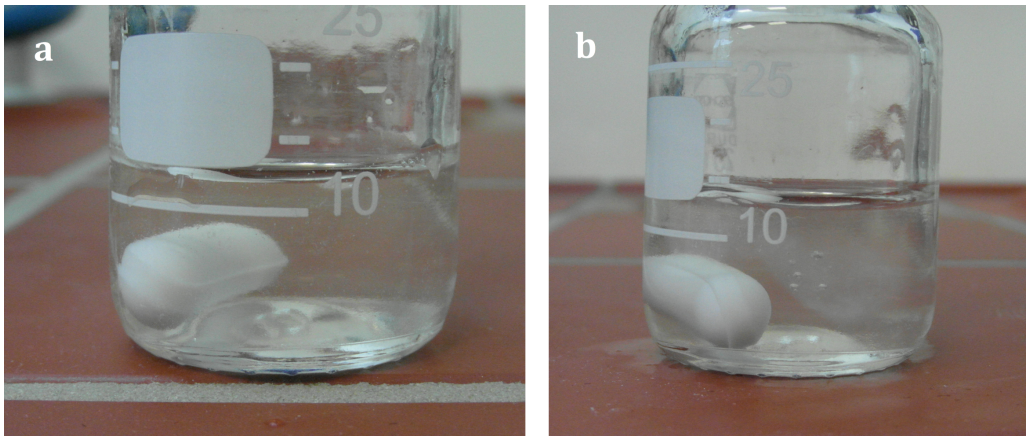


Figure 5.15: A well prepared (a) and partially gelled (b) GG solution with added $CaCl_2$.

The prepared solution is then poured into the syringe barrel. When the syringe plunger was inserted into the syringe barrel filled with the hydrogel solution, special attention was paid leaving no air trapped in the syringe (Figure 5.16). Since air is significantly more compressible as the hydrogel solution, it would act as a spring during extrusion. When the syringe would be compressing, the air would compress, instead of the solution being

extruded. This would cause inconsistent extrusion. Therefore, no air was left in the syringe before the printing started.

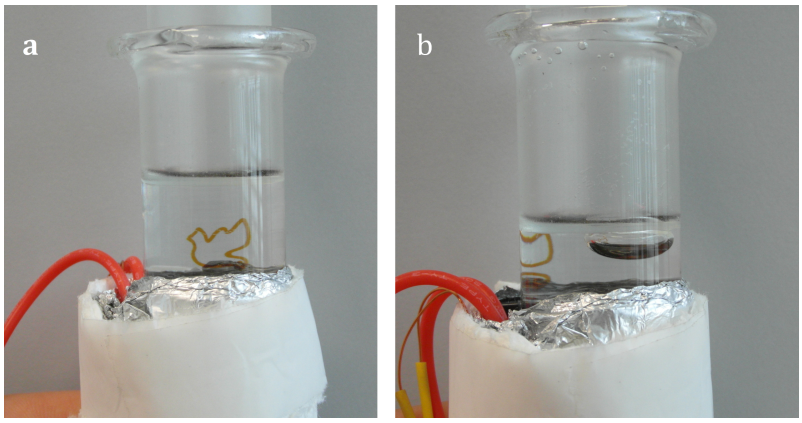


Figure 5.16: Syringe with a properly prepared hydrogel solution (a) and with unwanted air bubble (b)

The solution in the syringe was always kept 3 $°C$ above the start of gelation. The predetermined starting gelation temperature could be obtained from rheology of the GG solution. For the sake of simplicity, Figure 4.6 was plotted in moduli vs temperature (Figure 5.17), so the starting temperature of gelation can be determined. For example, sample H0 was printed at 43 $°C$, whereas sample H1 was printed at 58 $°C$.

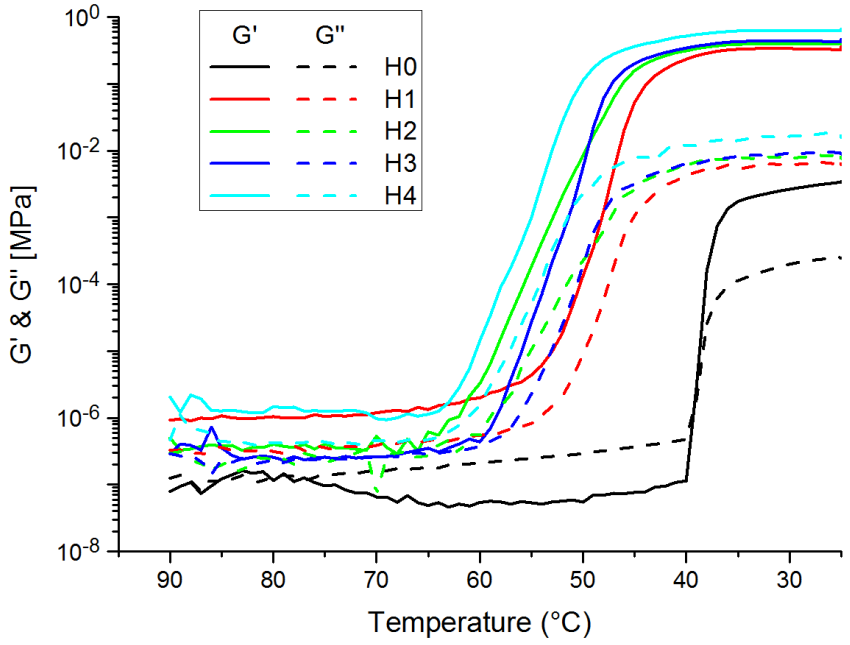


Figure 5.17: Temperature sweep of GG hydrogels with different amounts of BAG measured on a rheometer.

Once the hydrogel solution exits the nozzle, it has to solidify as fast as possible. Pure GG hydrogel (sample H0) fully gels with $2-3$ $°C$ temperature drop (Figure 5.17), whereas the composite samples need around 10 $°C$ temperature drop or even more. Therefore, it

would help to have an estimation on how fast a hydrogel solution cools down once it exits the nozzle. This could not be measured since we could not measure the temperature of the hydrogel along its length after it exits the nozzle. However, with a few simplifications we can derive an equation for the temperature drop along the length of the extruded hydrogel.

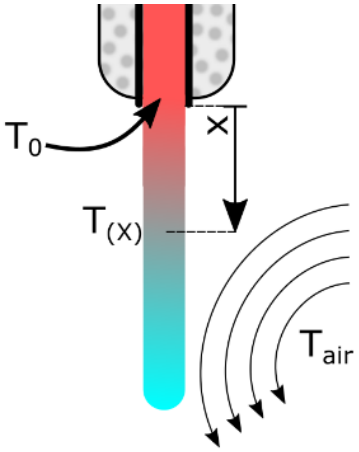


Figure 5.18: Sketch of hydrogel solution cooling down upon exiting the nozzle.

When the hydrogel solution exits the nozzle with a temperature of the syringe (T_0), it is cooled mainly by the surrounding air (Figure 5.18), which has a lower temperature (T_{air}). When the material touches the printing surface, it cools down even faster, but to simplify the system we will observe the worst-case scenario and see if the cooling of the material by air is sufficient by itself. This can be described by a one-dimensional heat transfer equation:

$$\frac{d}{dx}(kA\frac{dT}{dx}) + AQ_g + hP(T_{air} - T) = 0 \tag{5.5}$$

Where k is thermal conductivity of the hydrogel solution, which is assumed to be similar to a water's ($k = 0.591\ \frac{W}{m \cdot K}$). A is the cross-section surface of the solution that is extruded, which can be simplified to a cross-section of the nozzle opening. The temperature of the hydrogel solution is T, the temperature of the air T_{air} h is the convective heat transfer coefficient. This coefficient is very hard to determine since it depends on many factors (type of fluid, humidity of air, relative speed between the fluid and air, etc.), but we have used the smallest value found in the literature ($h = 10 \cdots 1000\ \frac{W}{m^2 \cdot K}$), and simulated the worst case scenario. Cooling of the surrounding air also depends on the surface area (P) between the hydrogel solution and air. Q_g is used to describe the generation of heat in the material, i.e. hydrogel solution. This part of the equation is neglected. Assuming also that thermal conductivity of the hydrogel solution does not change along the length in direction x, we can write the following equation:

$$\frac{kA}{hP}\frac{d^2T_{(x)}}{dx^2} + T_{air} - T_{(x)} = 0 \tag{5.6}$$

This is a second order differential equation that can be solved by assuming an exponential decrease of temperature $T_{(x)}$:

$$T_{(x)} - T_{air} = a \cdot \exp^{-b \cdot x} \tag{5.7}$$

$$\frac{dT}{dx} = -ab \cdot \exp^{-b \cdot x} \tag{5.8}$$

$$\frac{d^2T_{(x)}}{dx^2} = ab^2 \cdot \exp^{-b \cdot x} \tag{5.9}$$

To solve Equation 5.6, using Equations 5.7 and 5.9, we need to set $T_{(x=0)} = T_0$, which is the temperature of the hydrogel solution in the syringe.

$$T_{(x)} = T_{air} + (T_0 - T_{air}) \exp^{-\sqrt{\frac{hP}{kA}} \cdot x} \tag{5.10}$$

Assuming the extruded hydrogel solution has a cylindrical shape with a radius r, we can simplify the last term:

$$T_{(x)} = T_{air} + (T_0 - T_{air}) \exp^{-\sqrt{\frac{2h}{rk}} \cdot x} \tag{5.11}$$

Expressing the x from Equation 5.11, we can calculate at which distance from the nozzle, the hydrogel solution cools down to a certain temperature $T_{(x)}$:

$$x = \sqrt{\frac{rk}{2h}} \ln\left(1 - \frac{T_{(x)} - T_{air}}{T_0 - T_{air}}\right) \tag{5.12}$$

For example, we can now calculate the worst case scenario and print H1 hydrogel solution. Lets assume the room temperature is $T_{air} = 22\ °C$, and we want to know how far from the nozzle ($r = 0.25\ mm$) the printing solution cools down from $T_0 = 55\ °C$ to $T_{(x)} = 45\ °C$, at which point the solution should solidify. Solving Equation 5.12, we get a result of $x = 0.72\ mm$. This means that even in the worst scenario, cooling of the hydrogel solution that exits the nozzle is very fast. Cooling is so fast especially due to a small diameter of the nozzle.

5.3.1 Printing hydrogels

From the results of 3D printing (Chapter 4.3.3.) we can see that printing of GG hydrogels is possible. We were able to make simple cylindrical shapes (Figure 4.32) and square tower (Figure 4.30) to almost 10 mm of height. However, there are limitations that would need to be addressed to further improve printing of GG hydrogels.

As we saw in Figure 4.30 and 4.31, there are issues with the amount of hydrogel extruded on sharp turns. This is not an issue for models below 5 mm in height, but becomes an issue with higher models. Consequently, on the straight lines the nozzle is too far away from the printed model and on the edges it is touching the model. If the nozzle starts touching the model, it can break parts of the printed model and these parts can also attach on the nozzle, disturbing the the flow of hydrogel solution afterwards. On the other hand, where the nozzle is too far away from the model, the syringe might stop laying down the material. This appears to be an issue of such materials and might not be possible to avoid it. Because the hydrogel solution, right after it exits the nozzle, has low viscosity (comparable to water's viscosity), even lower elasticity (Figure 5.17) and high surface tension, it will tend to form droplets instead of a filament (like thermoplastic polymers do when used in FFF printing). Therefore, it only lays repeatable layers of hydrogel if the surface below is close enough. In other word, the surface below the nozzle defines how the hydrogel will form another layer. This is also a reason why we were not able to print bridges or severe overhangs with hydrogels. We could only build higher, in places where there was support of the previous layer.

But, where is the reason for the printed straight lines being lower than edges? There are three reasons that are important to my knowledge: Viscoelasticity of the printed solution, surface tension of the printed solution and the flexing of the extruder head. I will try to give the explanation behind each of the reasons.

The solution of GG is viscoelastic, which was determined by rheological measurements. When the hydrogel solution is extruded in a straight line, the nozzle is travelling at a constant speed, therefore also the extrusion rate of the hydrogel solution is constant. In this case, the necessary extrusion rate can simply be calculated based on the speed of the nozzle, size of the nozzle, layer width and height. However, when the nozzle approaches a sharp corner, it slows down, changes direction and accelerates to the set nozzle rate. This is necessary to reduce vibrations of the printer during extrusion, which is also connected with the flexing of the extruder head. During this deceleration and acceleration of the nozzle, the slicer also adjusts the extrusion rate to be proportional with the speed of the nozzle. This direct correlation between the nozzle speed and the extrusion rate would be completely valid for a pure viscous fluid. However, when the extruded fluid, as in our case, is viscoelastic, there is relaxation of the extruded fluid during the change of the extrusion rate. Specifically, when the extrusion rate is decreasing, the shear stresses on the hydrogel solution lower and the polymer molecules start to relax. This relaxation is instantaneous in purely viscous fluids, whereas polymer solution needs time to relax, which means that even after the compression of the syringe slows down, the rate of the hydrogel solution extrusion slows down with a delay. This could be avoided if the rate of extrusion would decelerate before the nozzle speed does, however determining the precise delay could be very difficult. It should be done based on relaxation properties of the extruded hydrogels solution, however it would most likely be easier by trial and error.

The second possible reason for the variation of the volume of extruded material, could be surface tension of the hydrogel solution. As we mentioned before, surface tension is high enough, compared to the viscosity of the hydrogel solution that it can form droplets if extruded in the air. This means that when the nozzle goes around a sharp corner, the material will soften around the edge, making a curve. This could be avoided if the material would solidify the moment it is extruded from the nozzle, however heat transfer requires time in which the forces of surface tension pull the material closer, softening the corners and locally increasing the height of the layer. This would be hard to correct by modifying the slicer parameters. The most direct way to solve this problem would be to adjust material properties by increasing the viscosity of the hydrogel solution as well as to lower the surface tension.

The last reason is possible flexing of the extruder head. Every body with a certain speed has a linear momentum that needs to change when changing the direction of movement. If the changes of the movement are abrupt (in case of sharp corners), the forces on the moving body can be significant. One way is to make less abrupt changes of direction (making edges curved) or to reduce the speed before the change of the direction. The latter solution is always used in FFF printers. By limiting maximum accelerations of the extruder head (in x and y axis direction), we can reduce the consequences of abrupt edges. This in terms reduces forces on the extruder head when changing direction, and consequently reducing vibrations. These vibrations can cause deformation of the extruder head. If the extruder head was very rigid, it would not be a problem, however, due to simplicity, our extruder head is partially made of more flexible ABS plastic, as it was 3D printed. This could mean that during nozzle passing corners, the extruder head could deform and additionally compress the syringe. This potential problem was avoided as much as possible with reducing the maximum acceleration of the extruder head in x and y axis direction by a factor of 10 according to the default settings.

After examining all three possible issues that could cause the variation of the volume of extruded material, we can make some conclusions. The last issue with flexing of the extruder head was easily solved by reducing the maximum acceleration of the extruder head. This consequently increased the effect of the first issue, by increasing the time of deceleration and acceleration of the nozzle when going around sharp corners. However, since the speed of deceleration and acceleration of the nozzle has also decreased, relaxation of the material should have a less prominent effect. Which leaves us with a surface tension of the hydrogel solution. This seems to be the main issue. As mentioned before, this can-not be easily solved by changing the printing parameters, instead we should put more effort in tailoring the rheological properties of the hydrogel solution as well as reducing its surface tension. On the other hand, this is only an issue with printing sharper corners as seen on the square model (Figure 4.30), whereas the cylindrical model did not show these issues (Figure 4.32) since it does not have any sharp edges. This means that in practice, printing scaffolds with soft edges would not be a problem.

Chapter 6

Conclusions

In this work, **viscoelastic properties of gellan gum** (GG) hydrogel composites for tissue engineering applications were studied in depth. Hydrogel samples were prepared with a 2 $wt.\%$ of GG and with different amounts of bioactive glass (BAG) particles or $CaCl_2$ for reinforcement. Five commonly used techniques for the characterization of mechanical properties were studied: uniaxial compression, rheometry, dynamical mechanical analysis (DMA), indentation and ultrasonic wave propagation. Afterwards, DMA was chosen as the most suitable technique for studying degradation of composite hydrogels. On the other hand, rheometry provided crucial information to the possibility of using GG hydrogels for 3D printing.

Viscoelastic properties of hydrogel-based scaffolds for tissue engineering are of crucial importance, especially in load bearing applications. Techniques like uniaxial compression and indentation are primarily intended for characterization of elastic materials. Standard **indenter** (CSM Nano Hardness Tester®) turned out to produce too high stresses and had insufficient resolution to measure any of the hydrogel composite samples. However, dedicated indenters for soft materials can be found which are able to measure hydrogel composites, but are much less common. **Uniaxial compression** on the other hand was capable of measuring the elastic modulus of hydrogel composites and could identify viscoelasticity. However, uniaxial compression, despite its simplicity, provides a harsh 'step-up' excitation followed by a constant strain rate deformation. This does not result in a steady-state deformation, making it impossible to describe the relaxation of the material during a single measurement. Despite this, results of elastic moduli from uniaxial compression were comparable to the results of rheometry and DMA.

Rheometry and DMA, on the other hand, are techniques intended for the characterization of viscoelastic materials. The main measuring procedure called 'frequency sweep' oscillates the sample, at different frequencies, in linear region and in 'steady state', providing more information on the material. Both techniques provide the elastic and dissipative response of the material at different frequencies (from approx. 0.1 to 100 Hz). Whereas DMA is more useful for premade samples and measures in compression, rheometry measures in shear and requires the sample to be made in the rheometer.

Ultrasonic wave propagation technique did not show any correlation with the results of other techniques. Calculated values of elastic moduli from the speed of ultrasonic wave propagation, were more than two orders of magnitude higher than moduli obtained from other techniques. However, the results obtained appear to give information on hydrogel's glassy modulus. This does not give practical information on how the material behaves under mechanical loading at ambient conditions, but it does correlate to the molecular structure and the amount of BAG it contains.

Long-term submersion of GG samples in simulated bodily fluid (SBF) did

not show significant degradation of the samples, but it showed formation of hydroxyapatite (HA). The goal was to show how viscoelastic properties change in 28 days during submersion of the samples in SBF. We expected degradation of the samples in this time, due to the hydrolysis of GG in SBF, however it turned out that the samples were crosslinked too much to allow hydrolysis to happen in the first place. After one week of submersion, the sample's viscoelastic properties started to increase. This implies that either the samples started to crosslink further, or the formation of HA acted as a reinforcing phase. The formation of HA was faster on samples with BAG.

Rheometry lead to an understanding of the crucial properties needed for **3D printing of GG hydrogels**. Since GG hydrogel solidifies upon cooling, we could use this property to lay down layers of liquid hydrogel solution using an FFF type 3D printer, which would solidify once it exits the printing nozzle. A conventional 3D printer was modified to hold a heated syringe with a hydrogel solution and used for printing hydrogels that gel upon cooling.

This work has summed up the characterization techniques for the determination of viscoelastic properties of hydrogels for tissue engineering applications. The obtained results provide information that allows for a comparison of results of different techniques. It was observed that the GG hydrogel composites, which are crosslinked with Ca^{2+} ions, do not degrade in SBF, but they do promote, formation of HA. In order to fully verify if the GG composites are still appropriate as a biodegradable scaffold material, we would need to perform long-term tests in the presence of enzymes in SBF, which could lead to a degradation of samples.

References

[1] H. T. Nia, I. S. Bozchalooi, Y. Li, L. Han, H.-H. Hung, E. Frank, K. Youcef-Toumi, C. Ortiz, and A. Grodzinsky, "High-bandwidth AFM-based rheology reveals that cartilage is most sensitive to high loading rates at early stages of impairment.," *Biophysical journal*, vol. 104, no. 7, pp. 1529–37, Apr. 2013. DOI: 10.1016/j.bpj.2013.02.048. [Online]. Available: http://www.ncbi.nlm.nih.gov/pubmed/23561529.

[2] Q. Chen, F. Baino, S. Spriano, N. M. Pugno, and C. Vitale-Brovarone, "Modelling of the strength–porosity relationship in glass-ceramic foam scaffolds for bone repair," *Journal of the European Ceramic Society*, Jan. 2014. DOI: 10.1016/j.jeurceramsoc.2013.11.041. [Online]. Available: http://linkinghub.elsevier.com/retrieve/pii/S0955221913005608.

[3] I. Johnson and H. Liu, "A study on factors affecting the degradation of Magnesium and a Magnesium-Yttrium alloy for biomedical applications," *PloS one*, vol. 8, no. 6, e65603, Jan. 2013, ISSN: 1932-6203. DOI: 10.1371/journal.pone.0065603. [Online]. Available: http://www.pubmedcentral.nih.gov/articlerender.fcgi?artid=3683025%7B%5C&%7Dtool=pmcentrez%7B%5C&%7Drendertype=abstract.

[4] N. Drnovšek, S. Novak, U. Dragin, M. Čeh, M. Gorenšek, and M. Gradišar, "Bioactive glass enhances bone ingrowth into the porous titanium coating on orthopaedic implants.," *International orthopaedics*, vol. 36, no. 8, pp. 1739–45, Aug. 2012, ISSN: 1432-5195. DOI: 10.1007/s00264-012-1520-y. [Online]. Available: http://www.pubmedcentral.nih.gov/articlerender.fcgi?artid=3535029%7B%5C&%7Dtool=pmcentrez%7B%5C&%7Drendertype=abstract.

[5] A. Dejaco, V. S. Komlev, J. Jaroszewicz, W. Swieszkowski, and C. Hellmich, "Micro CT-based multiscale elasticity of double-porous (pre-cracked) hydroxyapatite granules for regenerative medicine.," *Journal of biomechanics*, vol. 45, no. 6, pp. 1068–75, Apr. 2012, ISSN: 1873-2380. DOI: 10.1016/j.jbiomech.2011.12.026. [Online]. Available: http://www.ncbi.nlm.nih.gov/pubmed/22296936.

[6] J. A. Kluge, N. C. Rosiello, G. G. Leisk, D. L. Kaplan, and A. L. Dorfmann, "The Consolidation Behavior of Silk Hydrogels," *Journal of the Mechanical Behavior of Biomedical Materials*, vol. 3, no. 3, pp. 278–289, 2011. DOI: 10.1016/j.jmbbm.2009.12.001.The.

[7] S. Rammensee, D. Huemmerich, K. Hermanson, T. Scheibel, and a.R. Bausch, "Rheological characterization of hydrogels formed by recombinantly produced spider silk," *Applied Physics A*, vol. 82, no. 2, pp. 261–264, Nov. 2005. DOI: 10.1007/s00339-005-3431-x. [Online]. Available: http://link.springer.com/10.1007/s00339-005-3431-x.

[8] Y. Ohyabu, T. Adegawa, T. Yoshioka, T. Ikoma, T. Uemura, and J. Tanaka, "Cartilage regeneration using a porous scaffold, a collagen sponge incorporating a hydroxyapatite/chondroitinsulfate composite," *Materials Science and Engineering: B*, vol. 173, no. 1-3, pp. 204–207, Oct. 2010, ISSN: 09215107. DOI: 10.1016/j.mseb.2009.12.008. [Online]. Available: http://linkinghub.elsevier.com/retrieve/pii/S0921510709005339.

[9] S. V. Vlierberghe, V. Cnudde, P. Dubruel, B. Masschaele, A. Cosijns, I. D. Paepe, P. J. S. Jacobs, L. V. Hoorebeke, J. P. Remon, and E. Schacht, "Porous gelatin hydrogels: 1. Cryogenic formation and structure analysis.," *Biomacromolecules*, vol. 8, no. 2, pp. 331–7, Feb. 2007. DOI: 10.1021/bm060684o. [Online]. Available: http://www.ncbi.nlm.nih.gov/pubmed/17291055.

[10] D. F. Coutinho, S. V. Sant, H. Shin, J. T. Oliveira, M. E. Gomes, N. M. Neves, A. Khademhosseini, and R. L. Reis, "Modified Gellan Gum hydrogels with tunable physical and mechanical properties.," *Biomaterials*, vol. 31, no. 29, pp. 7494–502, Oct. 2010, ISSN: 1878-5905. DOI: 10.1016/j.biomaterials.2010.06.035. [Online]. Available: http://www.pubmedcentral.nih.gov/articlerender.fcgi?artid=2933815%7B%5C&%7Dtool=pmcentrez%7B%5C&%7Drendertype=abstract.

[11] A. Gantar, L. P. da Silva, J. M. Oliveira, A. P. Marques, V. M. Correlo, S. Novak, and R. L. Reis, "Nanoparticulate bioactive-glass-reinforced gellan-gum hydrogels for bone-tissue engineering.," *Materials science & engineering. C, Materials for biological applications*, vol. 43, pp. 27–36, Oct. 2014, ISSN: 1873-0191. DOI: 10.1016/j.msec.2014.06.045. [Online]. Available: http://www.sciencedirect.com/science/article/pii/S0928493114004159.

[12] D. Puppi, F. Chiellini, a.M. Piras, and E. Chiellini, "Polymeric materials for bone and cartilage repair," *Progress in Polymer Science*, vol. 35, no. 4, pp. 403–440, Apr. 2010, ISSN: 00796700. DOI: 10.1016/j.progpolymsci.2010.01.006. [Online]. Available: http://linkinghub.elsevier.com/retrieve/pii/S0079670010000134.

[13] G. Chen, T. Ushida, and T. Tateishi, "Scaffold Design for Tissue Engineering," *Macromolecular Bioscience*, vol. 2, no. 2, pp. 67–77, Feb. 2002. DOI: 10.1002/1616-5195(20020201)2:2<67::AID-MABI67>3.0.CO;2-F. [Online]. Available: http://doi.wiley.com/10.1002/1616-5195(20020201)2:2%7B%3C%7D67::AID-MABI67%7B%3E%7D3.0.CO;2-F.

[14] X. Luo, L. Zhang, Y. Morsi, Q. Zou, Y. Wang, S. Gao, and Y. Li, "Hydroxyapatite/polyamide66 porous scaffold with an ethylene vinyl acetate surface layer used for simultaneous substitute and repair of articular cartilage and underlying bone," *Applied Surface Science*, vol. 257, no. 23, pp. 9888–9894, Sep. 2011, ISSN: 01694332. DOI: 10.1016/j.apsusc.2011.06.096. [Online]. Available: http://linkinghub.elsevier.com/retrieve/pii/S016943321100972X.

[15] J. R. Tse and A. J. Engler, "Preparation of hydrogel substrates with tunable mechanical properties.," *Current protocols in cell biology / editorial board, Juan S. Bonifacino ... [et al.]*, vol. Chapter 10, no. June, Unit 10.16, Jun. 2010. DOI: 10.1002/0471143030.cb1016s47. [Online]. Available: http://www.ncbi.nlm.nih.gov/pubmed/20521229.

[16] E. R. Morris, K. Nishinari, and M. Rinaudo, "Gelation of gellan - A review," *Food Hydrocolloids*, vol. 28, no. 2, pp. 373–411, 2012. DOI: 10.1016/j.foodhyd.2012.01.004. [Online]. Available: http://dx.doi.org/10.1016/j.foodhyd.2012.01.004.

[17] N. Bureau, P. Gels, P. Science, T. I. Workshop, and R. Polysaccharides, "Gellan gum - introduction for a conference," 1996.

[18] E. Miyoshi, T. Takaya, and K. Nishinari, "Rheological and thermal studies of gel-sol transition in gellan gum aqueous solutions," *Carbohydrate Polymers*, vol. 30, no. 2-3, pp. 109–119, Jul. 1996, ISSN: 01448617. DOI: 10.1016/S0144-8617(96)00093-8. [Online]. Available: http://linkinghub.elsevier.com/retrieve/pii/S0144861796000938.

[19] T. Osmalek, A. Froelich, and S. Tasarek, "Application of gellan gum in pharmacy and medicine," *International Journal of Pharmaceutics*, vol. 466, no. 1-2, pp. 328–340, 2014. DOI: 10.1016/j.ijpharm.2014.03.038.

[20] C. J. Ferris, K. J. Gilmore, G. G. Wallace, and M. i. H. Panhuis, "Modified gellan gum hydrogels for tissue engineering applications," *Soft Matter*, vol. 9, no. 14, p. 3705, 2013, ISSN: 1744-683X. DOI: 10.1039/c3sm27389j. [Online]. Available: http://xlink.rsc.org/?DOI=c3sm27389j.

[21] L. L. Hench, R. J. Splinter, W. C. Allen, and T. K. Greenlee, "Bonding mechanisms at the interface of ceramic prosthetic materials," *Journal of Biomedical Materials Research*, vol. 5, no. 6, pp. 117–141, Nov. 1971, ISSN: 0021-9304. DOI: 10.1002/jbm.820050611. [Online]. Available: http://doi.wiley.com/10.1002/jbm.820050611.

[22] M. N. Rahaman, D. E. Day, B. S. Bal, Q. Fu, S. B. Jung, L. F. Bonewald, and A. P. Tomsia, "Bioactive glass in tissue engineering," *Acta Biomaterialia*, vol. 7, no. 6, pp. 2355–2373, 2011, ISSN: 1742-7061. DOI: 10.1016/j.actbio.2011.03.016. [Online]. Available: http://dx.doi.org/10.1016/j.actbio.2011.03.016.

[23] N. Drnovšek, "Development of Coatings on Ti6Al4V Alloy for New Generation Implants Bone with Improved Osseointegration," PhD thesis, 2012, p. 132.

[24] G. Roudaut, D. Simatos, D. Champion, E. Contreras-Lopez, and M. Le Meste, "Molecular mobility around the glass transition temperature: a mini review," *Innovative Food Science & Emerging Technologies*, vol. 5, no. 2, pp. 127–134, 2004, ISSN: 14668564. DOI: 10.1016/j.ifset.2003.12.003.

[25] K. Ninomiya and J. D. Ferry, "Some approximate equations useful in the phenomenological treatment of linear viscoelastic data," *Journal of Colloid Science*, vol. 14, no. 1, pp. 36–48, 1959, ISSN: 0095-8522. DOI: http://dx.doi.org/10.1016/0095-8522(59)90067-4. [Online]. Available: http://www.sciencedirect.com/science/article/pii/0095852259900674.

[26] F. Schwarzl and L. Struik, "Analysis of relaxation measurements," *Advances in Molecular Relaxation Processes*, vol. 1, no. 3, pp. 201–255, 1968, ISSN: 0001-8716. DOI: http://dx.doi.org/10.1016/0001-8716(68)80001-X. [Online]. Available: http://www.sciencedirect.com/science/article/pii/000187166880001X.

[27] (2014). Polymer master curve, [Online]. Available: http://polymerinnovationblog.com/thermoset-characterization-part-16-applications-dynamic-mechanical-analysis-dma/ (visited on 08/07/2017).

[28] P. I. Lee, "Effect of non-uniform initial drug concentration distribution on the kinetics of drug release from glassy hydrogel matrices," *Polymer*, vol. 25, no. 7, pp. 973–978, 1984. DOI: 10.1016/0032-3861(84)90082-X.

[29] S. C. Cowin, Ed., *Bone Mechanics Handbook*, Second Edi. 2001, p. 981, ISBN: 0849391172. DOI: 10.1016/S0021-9290(01)00251-2.

[30] G. W. Greene, B. Zappone, B. Zhao, O. Söderman, D. Topgaard, G. Rata, and J. N. Israelachvili, "Changes in pore morphology and fluid transport in compressed articular cartilage and the implications for joint lubrication.," *Biomaterials*, vol. 29, no. 33, pp. 4455–62, Nov. 2008. DOI: 10.1016/j.biomaterials.2008.07.046. [Online]. Available: http://www.ncbi.nlm.nih.gov/pubmed/18755507.

[31] W. C. Oliver and G. M. Pharr, "Measurement of hardness and elastic modulus by instrumented indentation : Advances in understanding and refinements to methodology," *Journal of Materials Research*, vol. 19, no. 1, pp. 3–20, 2004.

[32] (2015). Properties of waves, [Online]. Available: http://lightcoalition.org/properties-waves-wave-cycles-scalar-transverse-energy/ (visited on 08/07/2017).

[33] P. Karte, "Experimental Determination of the Stiffness Evolution of Young Cement Pastes with and without Fly-Ash as Cement Replacement Material," PhD thesis, 2014, p. 68.

[34] F. J. O'Brien, "Biomaterials & scaffolds for tissue engineering," *Materials Today*, vol. 14, no. 3, pp. 88–95, Mar. 2011, ISSN: 13697021. DOI: 10.1016/S1369-7021(11)70058-X. [Online]. Available: http://linkinghub.elsevier.com/retrieve/pii/S136970211170058X.

[35] C. M. Murphy, M. G. Haugh, and F. J. O'Brien, "The effect of mean pore size on cell attachment, proliferation and migration in collagen–glycosaminoglycan scaffolds for bone tissue engineering," *Biomaterials*, vol. 31, no. 3, pp. 461–466, Jan. 2010, ISSN: 01429612. DOI: 10.1016/j.biomaterials.2009.09.063. [Online]. Available: http://linkinghub.elsevier.com/retrieve/pii/S0142961209009958.

[36] R. Singh, P. D. Lee, T. C. Lindley, C. Kohlhauser, C. Hellmich, M. Bram, T. Imwinkelried, and R. J. Dashwood, "Characterization of the deformation behavior of intermediate porosity interconnected Ti foams using micro-computed tomography and direct finite element modeling.," *Acta biomaterialia*, vol. 6, no. 6, pp. 2342–51, Jun. 2010, ISSN: 1878-7568. DOI: 10.1016/j.actbio.2009.11.032. [Online]. Available: http://www.ncbi.nlm.nih.gov/pubmed/19961958.

[37] V. Karageorgiou and D. L. Kaplan, "Porosity of 3D biomaterial scaffolds and osteogenesis.," *Biomaterials*, vol. 26, no. 27, pp. 5474–91, Sep. 2005, ISSN: 0142-9612. DOI: 10.1016/j.biomaterials.2005.02.002. [Online]. Available: http://www.ncbi.nlm.nih.gov/pubmed/15860204.

[38] (2017). Freeze drying, [Online]. Available: http://www.khoshkmana.ir/Page1.html (visited on 08/07/2017).

[39] S. V. Murphy and A. Atala, "3D bioprinting of tissues and organs," *Nature Biotechnology*, vol. 32, no. 8, pp. 773–785, 2014. DOI: 10.1038/nbt.2958. [Online]. Available: http://www.nature.com/doifinder/10.1038/nbt.2958.

[40] I. Grabec, *Tridimenzionalni rekoder*, 1969.

[41] (2016). Pri zasnovi izdelkov nas bo omejevala samo še domišljija - delo, [Online]. Available: http://www.delo.si/sobotna/pri-zasnovi-izdelkov-nas-bo-omejevala-samo-se-domisljija.html (visited on 02/20/2016).

[42] (2016). Interview with dr. grabec, [Online]. Available: http://radioprvi.rtvslo.si/2016/03/prof-dr-igor-grabec/ (visited on 08/07/2017).

[43] AMazing®. (2017). Additive manufacturing techniques, [Online]. Available: http://additive%20manufacturing.com/basics/ (visited on 08/07/2017).

[44] A. Gantar, "Bioactive glass-based composite scaffolds for tissue engineering applications," PhD thesis, 2016, p. 86.

[45] T. Kokubo and H. Takadama, "How useful is SBF in predicting in vivo bone bioactivity?" *Biomaterials*, vol. 27, no. 15, pp. 2907–15, May 2006. DOI: 10.1016/j.biomaterials.2006.01.017. [Online]. Available: http://www.ncbi.nlm.nih.gov/pubmed/16448693.

[46] T. Brynk, C. Hellmich, A. Fritsch, P. Zysset, and J. Eberhardsteiner, "Experimental poromechanics of trabecular bone strength: role of Terzaghi's effective stress and of tissue level stress fluctuations.," *Journal of biomechanics*, vol. 44, no. 3, pp. 501–508, Feb. 2011, ISSN: 1873-2380. DOI: 10.1016/j.jbiomech.2010.09.016. [Online]. Available: http://www.ncbi.nlm.nih.gov/pubmed/20883995.

[47] J. M. Zuidema, C. J. Rivet, R. J. Gilbert, and F. A. Morrison, "A protocol for rheological characterization of hydrogels for tissue engineering strategies.," *Journal of biomedical materials research. Part B, Applied biomaterials*, vol. 00B, no. 00, pp. 1–11, Dec. 2013. DOI: 10.1002/jbm.b.33088. [Online]. Available: http://www.ncbi.nlm.nih.gov/pubmed/24357498.

[48] C. Kohlhauser, C. Hellmich, C. Vitale-Brovarone, a. R. Boccaccini, a. Rota, and J. Eberhardsteiner, "Ultrasonic Characterisation of Porous Biomaterials Across Different Frequencies," *Strain*, vol. 45, no. 1, pp. 34–44, Feb. 2009. DOI: 10.1111/j.1475-1305.2008.00417.x. [Online]. Available: http://doi.wiley.com/10.1111/j.1475-1305.2008.00417.x.

[49] Y. Jin, B. Kundu, Y. Cai, S. C. Kundu, and J. Yao, "Bio-inspired mineralization of hydroxyapatite in 3D silk fibroin hydrogel for bone tissue engineering," *Colloids and Surfaces B: Biointerfaces*, vol. 134, pp. 339–345, 2015, ISSN: 09277765. DOI: 10.1016/j.colsurfb.2015.07.015. [Online]. Available: http://linkinghub.elsevier.com/retrieve/pii/S0927776515300461.

[50] A. Goel, S. Kapoor, R. R. Rajagopal, M. J. Pascual, H.-W. Kim, and J. M. Ferreira, "Alkali-free bioactive glasses for bone tissue engineering: A preliminary investigation," *Acta Biomaterialia*, vol. 8, no. 1, pp. 361–372, 2012, ISSN: 1742-7061. DOI: http://dx.doi.org/10.1016/j.actbio.2011.08.026. [Online]. Available: http://www.sciencedirect.com/science/article/pii/S1742706111003795.

[51] M. Mohamed, O. Hassane, C. H. Dobrez-Sridi Rachida, P.-M. Pascal, C.-L. Dominique, C. Hassane, and C. Guy, "Synthesis and in vitro characterization of melt derived 47S CaO-P_2O_5-SiO_2-Na_2O bioactive glass," *Ceramics-Silikáty*, vol. 52, no. 1.4, pp. 121–129, 2008.

[52] D. C. Clupper, J. J. Mecholsky, G. P. LaTorre, and D. C. Greenspan, "Bioactivity of tape cast and sintered bioactive glass-ceramic in simulated body fluid," *Biomaterials*, vol. 23, no. 12, pp. 2599–2606, 2002, ISSN: 0142-9612. DOI: http://dx.doi.org/10.1016/S0142-9612(01)00398-2. [Online]. Available: http://www.sciencedirect.com/science/article/pii/S0142961201003982.

[53] L. Li and M. Kazemi, "Fluid Pressurization in Cartilages and Menisci in the Normal and Repaired Human Knees," in *Modeling and Simulation in Engineering*, C. Alexandru, Ed. Boston, MA: InTech, 2012, pp. 277–298, ISBN: 978-953-51-0012-6. DOI: 10.5772/29727.

[54] J. E. Mark, Ed., *Physical Properties of Polymer Handbook*, Second Edi. Springer.

[55] M. Kutz, Ed., *Handbook of Materials Selection*. John Wiley & Sons, Inc., 2002.

[56] S. Eshraghi and S. Das, "Mechanical and microstructural properties of polycaprolactone scaffolds with one-dimensional, two-dimensional, and three-dimensional orthogonally oriented porous architectures produced by selective laser sintering," *Acta Biomater.*, vol. 6, pp. 2467–2476, 2010.

[57] J. M. Walker, A. M. Myers, M. D. Schluchter, V. M. Goldberg, A. I. Caplan, J. a. Berilla, J. M. Mansour, and J. F. Welter, "Nondestructive evaluation of hydrogel mechanical properties using ultrasound.," *Annals of biomedical engineering*, vol. 39, no. 10, pp. 2521–30, Oct. 2011. DOI: 10.1007/s10439-011-0351-0. [Online]. Available: http://www.pubmedcentral.nih.gov/articlerender.fcgi?artid=3418603%7B%5C&%7Dtool=pmcentrez%7B%5C&%7Drendertype=abstract.

[58] F. Lionetto, F. Montagna, and A. Maffezzoli, "Ultrasonic Dynamic Mechanical Analysis of Polymers Abstract :," vol. 15, no. 5, pp. 326–335, 2005. DOI: 10.3933/ApplRheol-15-326.

[59] J. M. Hugh, "Ultrasound Technique for the Dynamic Mechanical Analysis (DMA) of Polymers," PhD thesis, 2007. DOI: http://dx.doi.org/10.14279/depositonce-1706.

[60] J. D. Ferry, Ed., *Viscoelastic Properties of Polymers*, Third Edi. John Wiley & Sons, Inc., 1980.

[61] M. E. Shivokhin, D. J. Read, D. Kouloumasis, R. Kocen, F. Zhuge, C. Bailly, N. Hadjichristidis, and A. E. Likhtman, "Understanding effect of constraint release environment on end-to-end vector relaxation of linear polymer chains," *Macromolecules*, vol. 50, no. 11, pp. 4501–4523, 2017. DOI: 10.1021/acs.macromol.6b01947. [Online]. Available: http://dx.doi.org/10.1021/acs.macromol.6b01947.

[62] R. Kocen, M. Gasik, A. Gantar, and S. Novak, "Viscoelastic behaviour of hydrogel-based composites for tissue engineering under mechanical load," *Biomedical Materials*, vol. 12, no. 2, p. 025 004, 2017. DOI: 10.1088/1748-605X/aa5b00. [Online]. Available: https://doi.org/10.1088/1748-605X/aa5b00.

[63] N. Drnovsek, R. Kocen, A. Gantar, M. Drobnic-Kosorok, A. Leonardi, I. Krizaj, A. Rečnik, and S. Novak, "Size of silk fibroin β-sheet domains affected by Ca^{2+}," *J. Mater. Chem. B*, vol. 4, pp. 6597–6608, 40 2016. DOI: 10.1039/C6TB01101B. [Online]. Available: http://dx.doi.org/10.1039/C6TB01101B.

Bibliography

Scientific Articles

R. Kocen, M. Gasik, A. Gantar, and S. Novak, "Viscoelastic behaviour of hydrogel-based composites for tissue engineering under mechanical load," *Biomedical Materials*, vol. 12, no. 2, p. 025 004, 2017. DOI: 10.1088/1748-605X/aa5b00. [Online]. Available: https://doi.org/10.1088/1748-605X/aa5b00.

N. Drnovsek, R. Kocen, A. Gantar, M. Drobnic-Kosorok, A. Leonardi, I. Krizaj, A. Rečnik, and S. Novak, "Size of silk fibroin β-sheet domains affected by Ca^{2+}," *J. Mater. Chem. B*, vol. 4, pp. 6597–6608, 40 2016. DOI: 10.1039/C6TB01101B. [Online]. Available: http://dx.doi.org/10.1039/C6TB01101B.

Conference Papers

R. Kocen, A. Gantar, N. Drnovšek, and S. Novak, "Rheology as a tool for validation of silk fibroin blend for 3D bio-printing," in *European Chapter Meeting of the Tissue Engineering and Regenerative Medicine International Society 2017*, Davos, Switzerland: TERMIS =Tissue Engineering and Regenerative Medicine International Society, 2017, p. 42.

N. Drnovšek, R. Kocen, M. Voga, G. Murn, L. Girandon, A. Rečnik, G. Majdič, and S. Novak, "Bioactive glass/fibroin composite scaffolds for the treatment of osteochondral defects," in *European Chapter Meeting of the Tissue Engineering and Regenerative Medicine International Society 2017*, Davos, Switzerland: TERMIS =Tissue Engineering and Regenerative Medicine International Society, 2017, p. 59.

J. Zvicer, A. Gantar, R. Kocen, D. Veljnović, S. Novak, and B. Obradović, "Biomimetic bioreactor characterization of scaffolds based on gellan-gum hydrogels with nano-particulate bioactive-glass," in *European Chapter Meeting of the Tissue Engineering and Regenerative Medicine International Society 2017*, Davos, Switzerland: TERMIS =Tissue Engineering and Regenerative Medicine International Society, 2017, p. 54.

R. Kocen, A. Gantar, and S. Novak, "3D printing biomaterials for regenerative medicine," in *9. študentska konferenca Mednarodne podiplomske šole Jožefa Stefana in 11. dan mladih raziskovalcev (Konferenca KMBO) = 9th Jožef Stefan International Postgraduate School Students' Conference and 11th Young researchers' Day*, M. Pavlin, Ed., Ljubljana, Slovenija: Ljubljana: Mednarodna podiplomska šola Jožefa Stefana, 2017, p. 52.

R. Kocen, M. Gasik, and S. Novak, "Improvement and validation of viscoelastic properties of hydrogels by bioactive glass particles additions," in *EROS 2016, 24th Annual Meeting, European Orthopaedic Research Conference*, Rizzoli, Italy: 2016, p. 42.

R. Kocen and S. Novak, "Can ultrasonic wave propagation predict mechanical properties in polymers?" In *Program in knjiga povzetkov = Program and book of abstracts, 24. mednarodna konferenca o materialih in tehnologijah*, M. GODEC and et. al., Eds., Portorož, Slovenija: Ljubljana: Inštitut za kovinske materiale in tehnologije, 2017, p. 116.

R. Kocen, A. Gantar, M. Gasik, and S. Novak, "Complete mechanical characterization of poroviscoelastic loadbearing scaffolds," in *Programme Book ESB 2016, Conference of the European Society of Biomechanics*, Lyon, France: 2016, p. 35.

A. Gantar, N. Drnovšek, R. Kocen, S. Novak, and G. Majdič, "Gellan gum soft construct for possible applications in skin tissue engineering," in *WBC 2016, 10th World Biomaterials Congress*, Montréal, Canada: 2016.

N. Drnovšek, R. Kocen, A. Gantar, K. Križman, M. Drobnič-Košorok, A. Rečnik, and S. Novak, "The influence of bioactive glass and the released Ca^{2+} ions on fibroin scaffolds properties : Secondary structure, mechanical properties and degradation," in *WBC 2016, 10th World Biomaterials Congress*, Montréal, Canada: 2016.

R. Kocen, M. Gasik, H. Christian, and S. Novak, "Viscoelastic properties of gellan gum - bag composites for tissue-engineering scaffolds," in *10th Young researchers' day*, S. P. Mihevc, M. Prunk, and J. Pungerčar, Eds., Ljubljana, Slovenija: Ljubljana: Institut Jožef Stefan, 2016, p. 31.

R. Kocen, A. Gantar, C. Hellmich, M. Gasik, and S. Novak, "Measuring viscoelasticity of hydrogel-bag composites," in *Program and book of abstracts, 23rd International Conference on Materials and Technology*, M. Godec and et al., Eds., Ljubljana, Slovenia: Ljubljana: Inštitut za kovinske materiale in tehnologije, 2015, p. 133.

S. Novak, A. Gantar, N. Drnovšek, R. Kocen, L. Girandon, and G. Majdič, "Kompozitni nosilci z bioaktivnim steklom za celično terapijo," in *Zbornik referatov in povzetkov, Slovenski kemijski dnevi 2015*, V. Kaučič and et al., Eds., Ljubljana, Slovenia: Ljubljana: Slovensko kemijsko društvo, 2015.

R. Kocen, A. Gantar, S. Novak, C. Hellmich, and M. Gasik, "Viscoelastic properties of hydrogel - "ceramic"composites for tissue-engineering scaffolds," in *Scientific program and abstracts of the 5th Eurosummer School on Biorheology and Symposium on Micro and Nanomechanics and Mechanobiology of Cells Tissues and Systems*, N. Antonova, I. Velcheva, and E. Zvetkova, Eds., Varna, Bolgaria: Sofia: Avangard Prima, 2015, p. 50.

R. Kocen, A. Gantar, M.-I. Pastrama, C. Hellmich, M. Gasik, and S. Novak, "Characterization of mechanical properties of hydrogel-"ceramic"used for tissue engineering scallolds," in *Unified scientific approaches towards REgenerative ORthopaedic and DEntistry, International [COST action MP1005 NAMABIO] Conference REDEOR*, San Servolo Island, Venice, Italy: 2015, p. 58.

R. Kocen, A. Gantar, S. Novak, C. Hellmich, and M. Gasik, "Mechanical properties of hydrogel-"ceramic"composites," in *9th Young researchers' day, abstract book*, N. Kavčič and et al., Eds., Ljubljana, Slovenia: Ljubljana: Institut Jožef Stefan, 2015, p. 33.

R. Kocen, A. Gantar, and S. Novak, "Viscoelastic properties of gellan gum scaffolds with bioactive glass particles," in *Journal of tissue engineering and regenerative medicine, ISSN 1932-6254*, TERMIS EU 2014 Meeting, 2014, p. 354.

A. Gantar, R. Kocen, and S. Novak, "Highly reinforced bioactive glass - gellan gum composite hydrogels for biomedical applications," in *Final programme, 26th Annual Conference [of] European Society for Biomaterials*, Liverpool, United Kingdom: 2014, p. 371.

R. Kocen, A. Gantar, and S. Novak, "Viscoelastic properties of scaffolds for tissue engineering," in *Program and abstract book, 8th Young Researchers' Day*, V. Žunič and et al., Eds., Ljubljana, Slovenia: Ljubljana: Institut Jožef Stefan, 2014.

Final Research Reports

R. Kocen, "Report on the short term scientific mission (STSM) : Dinamical mechanical analysis of hydrogel composites for tissue engineering," in *IJS delovno poročilo*, Aalto University, Finland, 2015.

R. Kocen, "Mechanical properties of composites for tissue engineering scaffolds : Report on the short term scientific mission," in *IJS delovno poročilo*, University of Technology, Vienna, 2014.

Technical Improvement

N. Drnovšek, K. Križman, A. Gantar, R. Kocen, and S. Novak, "Postopek priprave medicinskih pripomočkov iz svilnega fibroina : Tehnična izboljšava," Ljubljana: Institute Jožef Stefan, Tech. Rep., 2017, p. 7. [Online]. Available: `https://plus.si.cobiss.net/opac7/bib/30207527`.

Other Publications

M. E. Shivokhin, D. J. Read, D. Kouloumasis, R. Kocen, F. Zhuge, C. Bailly, N. Hadjichristidis, and A. E. Likhtman, "Understanding effect of constraint release environment on end-to-end vector relaxation of linear polymer chains," *Macromolecules*, vol. 50, no. 11, pp. 4501–4523, 2017. DOI: `10.1021/acs.macromol.6b01947`. [Online]. Available: `http://dx.doi.org/10.1021/acs.macromol.6b01947`.

R. Kocen, C. Bailly, and M. Shivokhin, "Controlling constraint release in polydisperse melts of linear polymers," in *Program and book of abstracts, 21st International Conference on Materials and Technology*, M. Godec and et al., Eds., Portorož, Slovenia: Ljubljana: Inštitut za kovinske materiale in tehnologije, 2013, p. 99.

Interviews

R. Kocen, *Bum regenerativne medicine*, TV Slovenija 1, oddaja Ugriznimo znanost, 2016. [Online]. Available: `http://4d.rtvslo.si/arhiv/ugriznimo-znanost/174428648`.

R. Kocen, A. Gantar, and N. Drnovšek, *Tkivno inženirstvo v K7*, RTV Slovenija, 3. program Ars, 2016. [Online]. Available: `http://ars.rtvslo.si/2016/12/pogled-v-znanost-91/`.

R. Kocen, *Po inovativnosti Slovenija med sledilci, zakaj ne med voditelji?* TV Slovenija 3, oddaja Točka preloma, 2016. [Online]. Available: `http://4d.rtvslo.si/arhiv/tocka-preloma/174434021`.

Biography

The author of this thesis , Rok Kocen, was born on March 14, 1989 in Ljubljana, Slovenia. His parents are Andreja and Boris Kocen. He has a younger brother Matej.

After graduating from the Bežigrad Gymnasium, Ljubljana in 2008, he was admitted to the Faculty of Mechanical Engineering at the University of Ljubljana. During his studies he joined ISIT (Institute for Sustainable Innovative Technologies) lead by Prof. Dr. Igor Emri, where he worked on several projects in the field of polymer materials. These projects included experimental work on commercial polymers and development of measuring software. He obtained his Bachelor's degree in 'Mechanical Engineering: Research and Development Program' in 2011.

Afterwards he joined European Masters in Engineering Rheology (EURHEO) and received an Erasmus Mundus scholarship for the time of studies abroad. First year and a half of Master's studies took place at the University of Minho, Portugal. He then spend the last half of the year of the two year program at the Catholic University of Louvain, Belgium, where he did his Master's thesis. The work was titled: 'Using "probe rheology" for controlling constraint release in polydisperse melts of linear polymers' and was done under supervision of Prof. Dr. Christian Bailly and Dr. Maxim Shivokhin. Experimental and modelling results were published in Macromolecules [61].

After finishing the Master's studies in 2013 he joined Department for Nanostructured Materials at Jožef Stefan Institute and enrolled into a doctoral program for Nanosciences and Nanotechnologies at Jožef Stefan International Postgraduate School (IPS). He attended two one month Short-Term Scientific Missions, one at Vienna University of Technology, Vienna, Austria in 2014 and another at Aalto University Foundation, Espoo, Finland in 2015. Both visits were funded within the COST Action MP1005 'From nano to macro biomaterials (design, processing, characterisation, modelling) and applications to stem cell regenerative orthopaedic and dental medicine—NAMABIO'. In the frame of a bilateral collaboration with Serbia, he visited Faculty of Technology and Metallurgy, University of Belgrade, Serbia and the group of Prof. Dr. Bojana Obradović.

He presented the results of his research work in papers [62], [63] and at several national and international conferences and meetings. He obtained an 'Award for the Best Young Scientist's Work' at the '5th Euro Summer School on Biorheology and Symposium on Micro and Nano Mechanics and Mechanobiology of Cells, Tissues and Systems 2015' in Varna, Bulgaria. The same year he was awarded for the Best Oral Presentation at '23th International Conference on Materials and Technology' in Portorož, Slovenia. In the year 2016 he and co-workers Dr. Ana Gantar, Dr. Nataša Drnovšek, Prof. Dr. Saša Novak and Kaja Križman received two awards for the Best Business Idea at 9th International Technology Transfer Conference (Bled, Slovenia) and CREA Summer Academy (Ljubljana, Slovenia). At the 9th Jožef Stefan IPS Students' Conference and Young Researchers Day of Chemistry, Materials, Biochemistry and Environment (CMBE), Ljubljana, Slovenia in 2017 he received the main award for the Best Presentation, Best Poster selected by the audience and SATENA award for the Best Presentation selected by a committee of journalists.